Brunel University London

DOCTORAL THESIS

Measurement of Energy Loss by Muons in Lithium Hydride on MICE

A Thesis submitted to Brunel University
in accordance with the requirements
for award of the degree of Doctor of Philosophy

in

the department of Particle Physics
Centre for Sensors & Instrumentation

Rhys Gardener

April 19, 2018

Declaration of Authorship

I, Rhys Gardener, declare that the work in this dissertation was carried out in accordance with the requirements of the University's Regulations and Code of Practice for Research Degree Programmes and that it has not been submitted for any other academic award. Except where indicated by specific reference in the text, the work is the candidate's own work. Work done in collaboration with, or with the assistance of, others, is indicated as such. Any views expressed in the dissertation are those of the author.

SIGNED: ..... DATE: .....

(Signature of student)

Abstract

The Muon Ionisation Cooling Experiment (MICE) has been commissioned to provide the first demonstration of ionisation cooling. MICE will aim to demonstrate that ionisation cooling can be used to reduce of the emittance of a beam of muons to meet the requirements of future particle physics experiments such as the Neutrino Factory, or Muon Collider. As of October 2016, commissioning of Step IV of MICE has been completed which provides an opportune time to make material physics studies on the absorber material.

The cooling formula that MICE will use to measure the emittance reduction was reviewed. It is shown that the energy loss term is important when measuring cooling, and an accurate measurement of the energy loss will hence improve the accuracy of the cooling formula. The physics of ionisation cooling is also reviewed.

The primary absorber used in the early data taking of MICE Step IV will be a 65mm disk of Lithium Hydride. The energy loss of Lithium Hydride was estimated using the equations of energy loss developed by Bethe. Methods were developed in this thesis to make measurements of the energy loss using data from the MICE trackers, and the time-of-flight data through the cooling channel.

The energy loss of muons in monte-carlo simulations measured with the two alternative methods was found to be in agreement, with a measurement by the trackers of 9.02 $\pm$ 0.07, and from simulated time-of-flight of 9.32 $\pm$ 0.15. The first measurement of energy loss by 200 MeV/c muons was made using time-of-flight data using real muons in the MICE channel of ΔE = 9.23 $\pm$ 0.13 MeV, corresponding to a stopping power of Lithium Hydride of $\frac{dE}{dx}$ = 1.42 $\pm$ 0.02 MeV g^{-1} cm^2.

Acknowledgements

I would like to first and foremost thank my supervisor Dr. Paul Kyberd for his continued support, patience and encouragement throughout my time at Brunel. I would also like to thank my colleagues within the MICE collaboration, in particular Chris Rogers for his continued and useful inputs on my analysis. I've thoroughly enjoyed my time at Brunel, in no small part due to the fantastic people that make up the physics group at Brunel, and my fellow students.

Contents

1 Introduction **1**

2 Neutrino Physics **3**
2.1 History . . . 3
2.2 The Solar Neutrino Problem . . . 4
2.3 Neutrino Oscillation Formulation . . . 6
2.4 Neutrino Oscillation Experimental Results . . . 8
2.4.1 Mass Heirachy . . . 9
2.5 Double beta decay . . . 9
2.6 Neutrino Factory . . . 11

3 The Muon Ionisation Cooling Experiment **13**
3.1 Emittance . . . 13
3.2 Ionisation Cooling . . . 17
3.3 MICE Experimental Setup . . . 19
3.3.1 Step IV . . . 19
3.3.2 The Demonstration of Ionisation Cooling . . . 20
3.4 Muon Beamline . . . 21
3.4.1 MICE Target design . . . 25
3.5 Absorbers . . . 26
3.6 RF Cavities . . . 28
3.7 Detectors . . . 29
3.7.1 Luminosity Monitor . . . 29
3.7.2 Time of Flight Detector . . . 29
3.7.3 Cherenkov Detector . . . 30
3.7.4 Trackers . . . 32
3.7.5 KL . . . 33
3.7.6 Electron Muon Ranger . . . 34

4 Energy Loss - Physical Processes **37**
4.1 Ionisation . . . 37

4.2 Multiple Scattering . . . 38
4.3 The Bethe formula . . . 39
4.4 Energy loss dependence on Material . . . 40
4.5 Momentum Effect on Energy Loss . . . 41
4.6 Fluctuations in Energy Loss . . . 42
4.7 Energy Loss for 200MeV Muons in Lithium Hydride. . . . 44

5 Simulation of Energy Loss Measurement in Step IV 49
5.1 Step IV . . . 49
5.2 SSD Descope . . . 50
5.3 Simulation Details . . . 52
5.4 Calculating the Energy Loss . . . 52
5.5 Momentum Reconstruction in Trackers . . . 53
5.5.1 TOF1 to TOF2 time Discrepancy . . . 59
5.6 Energy Loss . . . 60
5.6.1 Uncertainties . . . 61
5.6.2 Systematics . . . 64
5.6.3 Empty Absorber Unit . . . 65
5.6.4 LiH Absorber . . . 66
5.6.5 Field-on Analysis Conclusions . . . 68
5.7 Tracker vs Time reconstruction . . . 69
5.7.1 LiH Simulation data . . . 72
5.8 Results . . . 74

6 Energy Loss using Time of Flight 76
6.1 Method Outline . . . 76
6.1.1 Rayner Reconstruction for Momentum at TOF1 . . . 77
6.1.2 Delta as a function of Energy Loss . . . 79
6.1.3 Velocity of Muon before absorber . . . 81
6.1.4 Velocity of Muon after Absorber . . . 83
6.1.5 Python Simulation . . . 84
6.2 Monte Carlo Studies . . . 85
6.2.1 Cuts on simulated data . . . 86
6.2.2 Uncertainties . . . 87
6.2.3 Systematics . . . 88
6.2.4 TOF time and momentum reconstruction . . . 88
6.2.5 TOF reconstruction effects on Energy Loss . . . 89
6.2.6 Reconstructed and Simulated Energy Distributions . . . 91
6.2.7 Simulated Energy Loss with no Absorber . . . 95

6.2.8 Simulated Energy Loss in LiH 99
6.2.9 Energy Loss as a function of Momentum 102
6.2.10 Conclusions on monte carlo study 102
6.3 Real Data 103
6.3.1 Momentum verification with SSU 103
6.3.2 Empty Absorber 103
6.3.3 LiH Data with 200 MeV/c beam 106
6.4 Results Summary 109
6.4.1 Energy Loss Measurement 109
6.4.2 Comparison of the Measurement to Simulation 110

7 Conclusion **111**

List of Figures

2.1 The neutrino mass hierarchy. Populations of each flavour in each mass eigenstate are indicated by colour: ν_e in red, $\nu_m u$ in green and ν_τ in blue. 9
2.2 Feynman diagrams showing $2\nu\beta\beta$ on the left, and $0\nu\beta\beta$ with the virtual neutrinos on the right [1]. 10
2.3 Comparison of the two main results from the Heidelberg-Moscow experiment, one showing no peak in the $0\nu\beta\beta$ region, and the 'controversial' result with the $0\nu\beta\beta$ peak on the right. 11
2.4 Schematic drawing of the proposed Neutrino Factory by the IDS-NF collaboration.[2] 12

3.1 Trace space plot of an elliptical beam taken at a single point in time in 2D. The area of the ellipse is defined as the emittance ε, whilst α,β and γ are the Twiss parameters.[3] 15
3.2 Graphical representation of emittance reduction. 17
3.3 The original MICE staged plan. 20
3.4 Schematic of the MICE Step IV cooling channel. 21
3.5 Some proposed descope options for the demonstration of ionisation cooling. 22
3.6 MICE uses a Titanium target in the ISIS syncrotron between stations S6 and S7 to produce pions. These are captured by quadropole magnets and transported to the MICE cooling channel. 24
3.7 Schematic of the MICE Muon Beamline, showing the location of the target on ISIS, and the arrangement of the Quadropole, dipole, and decay solenoid magnets used to transport as many pions as possible to the cooling channel. 24
3.8 ISIS signals showing the beam intensity, total beamloss and summed beamloss from sector 7 (directly after the target) for the period that the MICE target is dipped. In this instance the sector 7 beamloss is shown as a negative going signal [4]. 25
3.9 Schematic of the target. Actuation is achieved through the stator coils and magnets.[5] 26
3.10 AFC module with LH2 absorber. [6] 27

3.11 The Lithium Hydride disk absorber. Radius 225mm, thickness 65mm. [7] 27
3.12 Partial cross section of one of the MICE RF modules, showing the cavities, couplers and BE windows. [8] 28
3.13 Schematic of the Luminosity Monitor [9] 29
3.14 TOF detector design. 3D view on left and schematic structure of scintillator and PMT on right. TOF2 has the same number of slabs as TOF0 but with a greater effective area. [10] 30
3.15 Time of flight between TOF0 and TOF1 for an electron beam. The left peak indicates population of electrons, the center peak muons and the rightmost peak pions. [11] 31
3.16 Vertical trace space emittance measurements using TOF1. True values from MC data on left, reconstructed MC in the center, and reconstructed experiemtal data on right. Taken from [10] 31
3.17 Response of the two CKOV detectors to muons, pions and electrons at a range of momenta. 32
3.18 Photograph of the 5 tracker stations. The stations are held by a carbon fibre frame. 33
3.19 Arrangement of the 3 tracker planes inside a single tracker station. 34
3.20 Schematic of the KL detector, from the side and the rear. [12] 34
3.21 Schematic of the EMR Detector, orientated on it's side. [13] 36
3.22 Downstream momentum as a function of range (R) travelled in the EMR. One bin is one plane and it's error is representative of the RMS of the momentum distribution within the bin. [13] 36

4.1 An incident muon scattering off an electron. 39
4.2 Mean energy loss rate in various materials from ionisation. [14] 41
4.3 Minimum Energy loss as a function of Z. The straight line is plotted for points where Z ¿ 6. 42
4.4 Mean excitation energies taken from the ICRU 37 report [15], and reviewed in the PDG [14]. Values based on experiment have error flags. The open circles show more recent determinations by Bichsel, and the dotted curve indicates the association $I = 16Z^{0.9}eV$ 43
4.5 Stopping power (=$\langle -dE/dx \rangle$) for muons in copper as a function of momentum. [16] 44
4.6 45
4.7 Mean energy loss of muons in 65mm of Lithium Hydride calculated from the Bethe equation for a range of muon energies from 100 to 1000MeV. . 46

4.8 Mean energy loss of muons in 65mm of Lithium Hydride calculated from the Bethe equation for a range of muon energies seen within the MICE cooling channel. . . . 46
4.9 Most probable energy loss of muons in 65mm of Lithium Hydride calculated by equation 4.8. . . . 47
4.10 Most probable energy loss of muons in 65mm of Lithium Hydride calculated by equation 4.8 compared to the mean energy loss predicted by the Bethe equation. . . . 48

5.1 Labelled diagram of the MICE Step IV cooling channel. . . . 50
5.2 Map of the magnetic field strength through the cooling channel after the SSD descope. . . . 51
5.3 Map of the magnetic field strength through the cooling channel after the SSD descope. . . . 52
5.4 Momentum distribution at TOF1. . . . 55
5.5 Momentum distribution at TKU1. . . . 55
5.6 Momentum distribution from simulation data at TKU1. . . . 56
5.7 Comparison between reconstructed and simulated momentum at TKU plane 1. . . . 56
5.8 Difference between reconstructed and simulated momentum at TKU plane 1. . . . 57
5.9 Difference between reconstructed and simulated momentum at TKU plane 1 for simulated data with 4T in the solenoid magnets. . . . 57
5.10 P_x residual for reconstructed and MC truth muons. . . . 58
5.11 P_y residual for reconstructed and MC truth muons. . . . 59
5.12 P_z residual for reconstructed and MC truth muons. . . . 59
5.13 Momentum distribution at TKD. . . . 60
5.14 Momentum distribution from simulation data at TKD1. . . . 60
5.15 Comparison between reconstructed and simulated momentum at TKD plane 1. . . . 61
5.16 P_x residual for reconstructed and MC truth muons. . . . 61
5.17 P_y residual for reconstructed and MC truth muons. . . . 62
5.18 P_z residual for reconstructed and monte carlo truth muons. . . . 62
5.19 Difference between reconstructed and simulated momentum at TKD plane 1. . . . 63
5.20 Non-corrected difference between MC and reconstructed time of flight between TOF1 and TOF2 after correction. Note the 0.5ns offset of the distribution from zero. . . . 63

5.21 Residual difference between MC and reconstructed time of flight between TOF1 and TOF2 after correction. 64
5.22 Monte carlo Energy loss measured in the Empty Absorber unit. 65
5.23 Reconstructed Energy loss for Empty Absorber data. 66
5.24 Reconstructed energy loss in the empty absorber for simulated muons passing through the absorber unit with the Lithium Hydride cylinder installed. 66
5.25 Simulated energy loss for muons passing through the absorber unit with the Lithium Hydride cylinder installed. 67
5.26 Reconstructed energy loss in Lithium Hydride for simulated muons passing through the absorber unit with the Lithium Hydride cylinder installed 67
5.27 Simulated energy loss distribution compared to the reconstructed energy loss from tracker data. 68
5.28 Residual between the monte carlo truth energy, and the energy reconstructed from time-of-flight data of muons just upstream of the absorber. . 69
5.29 Residual between the monte carlo truth energy, and the energy reconstructed from time-of-flight data of muons just downstream of the absorber. 70
5.30 Difference between the reconstructed muon energy before absorber. . . . 70
5.31 Difference between the reconstructed muon energy after absorber. 71
5.32 Simulated energy loss for empty absorber data reconstructed from TOF data. 71
5.33 Simulated energy loss versus energy loss reconstructed from TOF data for empty absorber data. 72
5.34 Overlaid energy loss distributions for empty absorber data obtained from tracker reconstruction and TOF reconstruction overlaid. 72
5.35 Energy loss for Lithium Hydride absorber dataset reconstructed from TOF data. 73
5.36 Simulated energy loss versus energy loss reconstructed from TOF data for LiH absorber data. 73
5.37 Overlaid energy loss distributions from LiH absorber dataset obtained from tracker reconstruction and TOF reconstruction. 74

6.1 The axial quadrupole gradient in Q7, Q8 and Q9 between TOF0 and TOF1. The model used to parametrize the path length of the muon is also illustrated. The width of these top-hat models is equal the effective length of the quadrupoles.[17] 78
6.2 Comparison between measurements of x' in data and Step I simulation at TOF 1 79

6.3 Comparison between measurements of y' in data and Step I simulation at TOF 1 . . . 79
6.4 Comparison between measurements of z' in data and Step I simulation at TOF 1 . . . 80
6.5 Annotated Step IV with the position of the muon in relation to the defined variables used for calculating field-off energy loss. . . . 81
6.6 Model of overall Energy loss from the Tracker, based on MAUS simulation and data tables. . . . 82
6.7 Model of overall Energy loss from the TOF, based on MAUS simulation and data tables. . . . 82
6.8 Effect on converging on v_{ad} through iteration on the final energy loss measurement. This plot is produced without consideration of the effect of the TOF resolution on the measurement. . . . 84
6.9 Effect of TOF resolution on Energy Loss measurement. . . . 84
6.10 Difference between reconstructed and simulated time-of-flight between TOF1 and TOF2. . . . 86
6.11 Difference between reconstructed and simulated time-of-flight for a muon between the absorber and the downstream tracker. . . . 86
6.12 Difference between reconstructed and simulated velocity in terms of the relativistic unit beta between the absorber and the downstream tracker. . . . 87
6.13 Reconstructed time of flight for Muons between TOF0 and TOF1. . . . 88
6.14 Reconstructed time of flight for Muons between TOF1 and TOF2. . . . 89
6.15 Comparison between muon momentum at TOF1 vs reconstructed momentum before the absorber. . . . 90
6.16 Comparison between muon momentum at TOF1 vs reconstructed momentum before the absorber. . . . 90
6.17 Momentum distribution at TOF1. . . . 91
6.18 Residual between monte carlo and reconstructed momentum at TOF1. . . . 91
6.19 Reconstructed Energy distribution before the absorber. . . . 92
6.20 Energy distribution obtained from the truth data of simulated muons before the absorber. . . . 92
6.21 Comparison of the energy distribution of MC truth data and reconstructed of muons before the absorber. . . . 93
6.22 Comparison of the energy distribution of MC truth data and reconstructed of muons before the absorber. . . . 93
6.23 Reconstructed Energy distribution after the absorber. . . . 94
6.24 Energy distribution obtained from the truth data of simulated muons after the absorber. . . . 94

6.25 Comparison of the energy distribution of MC truth data and reconstructed of muons after the absorber. 95
6.26 Comparison of the energy distribution of MC truth data and reconstructed of muons after the absorber. 96
6.27 Difference between simulated and reconstructed muon energy before absorber for empty set data. 96
6.28 Difference between simulated and reconstructed muon energy after absorber for empty set data. 97
6.29 Simulated energy loss in the LiH absorber measured from MC truth data either side of the absorber. 98
6.30 Energy loss of simulated muons with no absorber in the cooling channel. . 98
6.31 Comparison between monte carlo energy loss and energy loss reconstructed from time-of-flight of muons in the cooling channel with no absorber material. 99
6.32 Simulated energy loss in the LiH absorber measured from MC truth data either side of the absorber. 100
6.33 Simulated energy loss in the LiH absorber reconstructed from TOF data. . 100
6.34 Reconstructed energy loss and energy loss from monte carlo truth data. . . 101
6.35 Figure 6.34 plotted on logarithmic scale to show similarities in the tail towards high Energy losses. 101
6.36 Momentum of muons at TOF1 vs the energy loss observed from the absorber. 102
6.37 Difference between TKU momentum and reconstructed momentum from TOF1 data before absorber. 103
6.38 Energy of muons reconstructed prior to the absorber. 104
6.39 Energy of muons reconstructed after to the absorber. 104
6.40 Energy loss of 200MeV/c Muons in the absorber cell without the LiH absorber. Measured using time of flight information obtained from the TOF detectors. 105
6.41 Momentum of muons at TOF1 vs the energy loss observed from the absorber. 106
6.42 Time of flight between TOF0 and TOF1. 107
6.43 Energy of muons reconstructed prior to the absorber. 107
6.44 Momentum of muons at TOF1 vs the momentum of muons reconstructed prior to the absorber. 108
6.45 Momentum of muons at TOF1 vs the energy loss observed from the absorber. 108
6.46 Energy loss of 200MeV/c Muons in 65mm of LiH and the absorber cell. Measured using time of flight information obtained from the TOF detectors. 109

List of Tables

2.1 Best fit values and 3σ allowed ranges of the 3-neutrino oscillation parameters, taken from the Particle Data Group review 2014[14]. Values (values in brackets) correspond to the $m_1 < m_2 < m_3$ ($m_3 < m_1 < m_2$) mass hierarchies. Δm^2 is defined as: $\Delta m^2 = m_3^2 - (m_2^2 + m_1^2)/2$. Therefore this gives $\Delta m^2 > 0$ for $m_1 < m_2 < m_3$, and $\Delta m^2 > 0$ for $m_3 < m_1 < m_2$. 8

3.1 Horizontal dispersion and the intrinsic emittances of the Step I beams. Dispersion is defined as the change in particle position with a fractional momentum offset. [18] 23

5.1 Descoped currents used in the Step IV simulation. 51

5.2 Results from the simulated Step IV analysis. The first column is the "Most Probable" energy loss, and the second is the average energy loss across the distribution. 75

6.1 Results of Energy Loss by 200MeV/c Muons from 65mm Lithium Hydride. 109

6.2 Results from the field off simulated Step IV experiment. 110

Chapter 1

Introduction

In order to progress the study of Neutrinos to new frontiers, new experiments must be designed that can produce a well understood, high intensity beam of neutrinos. Towards this end, the Muon Ionisation Cooling Experiment (MICE) has been commissioned to investigate the feasibility and performance of ionisation cooling, with regards to future application in a Neutrino Factory or Muon Collider. Ionisation cooling involves reducing the momentum of a particle in all directions by passing it through an absorber, before re-accelerating the particle in one direction. The first chapter of this thesis outlines the current status of neutrino physics, and why a neutrino factory is desirable. Chapter 2 describes beam physics and ionisation cooling in the MICE experiment, followed by a description of the detectors and equipment used in the MICE cooling channel.

A key process of ionisation cooling is the energy loss of muons as they pass through the absorber. Precise measurements of the energy loss can help to improve the accuracy of the emittance reduction, and these measurements make up the topic of this thesis. Chapter 3 describes the theory of ionisation energy loss as developed by notable names such as Bethe and Landau, and the Bethe equations are used to calculate the potential muon energy loss seen in the MICE experiment from the Lithium Hydride absorber.

The next 2 chapters describe and implement two methods of measuring the energy loss in the absorber. The first method involves using the data from the MICE trackers to measure the muon momentum either side of the absorber, and make a measurement of the energy loss. This requires that the experiment has field in both solenoid magnets in order for momentum reconstruction to work. The second method involves using time-of-flight data to measure the particle velocity before the absorber, and reconstruct the velocity after the absorber. This second method is particularly useful as this does not require field in

the cooling channel. Monte Carlo simulations are used to demonstrate the performance of both methods of measuring the energy loss, and data collected in the MICE channel without field is used to make a measurement of the energy loss in Lithium Hydride for the first time.

Chapter 2

Neutrino Physics

2.1 History

The neutrino was first proposed by W. Pauli [19] as a solution to explain conservation of energy, momentum and angular momentum during a beta-decay . The proposed particle was very light, had neutral electrical charge, spin $\frac{1}{2}$, and was described by Pauli as a "terrible thing" because the proposed particle seemed to be undetectable.

In 1942, Wang Ganchang proposed in Physical review a process to detect neutrinos indirectly via beta capture [20], and in 1956 Frederick Reines and Clyde Cowan published results of the first detection of (anti)neutrinos, 26 years after Pauli's proposal [21]. Antineutrinos from a nuclear reactor interacted with the hydrogen nuclei through the mechanism:

$$\bar{\nu} + p^{+} \rightarrow n + e^{+} \tag{2.1}$$

the position will quickly annihilate with an electron, emitting 2 γ which are detectable. The neutron was captured by a cadmium nucleus again emitting a γ. These 3 γ-rays were detected using scintillators immersed in a target of water and cadmium chloride, with attached photomultiplier tubes (PMTs). Reines and Cowen were eventually awarded with a nobel prize in 1995 for their discovery of the neutrino.

In 1962 it was demonstrated that neutrinos produced in association with electrons differed from those produced from muons with results produced at Brookhaven by Leon M. Lederman, Melvin Schwartz and Jack Steinberger [22] in one of the first neutrino beam experiments. Pions were produced by colliding 15 GeV protons into a Beryllium target,

a 13.5m thick iron wall absorbed muons, and neutrinos were detected in a spark chamber from the interactions:

$$\nu_{mu} + n \rightarrow \mu^- + p \tag{2.2}$$

$$\bar{\nu_m} u + p \rightarrow \mu^+ + n \tag{2.3}$$

$$\nu_e + n \rightarrow e^- + p \tag{2.4}$$

$$\bar{\nu}_e + p \rightarrow e^+ + n \tag{2.5}$$

The experimented noted that the lack of electron showers in their detectors meant that these muon neutrinos must be different to previously observed electron neutrinos.

Finally with the observation of the tau particle in 1975 [23] it follows that another flavour of neutrino would exist that corresponded with the tau, and indeed the tau neutrino was discovered in 2000 by the DONuT collaboration [24]. This gives 3 neutrino flavours that correspond with the 3 leptons. Measurement of the Z^0 resonance peak width estimated the number of neutrino generations at $N_\nu = 2.92 \pm 0.05$, indicating that all flavours are accounted for where $2m_\nu < m_z$.

2.2 The Solar Neutrino Problem

Developments in the 1960s in modelling the fusion reactions within the Sun, and the development of detectors capable of detecting neutrinos through beta decay, it was possible to measure and predict the flux of neutrinos arriving at Earth from the Sun. The Homestake experiment [25] was the first to do this [25], and consisted of 380m^2 tank of perchloroethylene (C_2Cl_4), with the chlorine forming the nucleus target for neutrino capture, located 1478m underground in the Homestake Gold Mine. The reaction for neutrino capture is

$$\nu_e + {}^{37}Cl \rightarrow {}^{37}Ar + e^- \tag{2.6}$$

The Argon produced was collected by bubbling Helium through the tank, and the radioactive decay of the Argon was measured in a small gas counter. In this way the number of neutrinos could be measured. Surprisingly at the time, Davis' measurement of neutrinos over the lifetime of the experiment came to one third of the expected rate. After the scientific community ruled out errors in the calculations, this became known as the "Solar

Neutrino Problem".

Further experiments at the Super Kamiokande detector [26] observed a deficit in the ratio of muon neutrino to electron neutrino rate for neutrinos originating from the Sun. It was expected previously that pions in the atmosphere would decay via

$$\pi \rightarrow \mu + \nu_\mu \tag{2.7}$$

$$\mu \rightarrow e + \nu_e + \nu_\mu \tag{2.8}$$

resulting in twice the amount of muon neutrinos than muon neutrinos. However, too few muon neutrinos were observed to match this ratio. Furthermore, the atmospheric neutrino rate was affected on the angle that the neutrino entered the detector. As the angle was dependant on the position of Super Kamiokande relative to the Earth, this was the first indication of dependence on path length of the neutrino rate.

These discoveries led to the development of theories suggesting that neutrinos were capable of oscillating between flavours, with the other flavours not being detected. For example the Homestake experiment would not detect ν_μ, it only detected ν_e. However, the SNO (Sudbury Neutrino Observatory), consisting of 1000 tonnes of heavy water viewed by 9600 PMTs, could differentiate between 3 different neutrino interactions:

$$\nu_e + d \rightarrow p + p + e^- \tag{2.9}$$

$$\nu_x + d \rightarrow \nu_x + p + n \tag{2.10}$$

$$\nu_x + e^- \rightarrow \nu_x e^- \tag{2.11}$$

where equation 2.9 is a Charged Current interaction, equation 2.11 the Neutral Current, and 2.11 elastic scattering. In particular, the Charged Current interaction was only attainable by ν_e, whereas the Neutral Current was equally achievable by all flavours. Through this, SNO was able to demonstrate that the total flux of solar neutrinos was in agreement with predictions from the Standard Solar Model [27], however the Charged Current rate was one third of the expectation due to no models predicting ν_μ or ν_τ production in the Sun. Therefore this was clear evidence that the flavour of the neutrino was changing between the Sun and the detector.

In 2015 Takaki Kajita from Super-Kamiokande Observatory and Arthur McDonald from SNO were both awarded the 2015 Nobel Prize for Physics, an indication of the acceptance of the theory of Neutrino Oscillations and their significant impact on modern physics and the experimental outlook.

2.3 Neutrino Oscillation Formulation

The quantum mechanics supporting neutrino oscillation was developed primary by the quartet of Pontecorvo, Maki, Nakagawa, and Sakata [28]. Neutrino Oscillation is described in this theory as a phenomenon whereby a neutrino with one particular weak flavour eigenstate can be detected later in time with a different weak flavour eigenstate. This is made possible by the fact the flavour eigenstate of the neutrino immediately after it has undergone a weak interaction is not the same as the mass eigenstate, but instead the flavour eigenstates are considered a mixture of the mass eigenstates. Following the description given in [29], [30]:

$$|\nu_\alpha\rangle = \sum_k U_{\alpha k}|\nu_k\rangle \tag{2.12}$$

where $|\nu_\alpha\rangle$ are the flavour states where $\alpha = e, \mu, \tau$, $|\nu_k\rangle$ are the mass eigenstates with $k = 1, 2, 3$ and U is the PMNS matrix:

$$U = \begin{pmatrix} c_{12}c_{13} & s_{12}c_{13} & s_{13}e^{-i\delta} \\ -s_{12}c_{23} - c_{12}s_{23}s_{13}e^{i\delta} & c_{12}c_{23} - s_{12}s_{23}s_{13}e^{i\delta} & s_{23}c_{13} \\ s_{12}s_{23} - c_{12}c_{23}s_{13}e^{i\delta} & -c_{12}s_{23} - s_{12}c_{23}s_{13}e^{i\delta} & c_{23}c_{13} \end{pmatrix} \tag{2.13}$$

where $c_{ab} = \cos\theta_{ab}$, $s_{ab} = \sin\theta_{ab}$. θ_{12}, θ_{13} and θ_{23} are mixing angles between the different mass eigenstates, whilst δ is a CP violating phase.

The mass eigenstates are eigenstates of the Hamiltonian, and therefore the time dependance can be found by solving the Schrdinger equation. This gives:

$$|\nu_k(t)\rangle = e^{iE_k t}|\nu_k\rangle \tag{2.14}$$

Where E_k is the energy of the eigenstate expressed as $E_k = \sqrt{p^2 + m_k^2}$. This approximates

to $E_k \approx p + \frac{m_k^2}{2p}$ when assuming the neutrino momentum is much larger than the neutrino mass. So using this and equation 2.12 the mass eigenstate state vector becomes:

$$|\nu_\alpha(L)\rangle = \sum_k U*_{\alpha k}\, e^{-i(\frac{m_k^2}{2E})L}|\nu_k\rangle \tag{2.15}$$

Note we have also replaced $t = L$ where L is the distance travelled. The probability (P) that a neutrino changes flavour state from α to a final state β as a function of length is:

$$P_{\alpha\to\beta}(t) = |\langle\nu_\beta|\nu_\alpha(t)\rangle|^2 \tag{2.16}$$

$$P_{\alpha\to\beta}(t) = |\sum_k U*_{\alpha k}\, U_{\beta k} e^{-i\left(\frac{m_k^2}{2E}\right)L}|^2 \tag{2.17}$$

$$P_{\alpha\to\beta}(t) = \sum_k\sum_n U^*_{\alpha k} U_{\beta k} e^{-i\left(\frac{m_k^2}{2E}\right)L} U_{\alpha n} U^*_{\beta n} e^{+i\left(\frac{m_n^2}{2E}\right)L} \tag{2.18}$$

then let $\Delta m^2_{kn} = m_k^2 - m_n^2$ and equation 2.18 becomes:

$$P_{\alpha\to\beta}(L,E) \approx \sum_{k,n} U*_{\alpha k}\, U_{\beta k} U_{\alpha n} U*_{\beta n}\, exp\left(-i\frac{\Delta m^2_{kn} L}{2E}\right) \tag{2.19}$$

In many cases a two neutrino mixing is considered, where $U = R(\Theta)$, the two dimensional rotation matrix. This then yields the two dimensional oscillation probability equation:

$$P_{\alpha\to\beta}(L,E) = \sin^2(2\Theta)\sin^2\left(1.27\frac{\Delta m^2 L}{2E}\right) \tag{2.20}$$

Where now m is measured in eV, L in km, and E in GeV.
In the three-flavour case, then the Unitary matrix indeed becomes the PMNS matrix expressed in equation 2.13, and is given by [31]:

$$\begin{aligned} P_{\alpha\to\beta}(L,E) = \delta_{\alpha\beta} & \\ & -4\sum_{kn}\Re(K_{\alpha\beta kn})\sin^2\left(\frac{\Delta m^2_{kn} L}{4E}\right) \\ & +4\sum_{kn}\Im(K_{\alpha\beta kn})\sin\left(\frac{\Delta m^2_{kn} L}{4E}\right)\cos\left(\frac{\Delta m^2_{kn} L}{4E}\right) \end{aligned} \tag{2.21}$$

Parameter	best-fit($\pm 1\sigma$)	3σ
$\Delta m^2_{21}[10^{-5}eV^2]$	$7.54^{+0.26}_{-0.22}$	6.99 - 8.18
$\lvert\Delta m^2\rvert[10^{-3}eV^2]$	$2.43 \pm 0.06 (2.38 \pm 0.06)$	$2.23 - 2.61 (2.19 - 2.56)$
$\sin^2\theta_{12}$	0.308 ± 0.017	$0.259 - 0.359$
$\sin^2\theta_{23}, \Delta m^2 > 0$	$0.437^{+0.033}_{-0.023}$	$0.347 - 0.628$
$\sin^2\theta_{23}, \Delta m^2 < 0$	$0.455^{+0.039}_{-0.031}$	$0.380 - 0.641$
$\sin^2\theta_{13}, \Delta m^2 > 0$	$0.0234^{+0.0020}_{-0.0019}$	$0.0176 - 0.0295$
$\sin^2\theta_{13}, \Delta m^2 < 0$	$0.0240^{+0.0019}_{-0.0022}$	$0.0178 - 0.0298$
δ/π	$1.39^{+0.38}_{-0.27}$	$(0.00 - 0.16) \oplus (0.86 - 2.00)$

Table 2.1: Best fit values and 3σ allowed ranges of the 3-neutrino oscillation parameters, taken from the Particle Data Group review 2014[14]. Values (values in brackets) correspond to the $m_1 < m_2 < m_3$ ($m_3 < m_1 < m_2$) mass hierarchies. Δm^2 is defined as: $\Delta m^2 = m_3^2 - (m_2^2 + m_1^2)/2$. Therefore this gives $\Delta m^2 > 0$ for $m_1 < m_2 < m_3$, and $\Delta m^2 > 0$ for $m_3 < m_1 < m_2$.

where $K_{\alpha\beta kn} = U_{\alpha k} U^*_{\beta k} U^*_{\alpha n} U_{\beta n}$.

2.4 Neutrino Oscillation Experimental Results

Neutrino physics experiments in recent years have focussed on making precision measurements of the parameters of the PMNS matrix in equation 2.13, as well as measurements to determine the absolute neutrino mass scale and whether the neutrino is a Dirac or Majorana particle.

To determine the neutrino mixing, experiments utilise a known neutrino source such as a nuclear reactor, an accelerator or the atmosphere, followed by at least one distant detector which can measure the neutrino flux. Some experiments also use a detector close to the neutrino source, which gives a measure of the neutrino flux before any oscillation can take place. Sensitivity of an experiment is determined by L/E, due to the oscillations dependence on both these values. The T2K experiment is a good example of this [32]. A 30 GeV proton beam incident on a graphite target generates primarily ν_μ towards the Super-Kamiokande detector. There is a near detector 280m from the source, and the far detector 295km. Published results in 2013 demonstrated ν_e appearance in the far detector to greater accuracy.

From T2K, and various other studies, limits on the PMNS parameters have been measured and are summarised in table 2.1. Data from T2K [33], MINOS[34] and DayaBay [35] in particular have allowed the 3-oscillation parameters Δm^2_{21}, θ_{12}, $|\Delta m^2_{31}|$, $|\Delta m^2_{32}|$, θ_{23} and θ_{13} to be determined with relatively high precision. However so far there the mass hierarchy

has not been determined.

2.4.1 Mass Heirachy

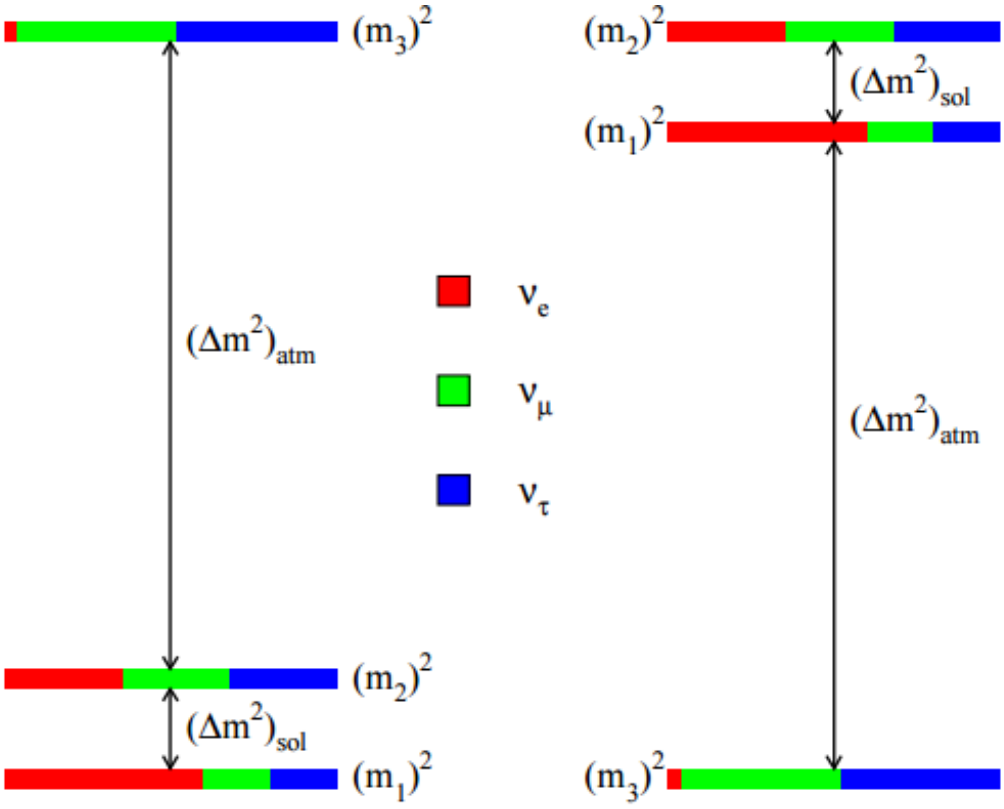

Figure 2.1: The neutrino mass hierarchy. Populations of each flavour in each mass eigenstate are indicated by colour: ν_e in red, ν_μ in green and ν_τ in blue.

Although values for the squared difference of the mass eigenstates are becoming better known, what is not yet clear is the sign of the differences, in particular whether Δm^2_{13} is positive or negative. One way to study is to focus on $\nu_\mu \rightarrow \nu_e$ oscillations, governed by the sign of Δm_{13}, which is the approach taken in experiments such as T2K. T2K can make this measurement by measuring $sin^2\theta_{13}$ with both neutrino and anti-neutrino beams. However, other experiments aim to determine the Mass Hierarchy through the double beta decay process.

2.5 Double beta decay

Double beta decay is a rare occurring process where two neutrons undergo beta decay simultaneously. The standard Double beta decay mode ($2\nu\beta\beta$) occurs where a nucleus

with Z protons decays to a nucleus with Z + 2 protons and keeps the same mass number A. The standard decay mode of $2\nu\beta\beta$ can also be thought of as 2 simultaneous beta decays, and was first considered by Maria Goeppert-Mayer in 1935 [36].

$$(Z,A) \rightarrow (Z+2,A) + 2e^- + 2\overline{\nu}_e \tag{2.22}$$

Whereas Neutrinoless double beta decay ($0\nu\beta\beta$) is a theoretical decay mode proposed by W. H. Furry to test Majorana's theory for neutrinos.[37]

$$(Z,A) \rightarrow (Z+2,A) + 2e^- \tag{2.23}$$

The $0\nu\beta\beta$ mode violates lepton number conservation and is currently forbidden in the Standard Model. However, if observed, then it provides direct evidence that the neutrino is a Majorana particle, which is to say that it is its own anti-particle. Feynman diagrams showing both modes of the decay are shown in figure 2.2.

If $0\nu\beta\beta$ is observed, the rate of $0\nu\beta\beta$ events will be very sensitive to the absolute neutrino mass hierarchy. Experiments such as SuperNEMO are looking for the decay but with little success so far. One collaboration (Heidelberg-Moscow) has published results suggesting they found a $0\nu\beta\beta$ signal [38], however the result has attracted criticism due to the comparison between their proposed $0\nu\beta\beta$ signal and background events from the Bismuth background. $2\nu\beta\beta$ has however been experimentally observed in multiple experiments.

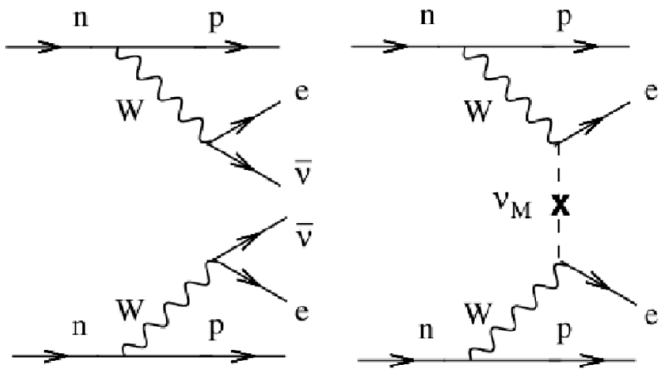

Figure 2.2: Feynman diagrams showing $2\nu\beta\beta$ on the left, and $0\nu\beta\beta$ with the virtual neutrinos on the right [1].

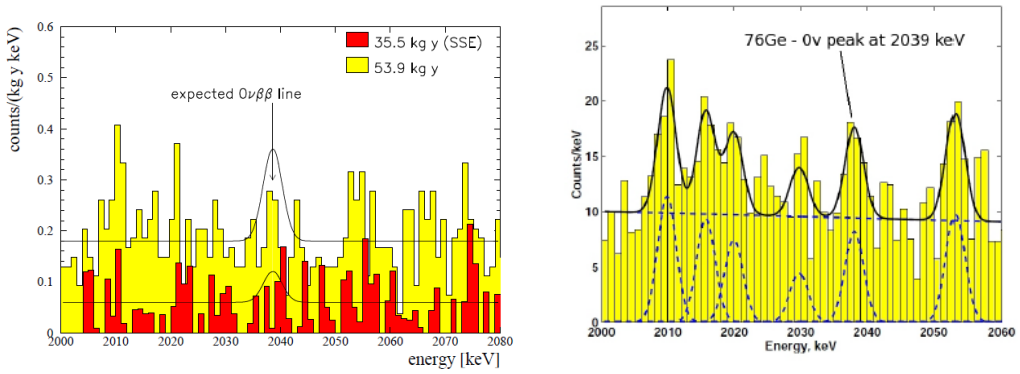

(a) Observed spectrum around the expected $0\nu\beta\beta$ peak announced by the Heidelberg-Moscow collaboration [39]. The two different spectra correspond to measuring periods with (red) and without (yellow) pulse shape discrimination, which is used to distinguish between a single charge deposition in the Ge crystal (such as double beta decay), and several charge depositions (such as Compton Scattering, a major background).

(b) The claimed $0\nu\beta\beta$ signal at 2039keV from a group within the collaboration [38]. Peaks at 2011, 2017, 2022 and 2053 keV correspond to ^{214}Bi background. The peak at 2030keV is unidentified.

Figure 2.3: Comparison of the two main results from the Heidelberg-Moscow experiment, one showing no peak in the $0\nu\beta\beta$ region, and the 'controversial' result with the $0\nu\beta\beta$ peak on the right. Decays of interest have an energy peak at a region of 2039 KeV which could not match the signal for a single beta decay.

2.6 Neutrino Factory

Current experiments in the Neutrino sector suffer from low sensitivity to Neutrinos due to the small cross section of the neutrino, and an unpredictable rate from the source. This will be corrected by proposed Neutrino Factory experiments, which will aim to boost the sensitivity of Neutrino experiments to something comparable to the quark sector. This will be achieved by producing a high intensity beam of neutrinos produced from muon decay.

From the International Design Study (IDS-NF) for a neutrino factory [2], a high power proton driver and target generate pions, which are captured by a 20T solenoid field. The pions decay into muons quickly, and these muons must have proper conditions before acceleration. A "bunching and phase rotation" section will reduce the energy spread of the beam, and an ionisation cooling section will reduce the transverse emittance of the beam. Then a series of accelerators will increase the beam energy from 120MeV up to 10GeV. Finally the muons enter a storage ring with long straight sections that store the beam for about 1000 turns. A schematic of the proposal is shown in figure 2.4. Knowing the content of the muon beam inside the storage ring allows the absolute flux of the neutrino beam to be measured with small systematics. The current optimisation of the

Neutrino Factory allows for one 100 kton Magnetised Iron Neutrino Detector (MIND) at approximately 2000km from the factory.

Feasibility studies [40] have been carried out to assess the technical challenges behind

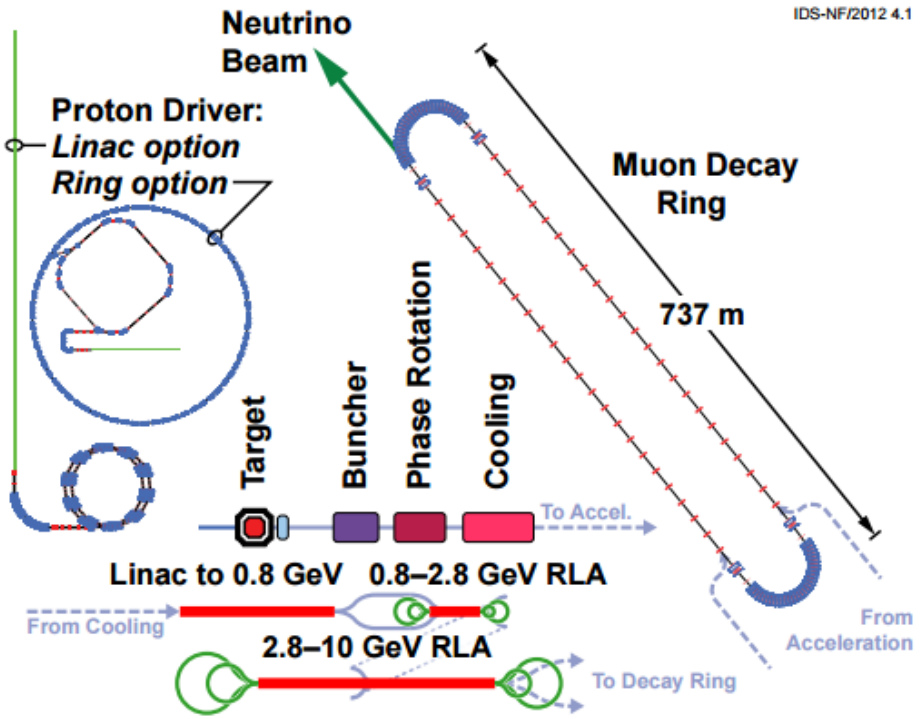

Figure 2.4: Schematic drawing of the proposed Neutrino Factory by the IDS-NF collaboration.[2]

the Neutrino factory. In particular, to achieve the desired muon production benchmarks it is important to maximise the transmission of the muons to the decay rings, through reduction of the beam emittance. This will be achieved through the ionisation cooling channel, comprised of repeated cells of absorbers which reduce the muon momentum in both transverse and longitudinal directions, and RF cavities which reintroduce longitudinal momentum to the beam, thereby reducing the transverse emittance. This concept has not been tested experimentally, so therefore the Muon Ionisation Cooling Experiment (MICE) was commissioned to demonstrate ionisation cooling in one cooling channel. MICE is explored further in the next chapter.

Chapter 3

The Muon Ionisation Cooling Experiment

The Muon Ionisation Cooling Experiment (MICE) has been commissioned at RAL to demonstrate the feasibility of ionisation cooling, designed using a section of cooling channel proposed in the feasibility study [40]. The investigation of ionisation cooling carried out by MICE may later be used in Neutrino Factory facility, and subsequent Muon accelerators and colliders [41]. When complete, MICE is designed to provide a 10% decrease in muon beam emittance measurable to 0.1% or better for a range of muon momenta between 140 MeV/c and 240 MeV/c. Emittance is a description of the phase space occupied by the beam, and is described below.

The chapter will provide a brief overview of the beam physics behind ionisation cooling, followed by a description of the components and development of MICE.

3.1 Emittance

The Neutrino Factory design [40] requires a muon beam that is “small” enough to fit into the acceptance of the acceleration system. The measure of this ”smallness” is described in accelerator physics by the concept of emittance. Emittance is a description of the phase space volume of the beam. Here I will provide a basic description of emittance as defined by MICE, followed by its reduction via ionisation cooling.

To begin, we define that the phase space of a particle in 2D consists of a spacial coordinate x, and its momentum p_x. The particle is moving longitudinally along the z axis with momenta p_z. For the purpose of measuring emittance, we then define the transverse phase space, or the trace space, by transforming the momenta by:

$$x' = \frac{p_x}{p_z} = \frac{dx}{dz} \tag{3.1}$$

Similarly, one could also define the phase space in 4D by adding the y components of space and momenta, and then also defining

$$y' = \frac{p_y}{p_z} = \frac{dy}{dz} \tag{3.2}$$

So now x' and y' represent the divergence of the particle trajectory away from the z-axis of the beam. Remaining in 2D for now, the area of the trace space occupied by the beam can be expressed as an integral:

$$\varepsilon = \frac{1}{\pi}\int x' dx = \frac{A}{\pi} \tag{3.3}$$

Generally in 2D the beam distribution represented in trace space takes the form of the ellipse, shown in figure 3.1. The equation that describes the ellipse is known as the Courant-Snyder invariant and is given by:

$$\varepsilon = \gamma x^2 + 2\alpha x x' + \beta x'^2 \tag{3.4}$$

Where α,β, and γ are the Twiss parameters defined as normal:

$$\alpha = \frac{< xx' >}{\varepsilon} \tag{3.5}$$

$$\beta = \frac{x'^2}{\varepsilon} \tag{3.6}$$

$$\gamma = \frac{x^2}{\varepsilon} \tag{3.7}$$

And ε is the quantity of the area of the beam in trace space, or the emittance of the beam.

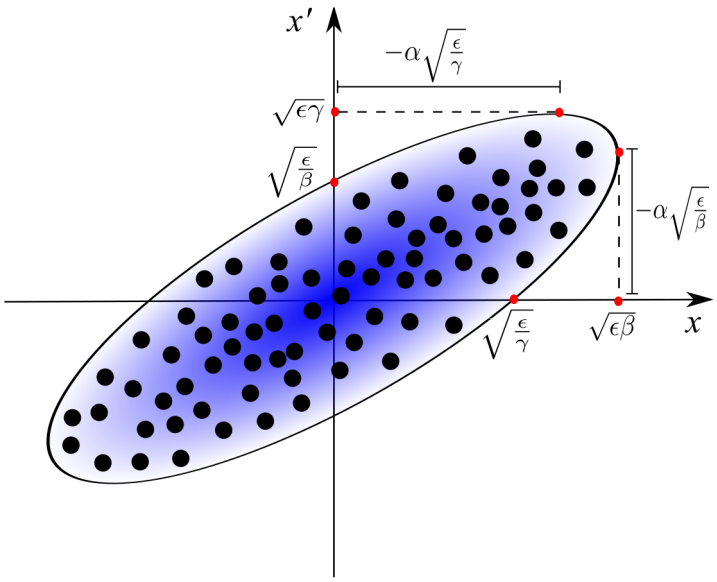

Figure 3.1: Trace space plot of an elliptical beam taken at a single point in time. The area of the ellipse is defined as the emittance ε, whilst α,β and γ are the Twiss parameters.[3]

Through the ellipse geometry, the Twiss parameters are related as per equation 3.8.

$$\beta\gamma - \alpha^2 = 1 \tag{3.8}$$

The equation for ellipse of any number of dimensions in matrix form is

$$u^T \sigma^{-1} u = 1 \tag{3.9}$$

Where σ is a symmetric matrix not yet defined. In two dimensions only, u becomes $\begin{pmatrix} x & x' \end{pmatrix}$ and therefore equation 3.9 becomes:

$$\begin{pmatrix} x & x' \end{pmatrix} \frac{1}{\Delta} \begin{pmatrix} \sigma_{22} & -\sigma_{12} \\ -\sigma_{21} & \sigma_{11} \end{pmatrix} \begin{pmatrix} x \\ x' \end{pmatrix} = 1 \tag{3.10}$$

where Δ is the determinant of the matrix σ.
Note $\sigma_{21} = \sigma_{12}$ as σ is symmetric, by property it is covariant, and so finally this becomes

$$x^2\sigma_{22} - 2xx'\sigma_{12} + x'^2\sigma_{11} = \Delta \tag{3.11}$$

which is the same form as equation 3.4. Therefore by substituting the Twiss parameters

where the elements of the σ matrix are, one can retrieve σ as:

$$\sigma = \varepsilon \begin{pmatrix} \beta & -\alpha \\ -\alpha & \gamma \end{pmatrix} \tag{3.12}$$

The twiss parameters can be used with equation 3.12 to express the beam size σ_x and divergence $\sigma_{x'}$:

$$\begin{aligned} \sigma_x &= \sqrt{\beta\varepsilon} \\ \sigma_{x'} &= \sqrt{\varepsilon/\beta} \end{aligned} \tag{3.13}$$

As an aside, one can now prove the relation 3.8 by the inverse matrix relation $\sigma\sigma^{-1} = I$, where I is the identity matrix:

$$\sigma\sigma^{-1} = \varepsilon \begin{pmatrix} \beta & -\alpha \\ -\alpha & \gamma \end{pmatrix} \frac{1}{\Delta}\varepsilon \begin{pmatrix} \gamma & \alpha \\ \alpha & \beta \end{pmatrix} = \frac{\varepsilon^2}{\Delta} \begin{pmatrix} \beta\gamma - \alpha^2 & \beta\alpha - \beta\alpha \\ -\gamma\alpha + \gamma\alpha & \beta\gamma - \alpha^2 \end{pmatrix} = \begin{pmatrix} 1 & 0 \\ 0 & 1 \end{pmatrix} = I \tag{3.14}$$

Now the area of the phase space in 2 dimensions can be defined as

$$Vol_{2D} = \pi\sqrt{|\sigma|} = \pi\sqrt{\varepsilon^2(\beta\gamma - \alpha^2)} = \pi\varepsilon \tag{3.15}$$

To bring this back to MICE emittance, it is important to define normalised emittance as an invariant quantity, given by:

$$\varepsilon_n = \beta_L\gamma_L\varepsilon = \frac{\varepsilon p}{m_0 c} \tag{3.16}$$

Where β_L and γ_L are Lorentz factors, not related to the Twiss parameters. Now the MICE 4D transverse normalised emittance can be expressed, and is given as quoted from the MICE technical reference document [42].

$$\varepsilon_n^{tran} = \frac{1}{m_\mu c}\sqrt{|V_{4D}(x,x',y,y')|} \tag{3.17}$$

And this is the quantity that MICE must reduce and measure.

3.2 Ionisation Cooling

Ionisation cooling [43] is the process where the total momentum of a particle beam is reduced by passing the beam through an absorber material, then the momentum is regained through longitudinal acceleration. Because muons only have a short lifetime of 2.2 μs, this method of beam cooling is the best proposed method to reduce the emittance of muons sufficiently to meet the conditions of a muon beam. Current alternative cooling technologies developed over over the past century involve relatively long timeframes, and hence are only suitable for stable particles (such as protons, electrons). Hence a new method is required for Muons.

Figure 3.2 shows in vector form how ionisation cooling works. The initial momentum of a muon has a certain transverse and longitudinal component. By passing the muon through an absorber, it undergoes energy loss through ionisation and loses momentum in all directions. Then the lost energy can be regained by acceleration through an RF cavity, but only in the longitudinal direction. This means that the final momentum with have a relatively greater longitudinal component, and hence the emittance has been reduced.

One process that acts against cooling is multiple scattering. Unfortunately, scattering will also occur as part of the ionisation energy loss process, and also may happen any time a muon passes through a material. Scattering will cause the beam emittance to increase, referred to as heating the beam.

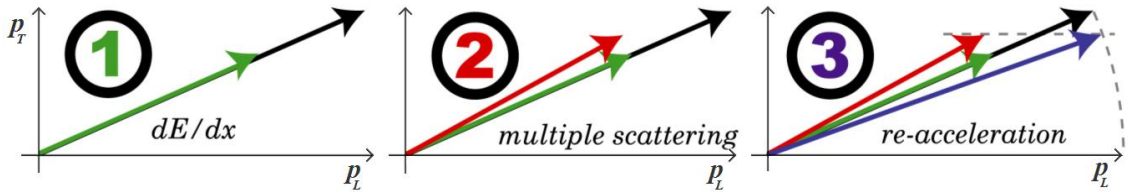

Figure 3.2: Graphical representation of emittance reduction. In the first figure, the overall momentum vector of the muon is reduced. Then the heating effect of scattering is considered, which increases the transverse component of the momentum vector. Finally, the beam is accelerated in the longitudinal direction. Overall, the transverse momentum is reduced and the proaxial momentum is maintained.

The effects of scattering and energy loss on the emittance of the muon beam are best described with the cooling equation [42]. Starting with the equation for normalised transverse emittance in equation 3.16, the rate of change of emittance for a beam moving through a material becomes:

$$\frac{d\varepsilon_n}{dz} = \frac{1}{m}\frac{dp}{dz}\sigma_x\sigma_x' + \frac{p}{m}\sigma_x\frac{d\sigma_{x'}}{dz} \tag{3.18}$$

which contains both a cooling term ($\frac{dp}{dz}$) and a scattering term ($\frac{d\sigma_{x'}}{dz}$). The $\frac{dp}{dz}$ term can be instead expressed in terms of the energy loss per length by substituting the dp terms for dE using:

$$E^2 = p^2 + m^2 \tag{3.19}$$

$$dp = \frac{E}{p} dE \tag{3.20}$$

thus

$$\frac{dp}{dz} = \frac{E}{p}\frac{dE}{dz} = \frac{1}{\beta}\frac{dE}{dz} \tag{3.21}$$

substituting this into equation 3.18 returns

$$\frac{d\varepsilon_n}{dz} = \frac{\varepsilon_n}{p\beta}\frac{dE}{dz} + \frac{p}{m}\sigma_x\frac{d\sigma_{x'}}{dz} \tag{3.22}$$

the scattering term can be redefined using the differential of $d\sigma_{x'}^2$ to give

$$\frac{d\sigma_{x'}^2}{dz} = 2\sigma_{x'}\frac{d\sigma_{x'}}{dz} \tag{3.23}$$

and this is again substituted into equation 3.22 to give

$$\frac{d\varepsilon_n}{dz} = -\frac{\varepsilon_n}{p\beta}\frac{dE}{dz} + \frac{p}{m}\sigma_x\frac{1}{2\sigma_{x'}}\frac{d\sigma_{x'}^2}{dz} \tag{3.24}$$

Earlier the definitions for σ_x and $\sigma_{x'}$ were given in equation 3.13. Substituting these in gives a general formula for cooling as:

$$\frac{d\varepsilon_n}{dz} = -\frac{\varepsilon_n}{p\beta}\frac{dE}{dz} + \frac{p}{m}\frac{\beta_\perp}{2}\frac{d\sigma_{x'}^2}{dz} \tag{3.25}$$

Generally, and as defined by MICE, the formula for cooling is given with an approximation term for the multiple scattering effect [44].

$$\frac{d\langle\theta_0^2\rangle}{dz} = \frac{d\sigma_{x'}^2}{dz} = \left(\frac{13.6MeV}{p\beta}\right)^2\frac{1}{X_0} \tag{3.26}$$

where $\Delta z/X_0$ is the fraction of radiation length of the absorber. This can be substituted

into equation 3.27, along with the relativistic expressions for $p = \gamma\beta m_\mu c$ and $E = \gamma m_\mu c$ to obtain the standard cooling formula.

$$\frac{d\varepsilon_n}{dz} = -\frac{\varepsilon_n}{\beta^2 E}\frac{dE}{dz} + \frac{\beta_\perp (13.6MeV)^2}{2\beta^2 E m_\mu X_0} \tag{3.27}$$

The final cooling formula, has the first term representing the cooling due to energy loss (the dE/dz term) and heating due to multiple scattering (the second term). It shows that an effective cooling channel will seek to maximise the energy loss, whilst minimising the multiple scattering effect.

3.3 MICE Experimental Setup

The original plan for MICE was that it would be a staged experiment. After each stage data would be collected and analysed to allow the effects of each new component to be measured. Figure 3.3 shows what these stages were to look like. In the first stage (Step I), the cooling channel of MICE only consisted of two TOF detectors, and the cherenkov detectors. This allowed for particle identification to take place, and a lot of characterisation of the beam was done with this data. Due to various delays and setbacks with the experiment, the decision was later made to jump straight to Step IV data taking, which is the status of MICE at the time of writing. Step IV consists of the two tracker units either side of an absorber module. In theory, this is an ideal time to take measurements relating to the absorber material, as the position of the trackers means that measurements of muon properties can be taken immediately before and after the absorber.

3.3.1 Step IV

A schematic of the Step IV cooling channel is shown in figure 3.4. In this configuration, the cooling channel consists of 3 time-of-flight detectors TOF0, TOF1 and TOF2 with TOF0 and 1 positioned at the start of the beam, and TOF2 at the end. Next to TOF1 are the cherenkov detectors, and they work with TOF0 and TOF1 to provide particle identification at the start of the beam. The time of flight from TOF0 to TOF1 can also provide information about the muon momentum.

In the center of the channel lies the absorber unit, consisting of the absorber focus coil magnet, with the absorber inside. Either side are situated the solenoid magnets that house the upstream and downstream trackers, which are used to return detailed information

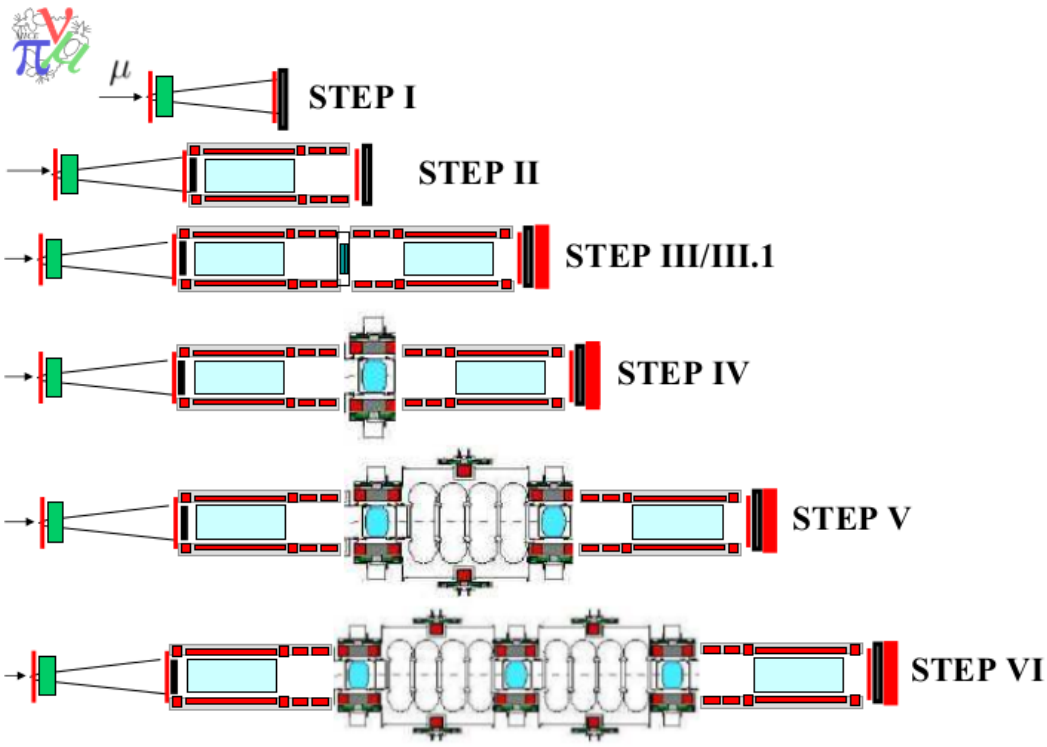

Figure 3.3: The original MICE staged plan. Step I would consist of a muon beamine, the first two TOF detectors and the Cherenkov detector to allow for PID. Step II and III introduce the trackers. Step IV introduces an absorber module, along with the focus coil. Step V and VI would finally add the RF cavities and additional absorbers to complete the demonstration.

about the muon tracks. At the end of the beam lies the KL and EMR detectors. These are used for particle identification at the end of the beam, and are particularly useful for identifying particles that have decayed inside the beam line (for example a muon decaying to an electron/neutrino).

3.3.2 The Demonstration of Ionisation Cooling

During preparation for Step IV running, damage occurred to the downstream solenoid which has potentially made it unsuitable for future steps of the experiment without an expensive repair. At the time of writing, work is currently ongoing to find new potential setups for MICE that will still allow for a full demonstration of ionisation cooling that includes re-acceleration with the RF cavities. Such solutions involve using only one of the solenoid magnets to take a measurement one side of the cooling, and a combination of other detectors to make alternative measurements. Two of proposed lattice are shown in figure 3.5, and studies are ongoing to find an optimal solution.

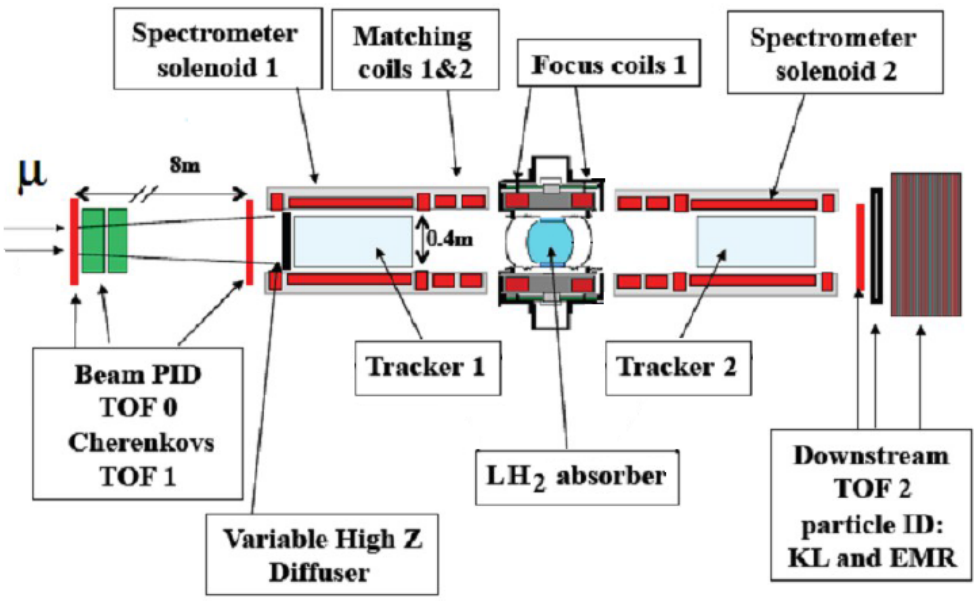

Figure 3.4: Schematic of the MICE Step IV cooling channel.

3.4 Muon Beamline

The MICE beamline obtains its muons by feeding off the ISIS synchrotron at the Rutherford Appleton Laboratory (RAL) in Oxfordshire, as shown in figure 3.6. A Titanium target dips into the ISIS beam at a frequency of a few Hz, producing pions and protons [45]. These leave the ISIS vacuum chamber through a small window, and some are captured by the first quadrupole magnets Q1-3 [46], shown on figure 6.7. This triplet of quadrupoles transports the particles to the first Dipole magnet, D1, which directs the beam into the MICE hall itself. Tuning D1 to different strengths allows MICE to capture Pions of various momenta. Following D1, the particles pass through the 5T decay solenoid, which increases the pion path length resulting in about 10 times more muons in the cooling channel than without[47]. A second dipole magnet provides selection of muon momenta, and directs the beam trajectory towards the cooling channel.

After this point there is another pair of quadrupole triplets, Q4-6, and Q7-9 which transport the beam to the diffuser [48]. This is designed to increase the emittance of the beam. Therefore, through a combination of the quadrupole and dipole currents, a range of muon beam emittance values between 1 and 12 mm rad can be achieved with a momentum range of 140-240MeV [49]. During Step 1 running of MICE 17 distinct beam settings were characterized for use, and are described in table 3.1 [18].

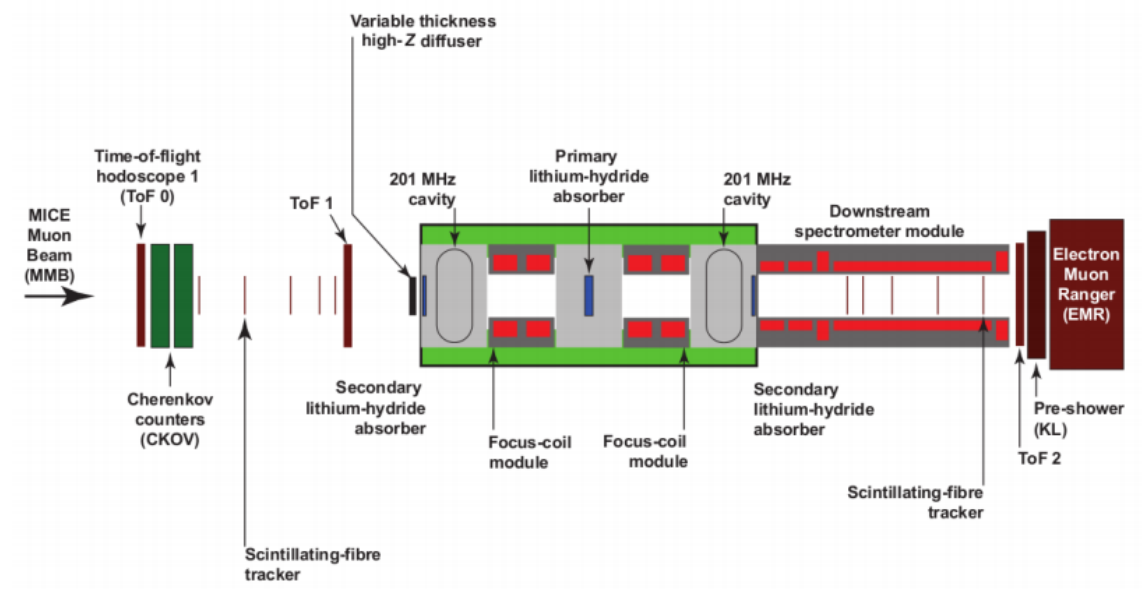

(a) Spectrometer after absorber

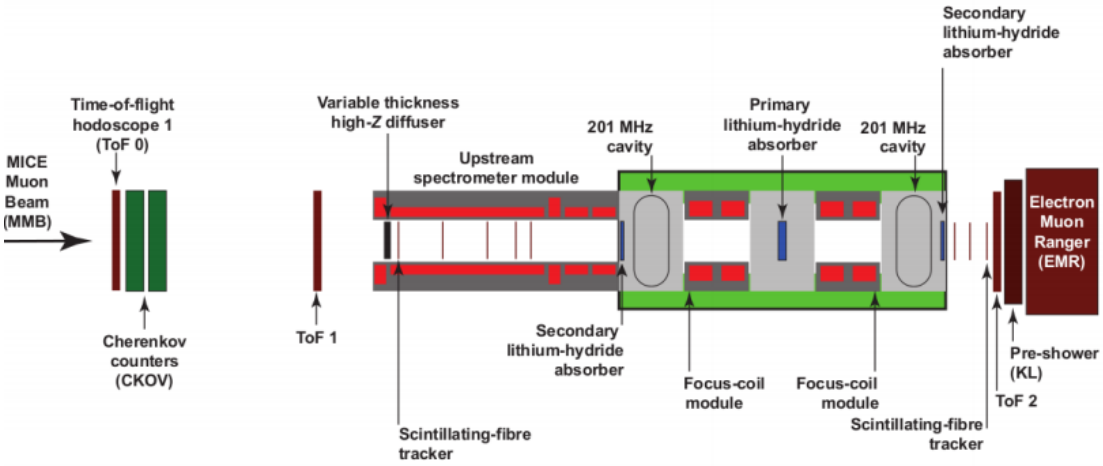

(b) Spectrometer before absorber

Figure 3.5: Some proposed descope options for the demonstration of ionisation cooling.

	Beam		η_x (mm)	η'_x (rad)	ε_x (π mm-rad)	α_x	β_x (m)
	ε_N	p_z					
μ^-	3	140	90.28	0.07	2.08±0.11	0.60±0.01	1.56±0.09
		200	123.78	0.09	1.53±0.08	0.65±0.01	1.82±0.10
		240	137.58	0.11	1.26±0.07	0.68±0.01	1.99±0.11
	6	140	89.37	0.08	1.97±0.11	0.64±0.01	1.66±0.09
		200	106.27	0.10	1.31±0.07	0.72±0.01	2.06±0.12
		240	157.91	0.11	1.26±0.07	0.68±0.01	1.98±0.11
	10	140	96.03	0.07	1.83±0.10	0.64±0.01	1.71±0.10
		200	132.78	0.08	1.04±0.06	0.79±0.01	2.47±0.14
		240	145.71	0.11	1.40±0.08	0.75±0.01	2.02±0.12
μ^+	3	200	122.96	0.03	1.85±0.10	0.56±0.00	1.58±0.09
		240	156.47	0.03	1.45±0.08	0.66±0.01	1.87±0.11
	6	140	95.91	0.04	2.18±0.12	0.52±0.00	1.51±0.09
		200	131.16	0.04	1.76±0.09	0.58±0.00	1.62±0.09
		240	172.97	0.04	1.54±0.08	0.64±0.01	1.76±0.10
	10	140	103.27	0.04	2.03±0.11	0.54±0.01	1.57±0.09
		200	138.50	0.03	1.53±0.08	0.59±0.01	1.78±0.10
		240	189.64	0.04	1.61±0.09	0.61±0.01	1.64±0.09

Table 3.1: Horizontal dispersion and the intrinsic emittances of the Step I beams. Dispersion is defined as the change in particle position with a fractional momentum offset. [18]

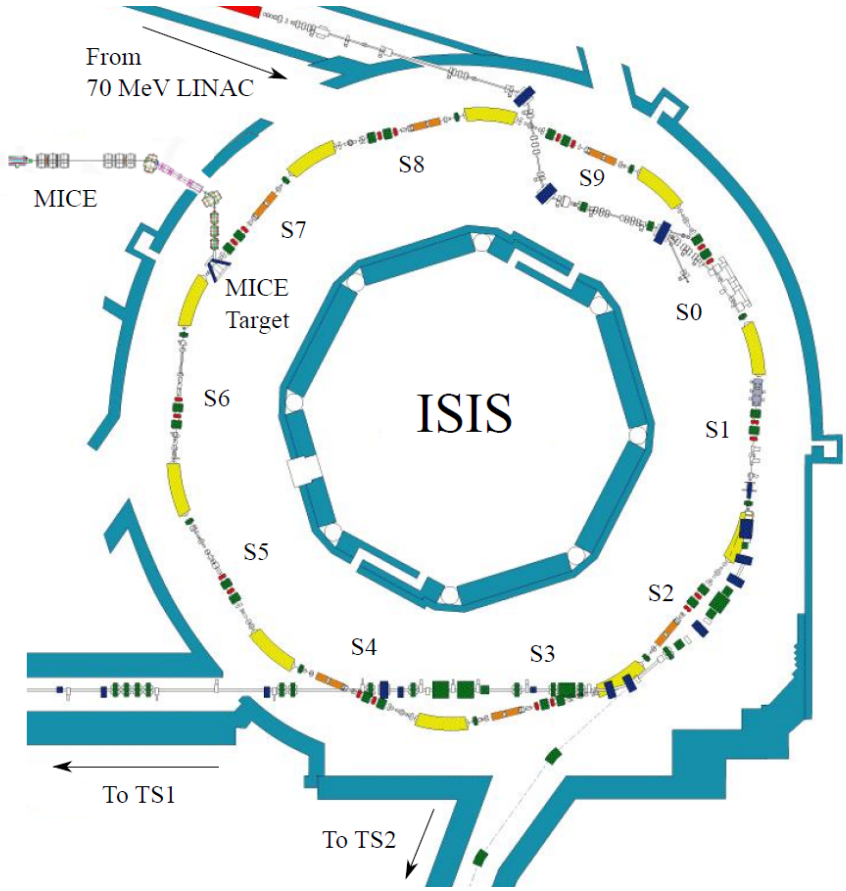

Figure 3.6: MICE uses a Titanium target in the ISIS syncrotron between stations S6 and S7 to produce pions. These are captured by quadropole magnets and transported to the MICE cooling channel.

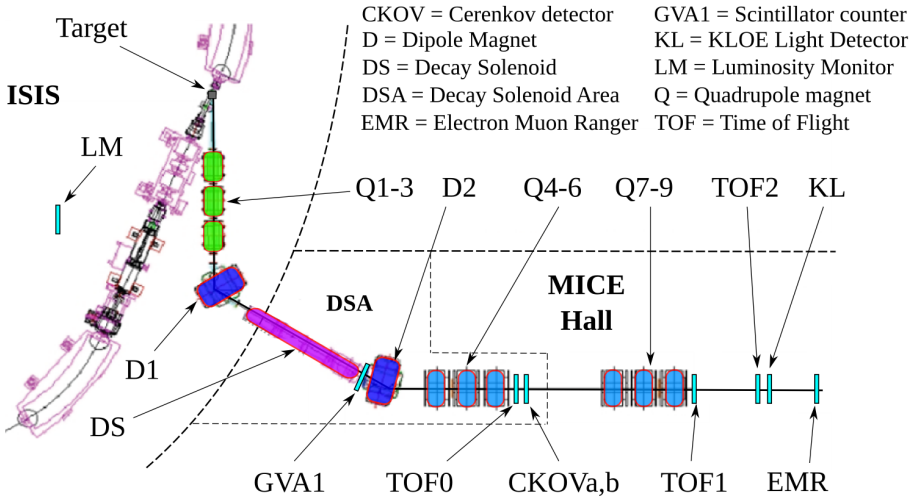

Figure 3.7: Schematic of the MICE Muon Beamline, showing the location of the target on ISIS, and the arrangement of the Quadropole, dipole, and decay solenoid magnets used to transport as many pions as possible to the cooling channel.

3.4.1 MICE Target design

Due to the parasitic nature of MICE, it was necessary to design a novel target that would dip into the ISIS beam, without creating an obstruction to the beam that would result in excessive beam losses in the ISIS beam. Multiple passes through the target, and if the beam is low energy, result in worse beam losses. Therefore the target must only be present in the beam for the protons with peak energy. ISIS accelerates protons from 70 MeV at injection up to 800 MeV at extraction, after which the next injection of protons occurs after a 10ms delay. This means there is a fairly narrow window in which the target has to operate. The MICE target is composed of a hollow Titanium cylinder of 3mm outer radius and 2.3mm inner radius, and "dips" into the proton beam during the last 2ms before beam extraction, shown by the beamloss graph in figure 3.8. A schematic of the target is found in figure 3.9. As the target must be outside of the ISIS beam envelope before the next injection, the target has to be capable of acceleration to the order of 90g, or 900ms^{-2}.

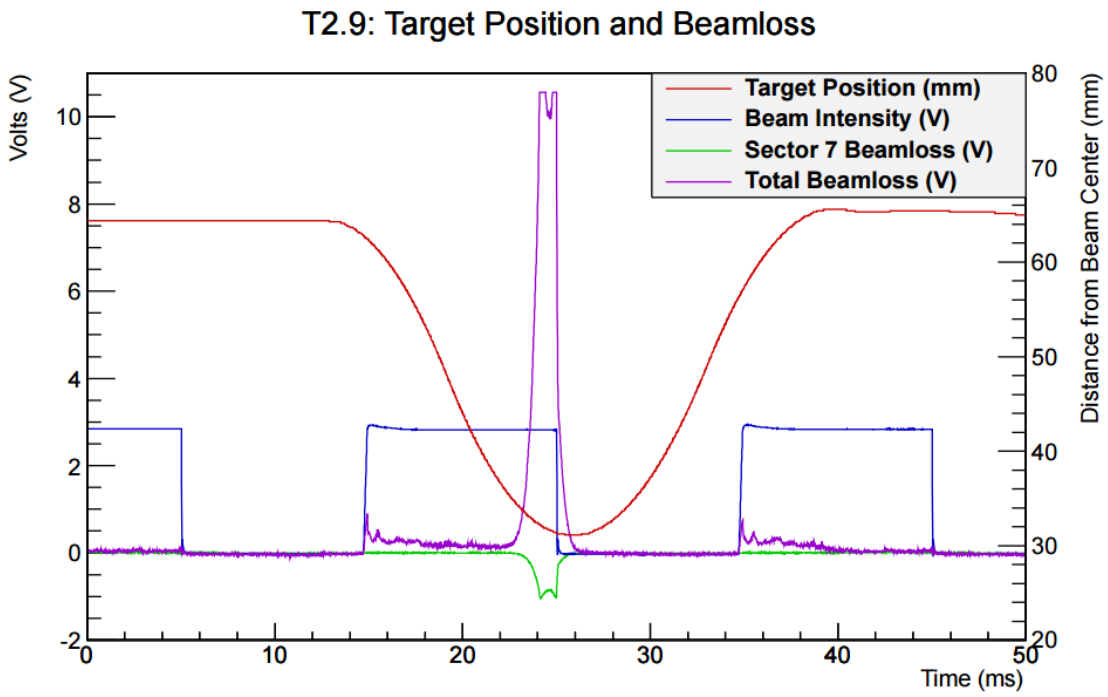

Figure 3.8: ISIS signals showing the beam intensity, total beamloss and summed beamloss from sector 7 (directly after the target) for the period that the MICE target is dipped. In this instance the sector 7 beamloss is shown as a negative signal [4].

The target drive consists of a brushless DC permanent magnet linear motor [5]. Actuation is achieved when the magnets in the target interact with the coils located within the stator. The Stator itself consists of 24 flat coils of copper wire around a steel tube, and water cooling, all mounted within an aluminium outer cylinder. This composition allows the target to meet the specifications.

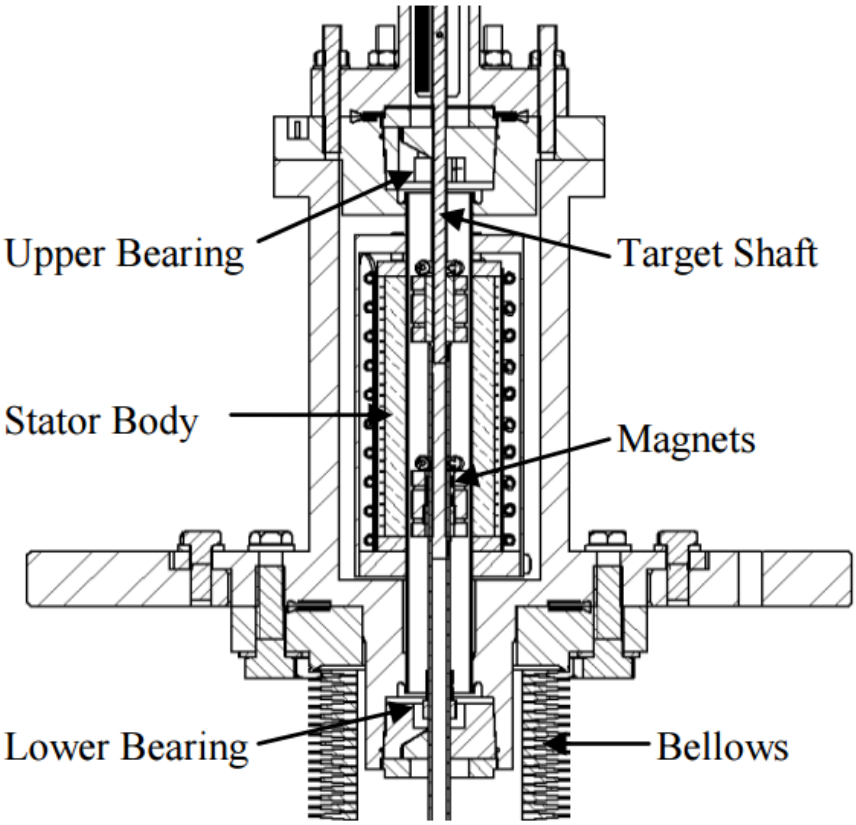

Figure 3.9: Schematic of the target. Actuation is achieved through the stator coils and magnets.[5]

3.5 Absorbers

An important part of ionisation cooling is the absorber material, which reduces the total momenta of particles in the beam through ionisation energy loss. The absorber is required to have a low Z value, to minimise the occurrences of multiple scattering events, which increase a particles transverse momentum and has the result of increasing the emittance (also known as heating). This is further discussed in chapter 4. MICE has elected to use Liquid Hydrogen (LH2) as its primary absorber. It has a high minimum dE/dx energy loss rate of 4.032 MeV cm^2/g [16], but also has a low density of 70kg/m^3 at 20K.

A schematic of the absorber module is shown in figure 3.10. The vessel that stores the LH2 has a volume of 23 litres and is 350mm long. There are aluminium windows either end of the cylinder with width less than 200μm, that are curved slightly to help withstand higher pressure whilst being thinner to minimise scattering. If necessary, the entire module can be replaced, so that other materials can be tested in the MICE beam. It is intended that MICE will also use a disk of Lithium Hydride of thickness 65mm (shown in figure 3.11), and a wedge-shaped absorber also of LiH [7]. LiH provides slightly worse cooling performance than LH2, due to its lower minimum energy loss (estimated around

1.92MeV cm^2/g), and increased density of $79.62 kg/m^3$ meaning particles have to travel through more material resulting in an increase of scattering events. However, LiH offers practical advantages over the volatile LH2 system, which has proved to be temperamental, and the first data collected in Step IV of MICE will be with the Lithium Hydride absorber.

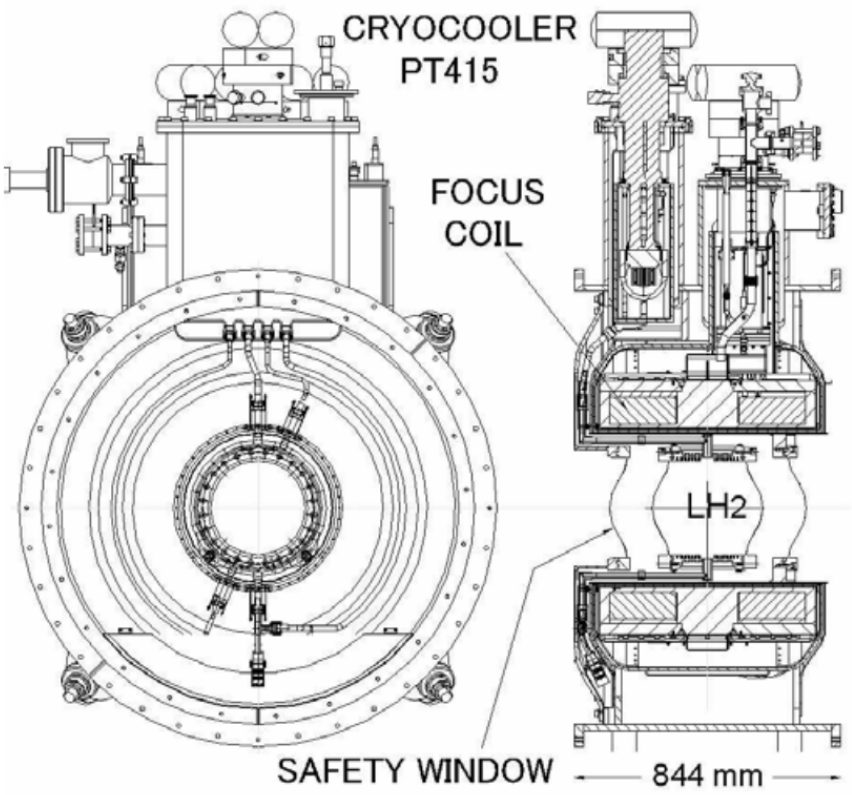

Figure 3.10: AFC module with LH2 absorber. [6]

Figure 3.11: The Lithium Hydride disk absorber. Radius 225mm, thickness 65mm. [7]

3.6 RF Cavities

The RF cavities will be added to the MICE cooling channel in the final stage after step IV. Their purpose is to re-accelerate the muons along the longitudinal direction, in order to replace the energy loss in the cooling process. MICE has eight RF cavities for this purpose, that in the demonstration setup will most likely be positioned either side of the absorber. An RF station is made up of four conductive copper cavities, each 41cm long and 61cm radius and arranged as shown in figure 3.12. The beam enters and exits the cavity through beryllium windows [50]. This means that the RF cavity can act as a closed system, which improves its electromagnetic properties [51], and the use of a low density material such as beryllium means that the muons should be almost unaffected. The cavities can operate at 201 MHz, and are driven by a 2-MW amplifier system to allow for a gradient of 8MV per cavity.

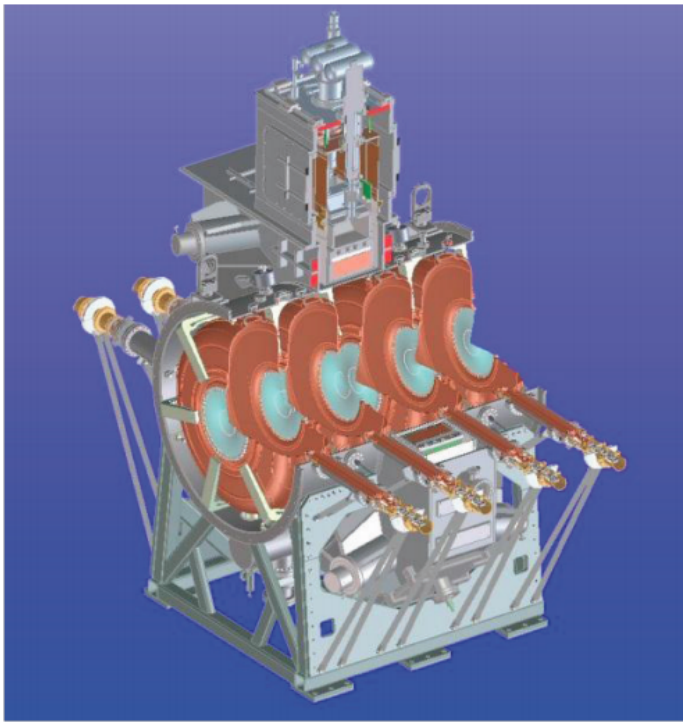

Figure 3.12: Partial cross section of one of the MICE RF modules, showing the cavities, couplers and BE windows. [8]

3.7 Detectors

3.7.1 Luminosity Monitor

A Luminosity Monitor is located inside the ISIS vault at a position indicated in figure 3.6. It is mounted 10m from the target in a position at an angle such that if a line is drawn from the monitor to the target, the start of the MICE beamline is reflected along the ISIS axis. This allows the Luminosity Monitor to provide a measure of flux of pions generated by the target.

Figure 3.13 shows a schematic of the Luminosity Monitor. Two sets of scintillators are coupled to two pairs of photomultiplier tubes. One scintillator is shielded by a 150mm piece of polyethylene, which suppresses signals of protons below 500MeV. The shielded scintillator has a cross-section of 20 x 20 mm^2, and the unshielded 30 x 30 mm^2 [9].

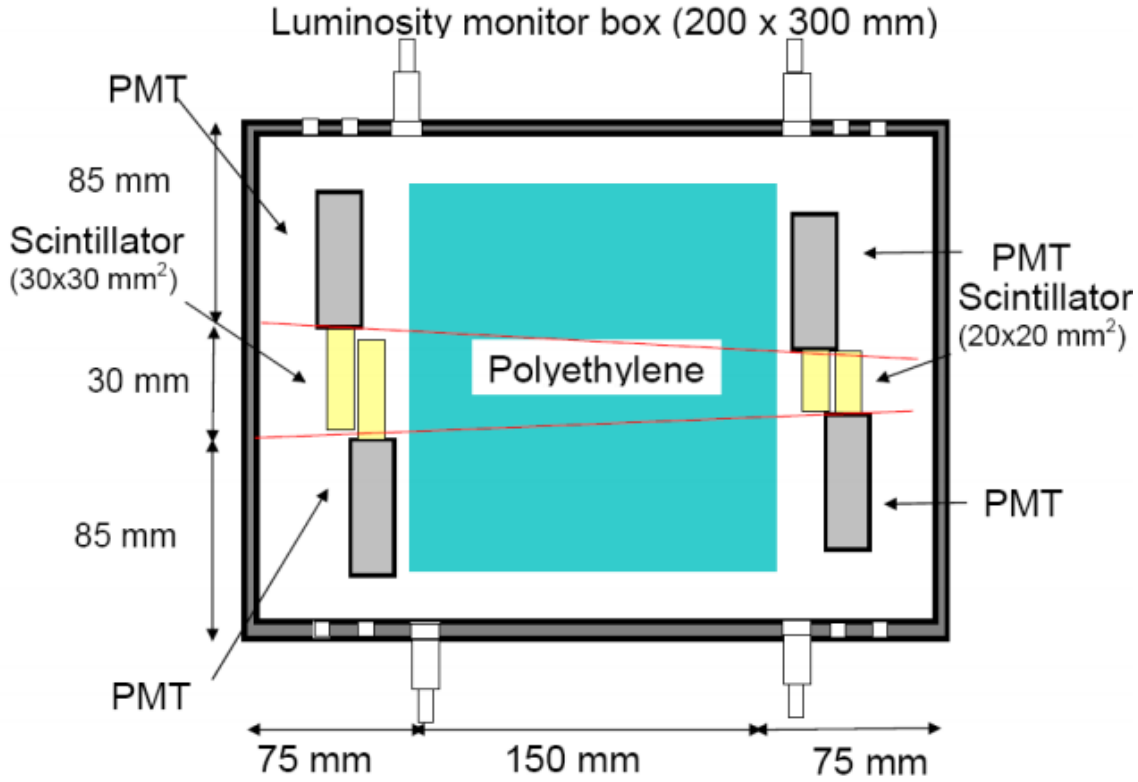

Figure 3.13: Schematic of the Luminosity Monitor [9]

3.7.2 Time of Flight Detector

Along the MICE beamline there are three time-of-flight detectors, TOF0, TOF1 and TOF2, which are used for PID measurements by utilising the fact that particles of the same momenta take different times to travel between stations. The positions of TOF0 and

TOF1 are shown on the beamline diagram in figure 6.7, and TOF2 is located after the trackers before the KL detector. Each TOF station is composed of 2 layers of rectangular scintillator slabs, arranged orthogonally to provide an x-y geometry. Each slab is read out by 2 PMT attached either end, as shown in the schematic in figure 3.14. TOF0, TOF1 and TOF2 have active areas of 40 x 40 cm^2, 42 x 42 cm^2 and 60 x 60 cm^2 respectively [52].

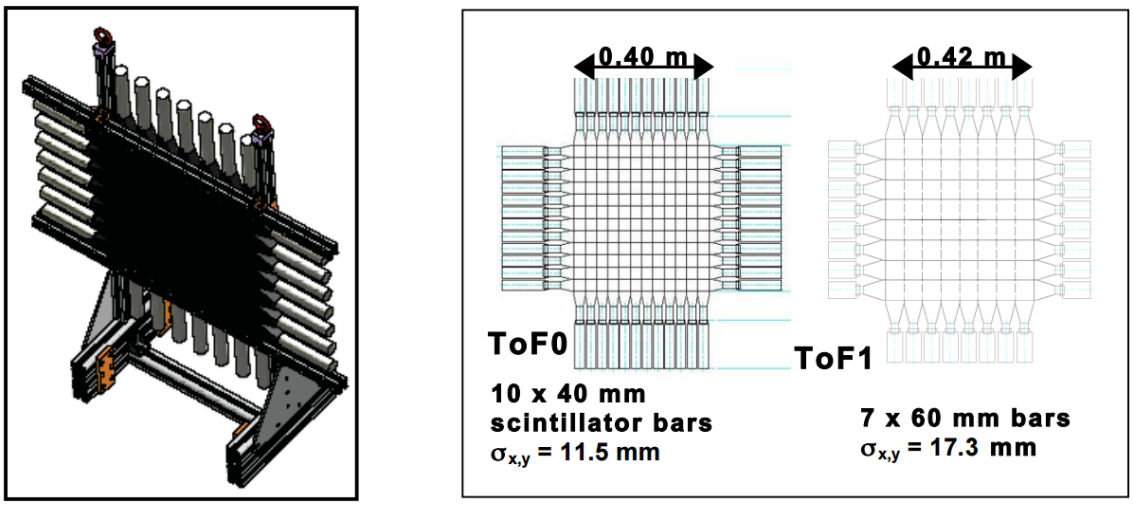

Figure 3.14: TOF detector design. 3D view on left and schematic structure of scintillator and PMT on right. TOF2 has the same number of slabs as TOF0 but with a greater effective area. [10]

TOF0 and TOF2 have measured time resolution of about 50ps each. TOF1 has slightly worse resolution of about 60ps due to using slightly lower quality PMTs, but remains within the design spec [11]. An example of the time of flight distribution seen from analysis of the TOF0-1 detectors is shown in figure 3.15. The TOF detectors have some additional uses when running MICE. TOF2 is also used to make a measure of the number of particles reaching the end of the cooling channel. TOF0 is used as a trigger for the DAQ system during data taking. It is also possible to make a measurement of the beam profile (see figure 3.16), which was used during Step I running to characterise the MICE beam [18].

3.7.3 Cherenkov Detector

From figure 3.15, one can tell that whilst the majority of pions and muons can be identified from each other in the MICE beam, there exists a region where TOF0/1 alone are not sufficient. Discrimination between muons and pions is particularly difficult for momenta >200 MeV. Therefore MICE also has two aero gel Cherenkov counters, which allow greater discrimination to take place. There is no single material that would radiate

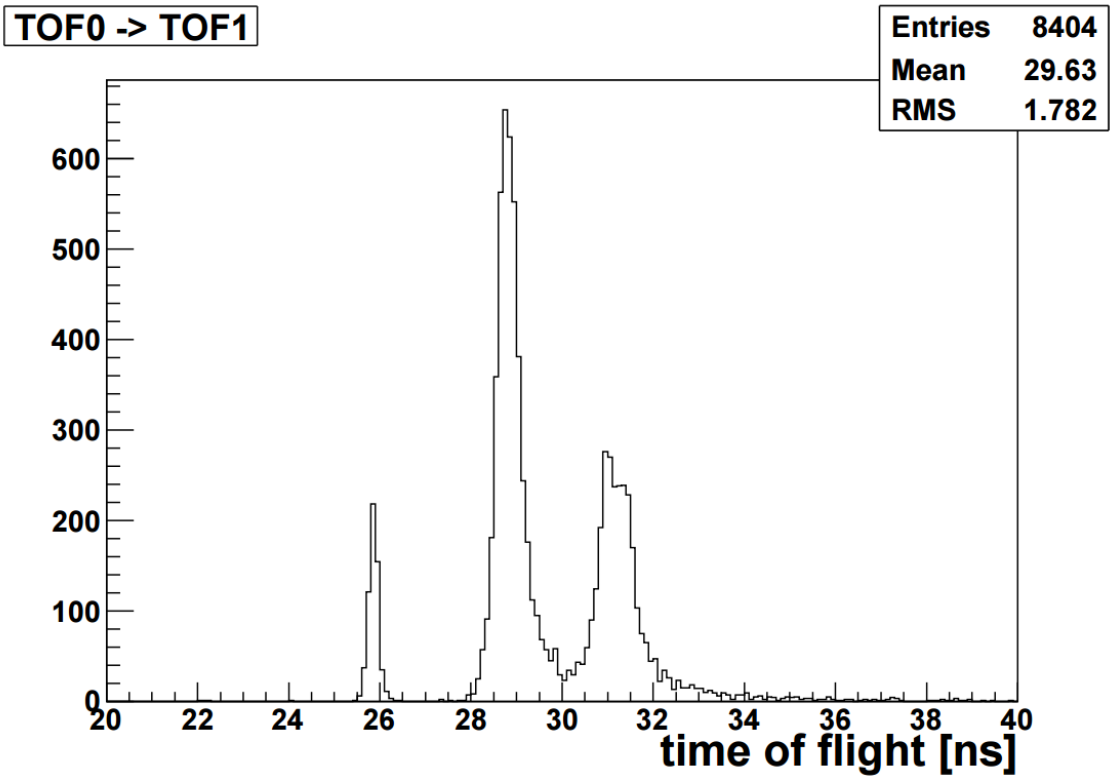

Figure 3.15: Time of flight between TOF0 and TOF1 for an electron beam. The left peak indicates population of electrons, the center peak muons and the rightmost peak pions. [11]

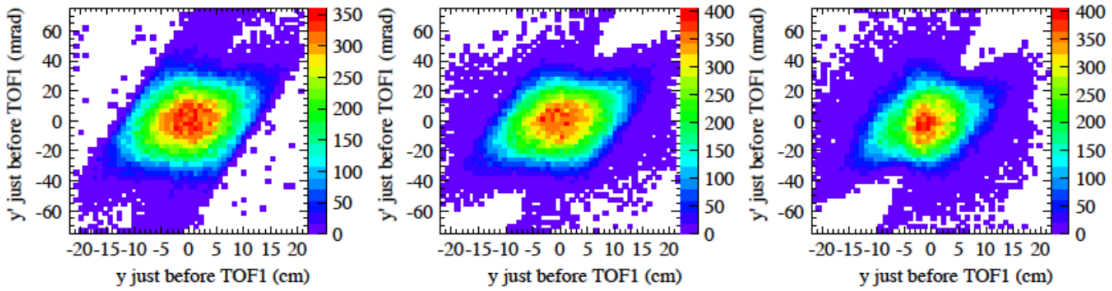

Figure 3.16: Vertical trace space emittance measurements using TOF1. True values from MC data on left, reconstructed MC in the center, and reconstructed experimental data on right. Taken from [10]

Cherenkov light for muon, but not pions, over the entire operating momentum range of MICE, so therefore two forms of aerogel were commissioned.

Both CKOV detectors were constructed from 15mm steel places, with 4 PMT's positioned one on each lateral face. CKOV1 had a refractive index of 1.07, and CKOV2 of 1.12. Figure 3.17 demonstrates the signals produced in each CKOV detector for a range of particles and momenta. For momentum region 1, CKOV 2 produces a signal for muon. In momentum region 2 both CKOV give a signal.

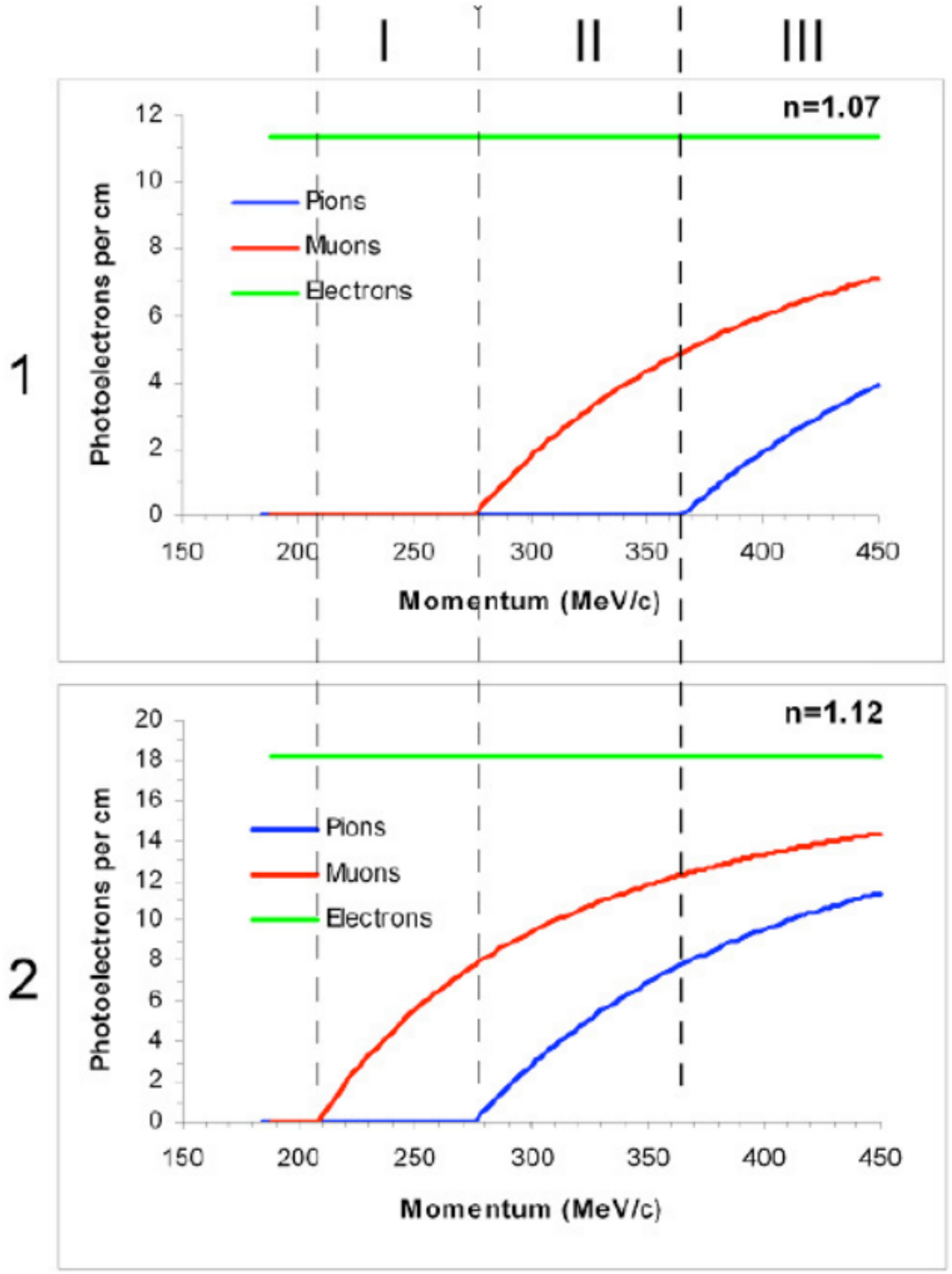

Figure 3.17: Response of the two CKOV detectors to muons, pions and electrons at a range of momenta. In momentum region I only muons produce a response from CKOV2. In region II, muons produce a signal in both detectors. Region III is above the region of interest to MICE.[42]

3.7.4 Trackers

In MICE there are two trackers which are situated either side of the AFC in Step IV, and will be either side of the cooling channel in the final demonstration setup. Each tracker is made up of 5 stations of scintillating fibers, and have a small diameter of around

350 μm to minimise any multiple scattering effects [53]. A photo of the tracker station layout is shown in figure 3.18. The fibres are read out by Visible Light Photon Counters (VLPCs), which have a high quantum efficiency. Each of the 5 stations inside each tracker is identical, and consists of 3 doublet layers of scintillating fibre, with each layer arranged orientated 120° to the other two as shown in figure 3.19. The arrangement of the planes allows for full 3D coordinate reconstruction of a particle travelling through the detector [54], whilst the doublet layering means that there is no deadspace where a particle could slip through the detector unnoticed. Each tracker is surrounded by a solenoid magnet, designed to provide a uniform 4T field across the whole of the tracker, which produces curved tracks thus allowing the momentum to be measured [55]. Recent issues with the commissioning of the downstream solenoid have led to the maximum possible field being limited in the upstream solenoid to 3T. The downstream solenoid is unable to run current through the two matching coils closest to the absorber, and hence only has a partial field coverage. The resolution of this measurement is very important in the Energy loss analysis and is talked about in greater detail later.

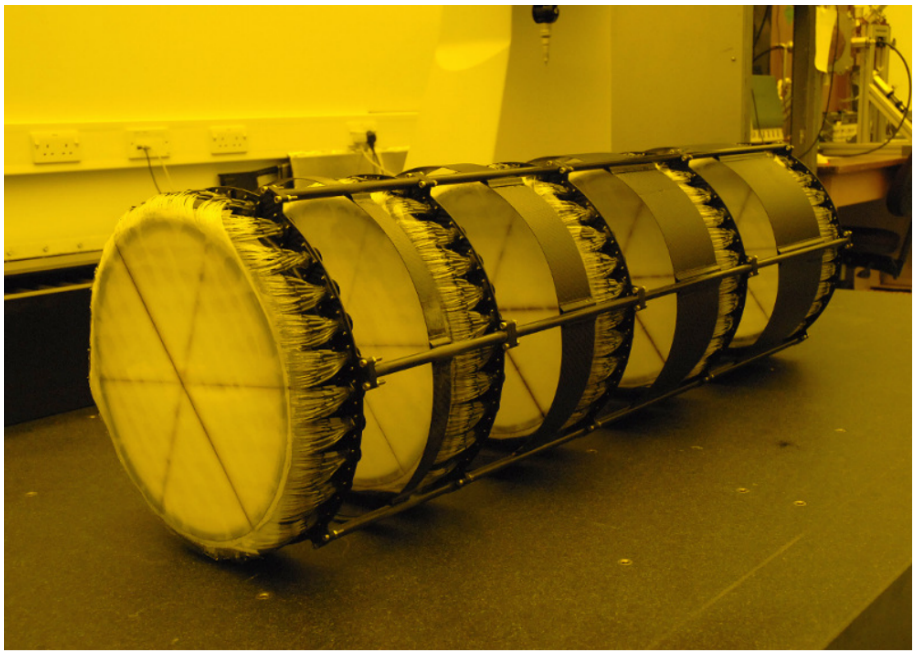

Figure 3.18: Photograph of the 5 tracker stations. The stations are held by a carbon fibre frame. Special lighting is needed to protect the fibres from damage, hence the orange glow in the picture. [53]

3.7.5 KL

The KL, along with the EMR, is used to aid in distinguishing muons from decay-electrons in the MICE beam. It closely follows the design of the calorimeter used in the KLOE

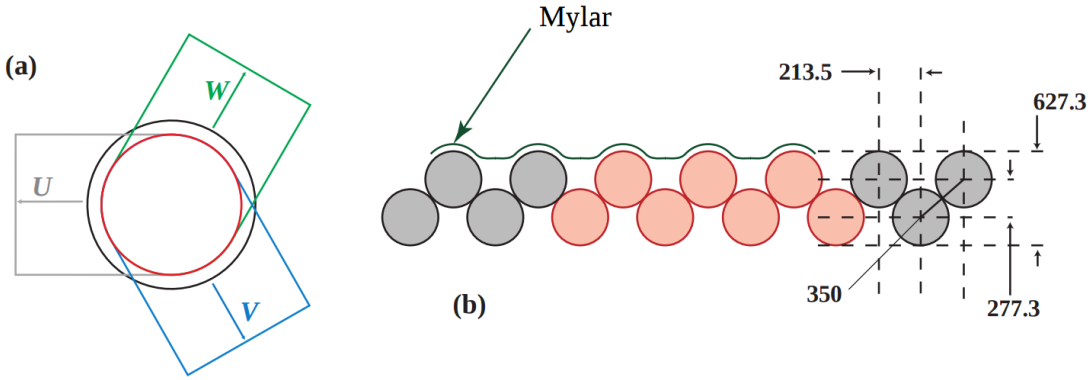

Figure 3.19: (a) Arrangement of the 3 tracker planes inside a single tracker station. The outer circle shows the solenoid bore whilst the inner circle indicates the active tracking region. The regions marked U, V and W indicate the directions taken by the 3 planes. (b) The arrangement of the fibres in a doublet layer. Spacing and pitch of the fibres is given on the right-hand side of the figure in μm. [54]

experiment [56]. It consists of 3mm grooved lead plates inlaid with 1mm scintillating fibres, and has an active cross section of 120 x 120 cm^2. It is installed in the MICE beam directly prior to the EMR.

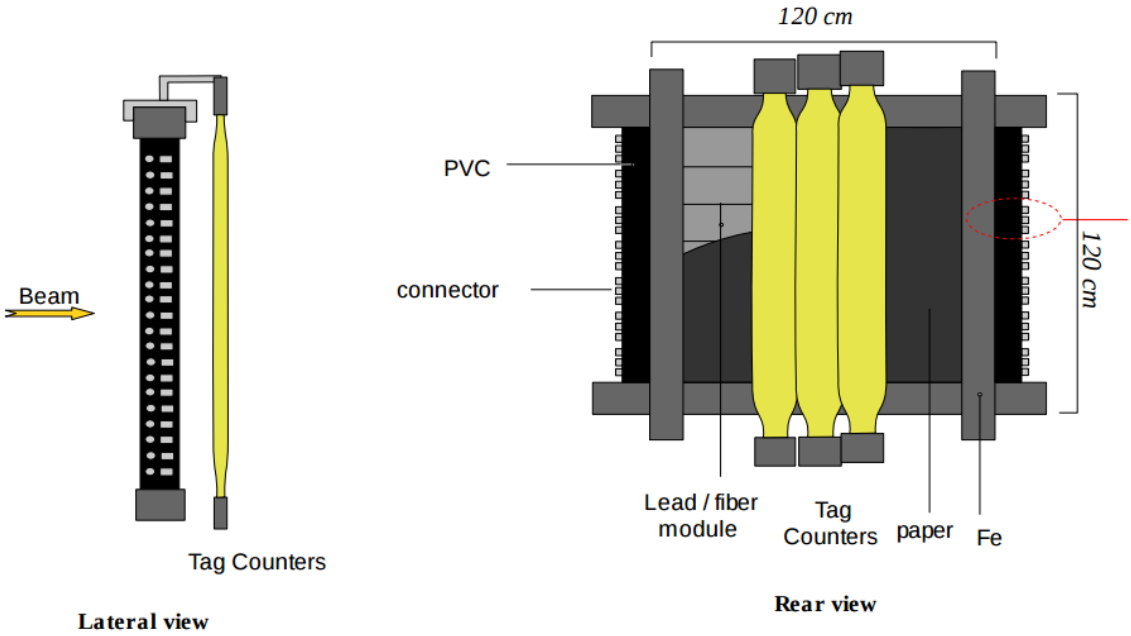

Figure 3.20: Schematic of the KL detector, from the side and the rear. [12]

3.7.6 Electron Muon Ranger

The EMR is a totally active scintillator detector which is situated at the end of the MICE beam. It works alongside the KL to help identify decay electrons in the MICE beam.

Muons will deposit most of their energy at the point of decay within the detector, whereas Electrons will deposit energy uniformly across many bars. The EMR should be able to record a full energy spectrum of each track for evaluation, and particles can be identified through comparison of the spectra. This information will compliment the PID information already obtained through the TOF detectors, whilst determining if Muon-Electron decay has taken place within the cooling channel. Muon decay occurring within the cooling channel will result in extra contamination of the final result, as the decayed electron will have a momentum component transverse to the momentum of the initial muon. Therefore the EMR has an important role to play in analyses.

The EMR consists of 48 planes (59 bars per plane) of triangular scintillator bars, with the bars in each alternating plane arranged orthogonally to its neighbours to provide an x-y tracking geometry. Each plane has dimensions 1m x 1m x 1.7cm. Each bar has an optical wavelength-shifting fiber running through it, which on one side of each plane are bunched together and read-out by a single PMT in order to obtain an energy reading for the whole plane. On the other side of the plane, a 64-channel PMT takes energy measurements of each individual bar in the plane.

The EMR was commissioned in the MICE hall in October 2013, and it was demonstrated that the EMR by itself can identify electrons produced from muons decaying in the cooling channel with 98.6% efficiency [13], through techniques such as comparing the different plane density of particles (muons have a much higher penetration, and therefore plane density, than electrons.) The EMR can also make a momentum measurement, with a resolution of around $\sim$ 10 MeV/c for particles stopping midrange, and down to 3 MeV/c for large range particles, shown in detail in figure 3.22.

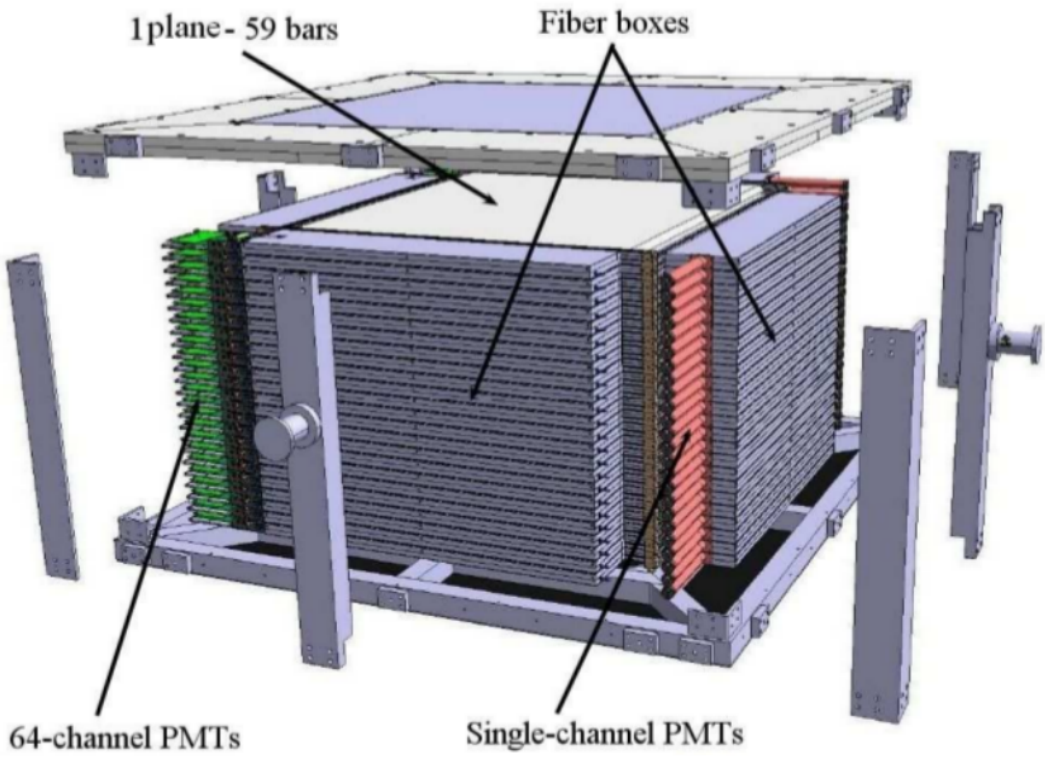

Figure 3.21: Schematic of the EMR Detector, orientated on it's side. [13]

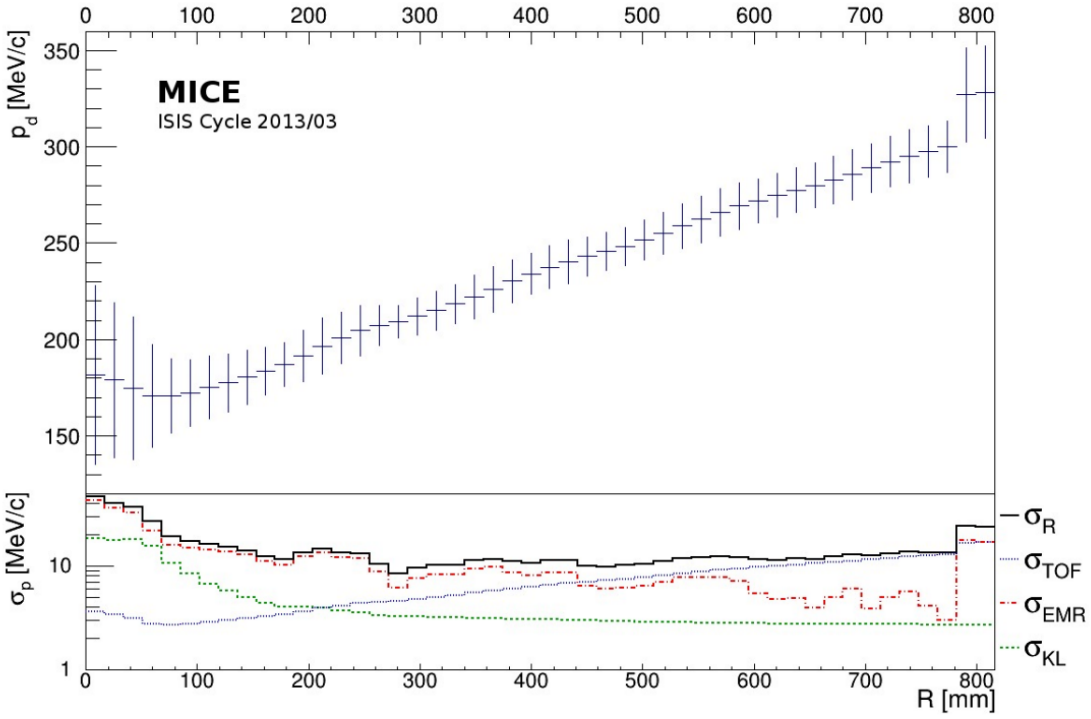

Figure 3.22: Downstream momentum as a function of range (R) travelled in the EMR. One bin is one plane and it's error is representative of the RMS of the momentum distribution within the bin. [13]

Chapter 4

Energy Loss - Physical Processes

As discussed in chapter 3, Energy Loss in the absorber is one of the key processes involved in ionisation cooling. Although predictions exist to calculate the expected energy loss in form of the Bethe formula [16], direct measurement of energy loss has not been carried out for any material at 200MeV, including Lithium Hydride which will be the primary absorber investigated in this thesis. In this section the physical energy loss processes will be reviewed, alongside a look at the Bethe equation with a model of how the Bethe equation predicts muon energy loss in Lithium Hydride over the MICE momentum range.

4.1 Ionisation

When a charged particle (such as a muon) passes through a material, interactions will take place between the muon and the atoms that make up the material. For muons, these interactions can classified into electronic processes, such as ionisation and scattering, and radiative processes such as bremsstrahlung and pair production. The mean energy loss as a function of distance, or the stopping power, can be expressed as [57]:

$$\frac{-dE}{dx} = a(E) + b(E)E \tag{4.1}$$

where E is the total energy, a(E) is the electronic stopping power and b(E) is the radiative stopping power. Note that for muons, radiative processes are negligible below the GeV energy scale, and therefore this term can be ignored in the context of MICE. Therefore the greatest contribution to energy loss will be in events where the muon interacts with

the electrons, continuously transferring energy through ionisation but leaving the trajectory of the muon relatively unchanged. Direct or hard collisions between the muon and the electrons or atomic nucleus have a small chance of occurring (however are important in the context of measurements). Such a collision with an electron will eject an electron from the atom.

Any interaction between the muon and the constituents of an atom will result in an amount of scattering on the muon. For electron scatters, the scatter will only depend on the proximity of the muon to the electron. However, if the muon scatters off the nucleus then the higher the charge of the nucleus, the greater magnitude the scatter will be. An optimal material to study energy losses will minimise these hard scatters, and therefore will have low Z, which will minimise the nuclei scatters. The second point to make is that the interaction between a muon and an electron has a dependence on the momenta of both particles.

4.2 Multiple Scattering

With any interaction between the incident muon, and an atom inside the absorber, there will be both energy loss and scattering. This is shown in figure 4.1, where an incident muon of energy E and momentum p interacts with an electron in an atom. The muon will lose kinetic energy in this process (expressed as v below), and also scatter from the electron at an angle θ. One can write this interaction by rearranging $E^2 = p^2 + m^2$ for the muon and electron.

$$(m_e + v)^2 - (\vec{p} - \vec{q})^2 = m_e^2 \tag{4.2}$$

$$(E - v)^2 - \vec{q}^2 = m_\mu^2 \tag{4.3}$$

and therefore

$$\vec{p}\vec{q} = p^2 - (E + m_e)v \tag{4.4}$$

then using the definition of the scalar product, this results in the expression

$$cos\theta = \frac{p^2 - (E + m_e)v}{|p||q|} \tag{4.5}$$

From equation 4.5, the mass term m_e could be replaced with the mass of any target object, such as the atomic nucleus, as the equation was constructed in the rest frame of the electron. Therefore, for a given scattering angle, the energy transferred to the target would be much greater in an electron interaction as opposed to a nucleus. However, for a given energy loss the muon will experience a greater scattering angle with a nucleus than with an electron.

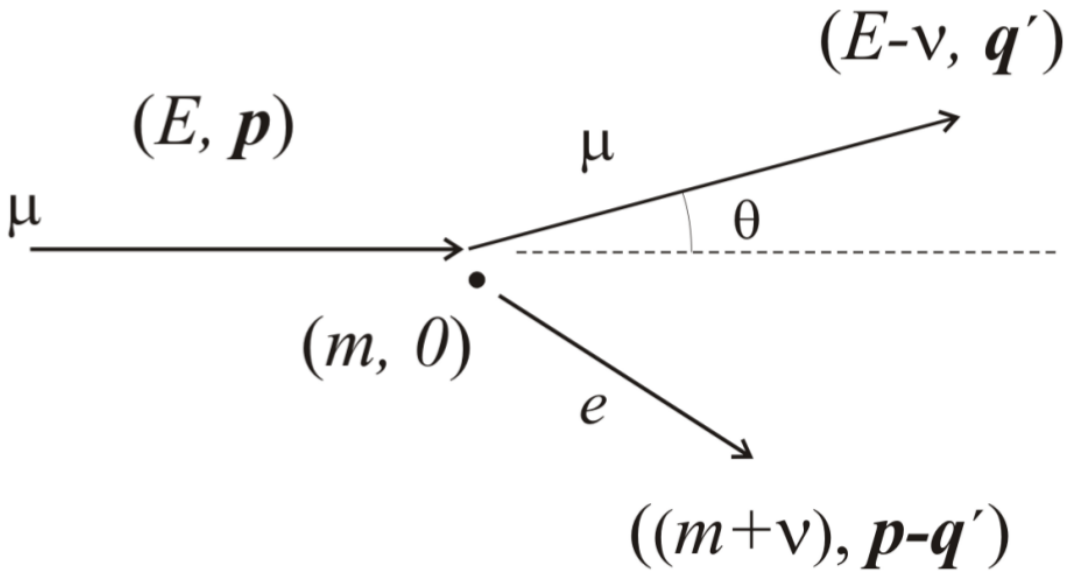

Figure 4.1: An incident muon scattering off an electron.

4.3 The Bethe formula

The Bethe formula [58] is used to describe the mean energy loss of charged particles as they travel a distance through a material through ionisation processes. The formula is given by:

$$-\left\langle \frac{dE}{dx} \right\rangle = Kz^2 \frac{Z}{A} \frac{1}{\beta^2} \left[\frac{1}{2} ln \frac{2m_e c^2 \beta^2 \gamma^2 T_{Max}}{I^2} - \beta^2 - \frac{C}{Z} \right] \tag{4.6}$$

Where:

- $\frac{K}{A}$ is a constant term that equals $0.307075 MeV g^{-1} cm^2$
- z is the charge of the incident particle
- Z is the atomic number of the absorber
- I is the Mean Ionisation Potential of the material

- T_{Max} is the maximum transferable kinetic energy
- $\frac{C}{Z}$ is a shell correction term for slow particles (energies less than 100MeV) [59]

The maximum transferable kinetic energy term can be defined as:

$$T^{Max} = \frac{2m_e c^2 \beta^2 \gamma^2}{1 + 2\gamma m_e/m_\mu + (m_e/m_\mu)^2} \tag{4.7}$$

where m_μ and m_e are the masses of the muon and electron respectively, and γ and β relate to the relativistic quantities of the incident muon.

There are a few things to note regarding the Bethe equation. The energy loss is independent of the mass of the incident particle, and only dependant on its energy. So for example, a proton and a muon should have similar energy loss curves for the same absorber. The minimum of the equation lies around the point where β = 0.96, and the relationship between β and the energy loss for various values of β is discussed further in the next section. Finally, the z^2 term means that there is a strong dependence on the charge of the incident particle, meaning highly charged ions will suffer from higher energy losses.

Regarding the material of the absorber, the Z/A term contributed from the material of the absorber is similar for many materials, meaning dE/dx is relatively independent of material.

4.4 Energy loss dependence on Material

Figure 4.2 shows the calculated energy loss values of protons travelling through various materials. Generally, as expected the minimum energy loss occurs around the point where $\beta = 0.96$. The range of minimum energy losses for materials (excluding Hydrogen) lies between 1-1.7MeV /(g/cm^2), demonstrating the weak dependence on material. The minimum energy loss (or minimum ionisation) for a range of materials with Z between 1 and 100 are plotted in figure 4.3, and it can be seen that the energy loss is generally consistent within a range of a few MeV.

The mean ionisation energy of a material is a quantity used in the Bethe equation, and is a measure of the average energy required to ionise a material. This is greater than the minimum ionising energy of the material.

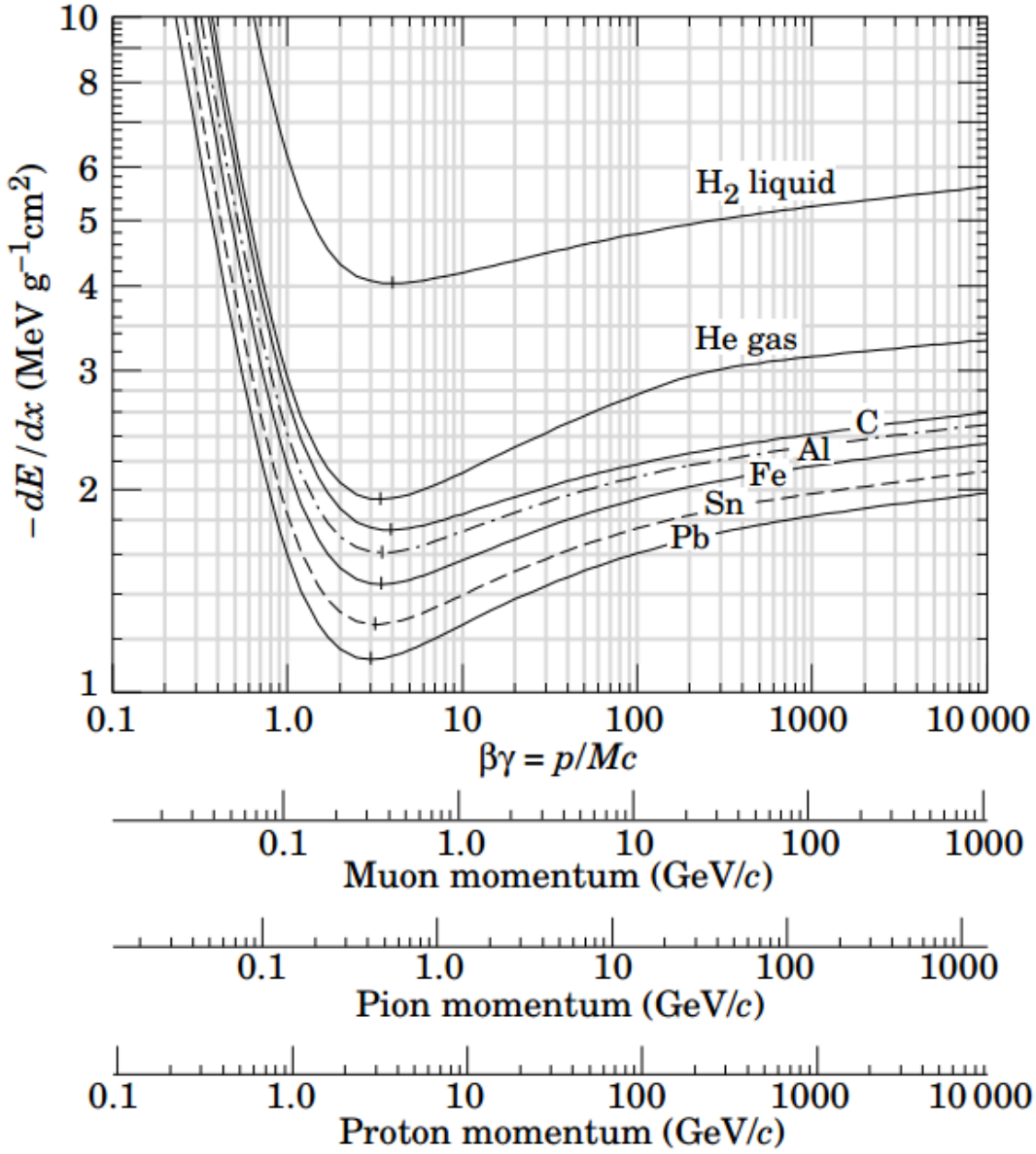

Figure 4.2: Mean energy loss rate in various materials from ionisation [14]. Note that the mimimum energy loss for each function lies around $\beta\gamma = 3 - 3.5$, and the difference in minimum energy losses is also small.

4.5 Momentum Effect on Energy Loss

Figure 4.5 shows the mean stopping power of muons in Copper for a range of momenta between 0.1 MeV/c and 100 TeV/c, where some data is predicted by the Bethe equation and some is from experimental measurements.

For low momenta (less than 0.02MeV/c), the energy loss directly correlates to β. As the particle momentum increases to over 0.1MeV/c, the Bethe equation describes the energy loss well up to high muon momenta of around 1TeV. After this point radiative energy loss

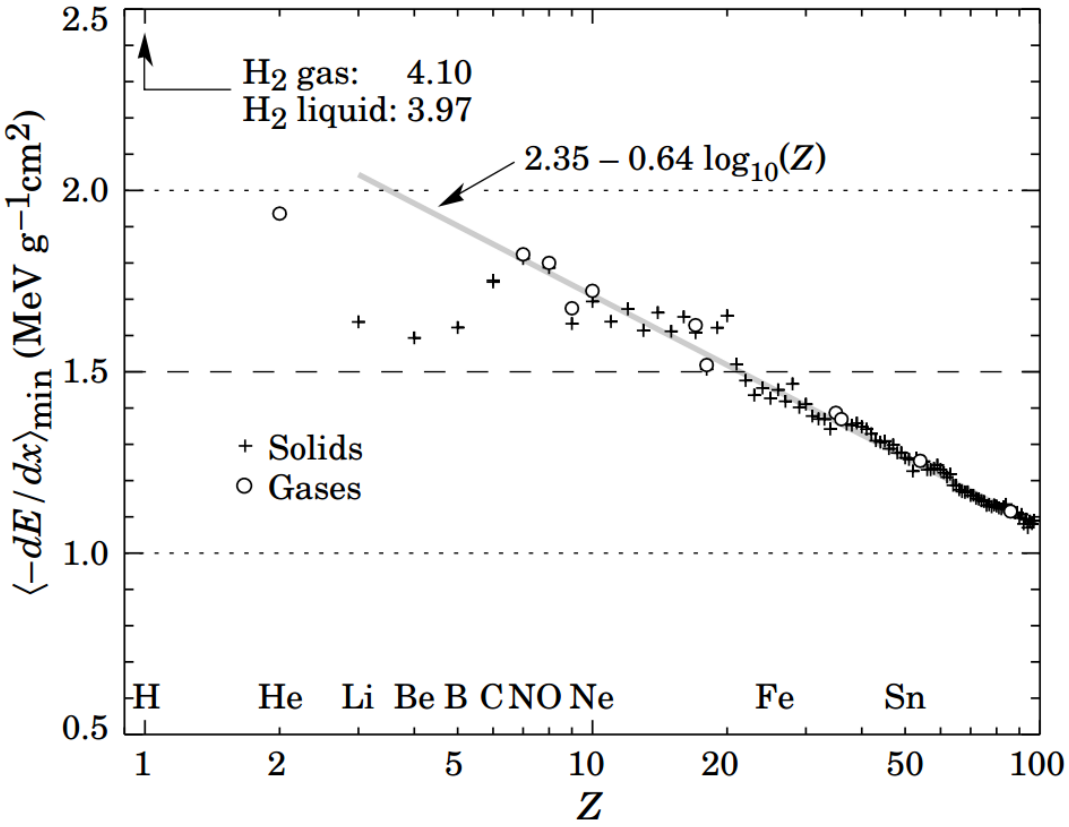

Figure 4.3: Minimum Energy loss as a function of Z. The straight line is plotted for points where Z $>$ 6.

processes begin to take over.

4.6 Fluctuations in Energy Loss

The Bethe equation gives the average energy loss for an incident particle per unit thickness of an absorber. However, fluctuations around the mean value have a significant effect on the distribution, depending on the thickness of the absorber. For a thin absorber, there are fewer particle interactions, resulting in a higher probability that particles lose less energy, with fewer particles suffering high energy losses. This creates a Landau distribution, with a peak at the most probable energy loss just below the mean energy loss, which itself is skewed to a high value as a result of a lower proportion of much higher energy losses tending towards T_{Max} [60].

A thicker absorber has many collisions, and therefore it is more likely that each particle is affected in the same way as a result of the central limit theorem. Therefore, in these instances the peak of the distribution will be gaussian, with nearly no difference between the average energy loss and the most probable energy loss. It is still possible that there

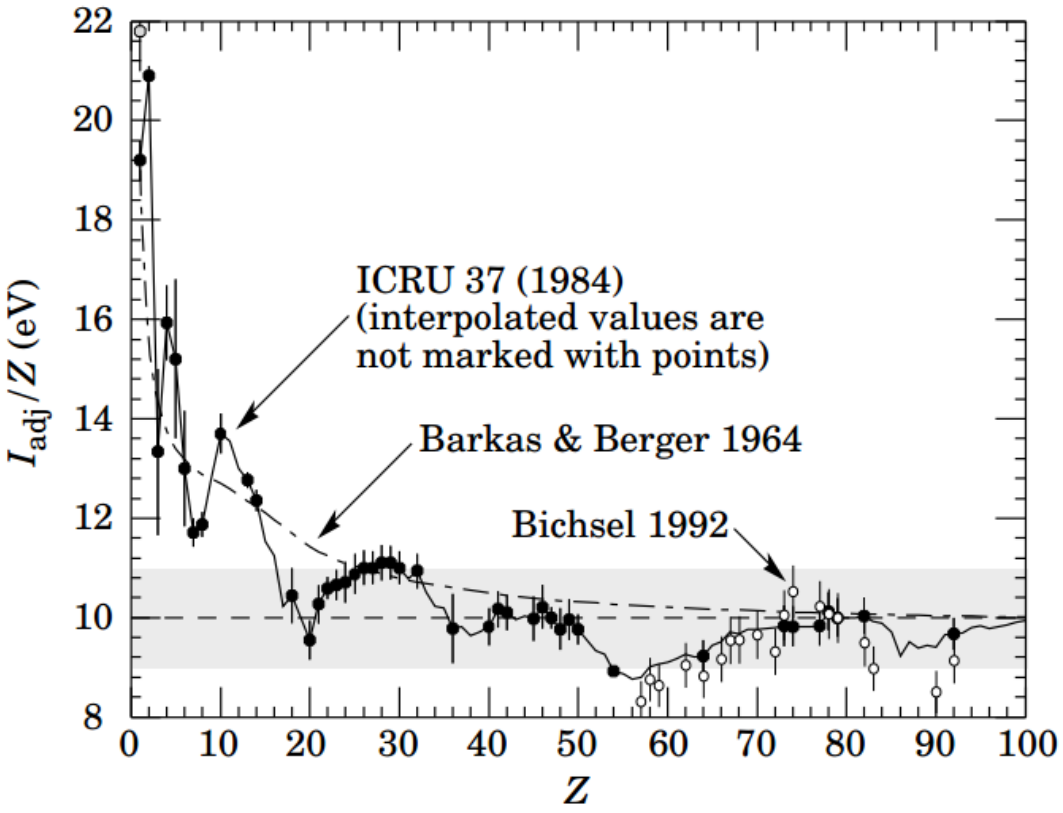

Figure 4.4: Mean excitation energies taken from the ICRU 37 report [15], and reviewed in the PDG [14]. Values based on experiment have error flags. The open circles show more recent determinations by Bichsel, and the dotted curve indicates the association $I = 16Z^{0.9}eV$.

will be a tail to high energies, as a result of hard scattering, which skews the average energy loss measured. However in this instance if the peak can be shown to be a gaussian distribution, then the peak may represent the best estimate of average energy loss.

The most probable energy loss for an absorber can be calculated using the Landau equation [61]:

$$\Delta_p = \Xi \left[ln\frac{2mc^2\beta^2\gamma^2}{I^2} + ln\frac{\Xi}{I} + j - \beta^2 \right] \tag{4.8}$$

where

$$\Xi = \frac{K}{2}\left\langle \frac{Z}{A} \right\rangle \frac{x}{\beta^2} \tag{4.9}$$

For a detector with thickness z in g cm^{-1}. j = 0.200 [61]. This Landau equation is also expressed with a correction for the density of the material, but as that only applies for high energies it hasn't been discussed here. One main difference is that whilst the Bethe equation is relatively independent of the thickness of the material, the most probably energy loss scales as $aln(x)+b$. Figure 4.6 shows the effect of the thickness of the absorber

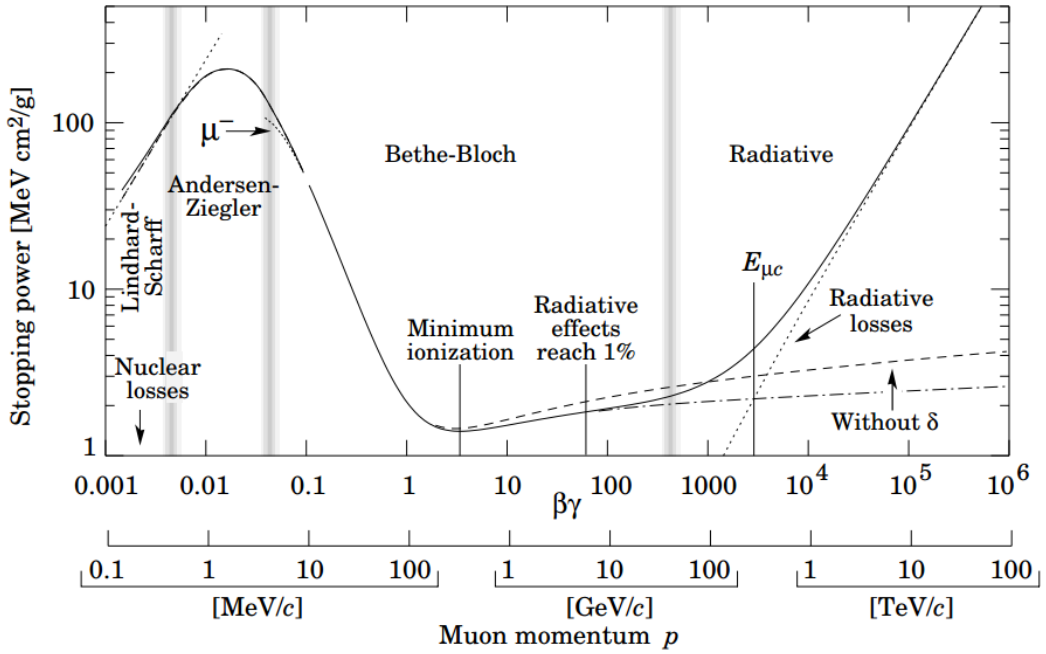

Figure 4.5: Stopping power (=$\langle -dE/dx \rangle$) for muons in copper as a function of momentum taken from the particle data group [16]. Solid curves indicate the total stopping power. Data below the break at around p = 0.5 MeV/c are scaled by the appropriate mass ratios. Vertical bands indicate boundaries between different theoretical approximations or dominant physical processes.

on the most probable energy loss at the minimum ionising point of Silicon.

Because the most probable energy loss is seen in an energy loss distribution as the peak of the landau curve, it is much easier to measure this value then the mean energy loss predicted by the Bethe equation. This is particularly true for small sample sizes, where only a few rare occurrences of high energy loss can extend the tail of the distribution, and this skew the mean and make it very sensitive to cuts.

4.7 Energy Loss for 200MeV Muons in Lithium Hydride.

In the MICE cooling channel, a 65mm thick Lithium Hydride absorber will be used to provide ionisation cooling, and it is possible to use the Bethe and Landau equations to make a calculation of the first estimate for the energy losses in the absorber. The mean energy loss caused unto the muon beam by the absorber can be modelled using the Bethe equation, and the most probable energy loss will also be calculated using equation 4.8.

Lithium Hydride is a molecule, and therefore its effective atomic number must be used in

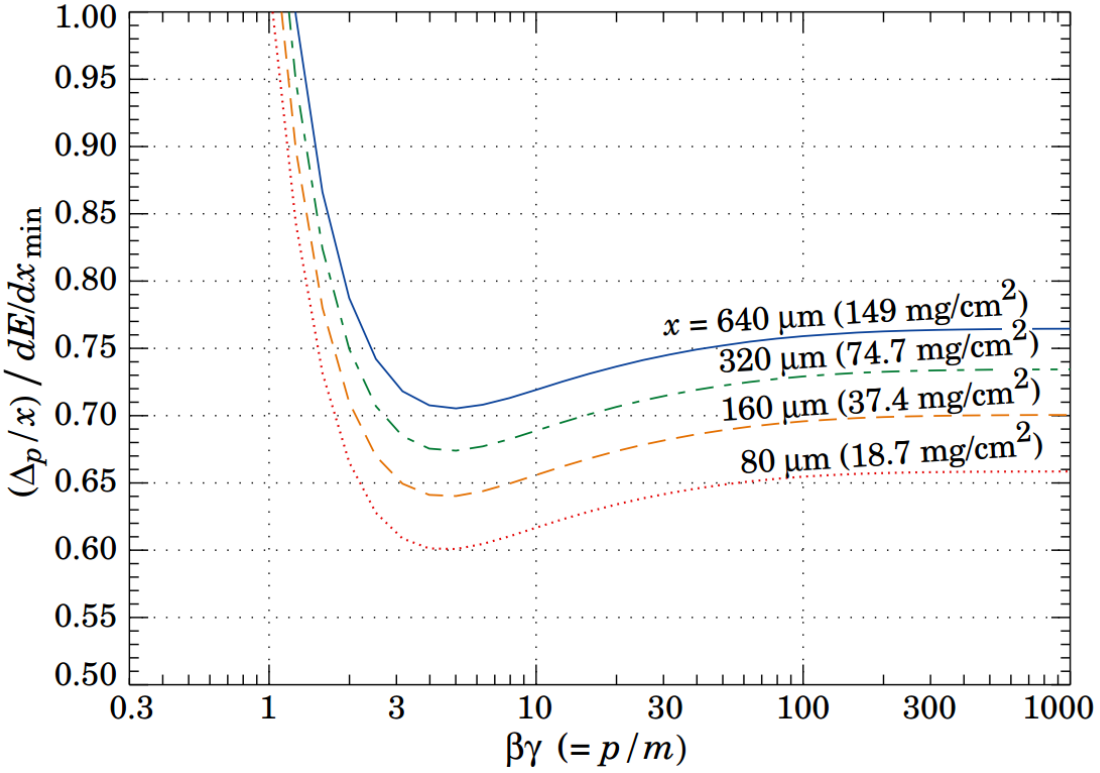

Figure 4.6: Most probable energy (Δ_P/x for particles in Silicon around the minimum ionising point.[14]

the Bethe equation. This was obtained using equation 4.10

$$\sqrt[2.94]{f_1 x(Z_1)^{2.94} + f_2 x(Z_2)^{2.94} + \ldots} \tag{4.10}$$

where f_n is the fraction of electrons associate with each element in the molecule, and Z_n is the atomic number of each element. This gives $Z_{eff} = 2.7325$.

In order to use the Bethe equation to estimate the mean energy loss for Lithium Hydride, the Bethe equation was encoded into a program written in python. The first stage of the program was to input the initial energy of the muon, and then the energy loss of the muon after it has travelled through 0.1mm of Lithium Hydride was calculated. Then the new energy is used to calculate the energy loss in the next 0.1mm, and this continues until the muon exits the Lithium Hydride.

Figure 4.7 shows the result of the Bethe calculation on 66mm of Lithium Hydride, for a range of muon energies between 100MeV and 1000 MeV. The predicted minimum ionising point of Lithium Hydride can be seen at around 300 MeV, which is in line with other materials as looked at in figure 4.2.

Figure 4.8 shows the results of the same calculation, but zoomed in on the range of muon energies that can be covered by the MICE experiment. There is only expected to be an approximate 5% difference in energy loss across the range of muon energies.

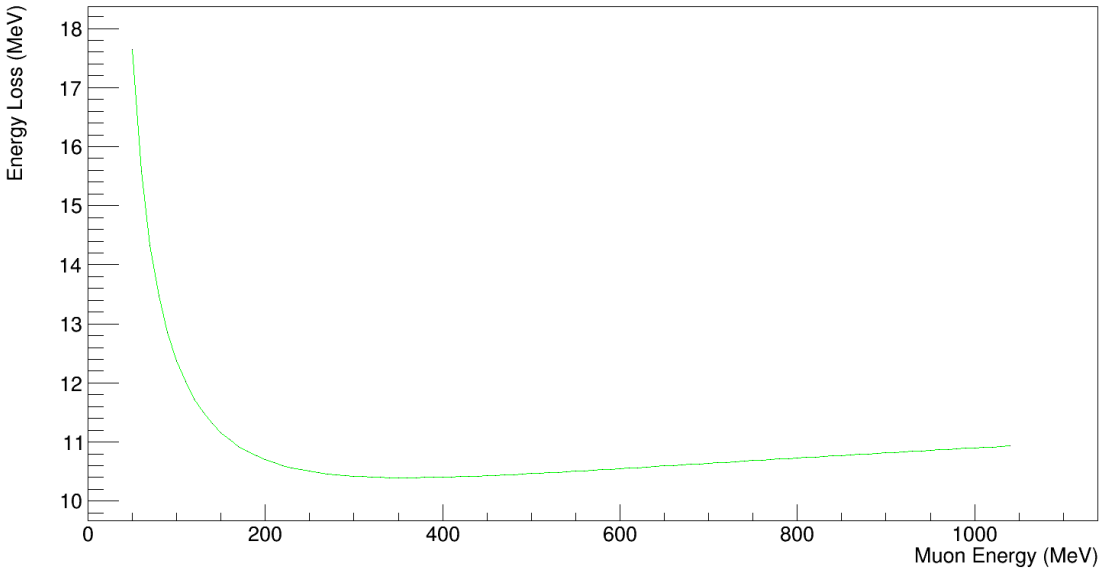

Figure 4.7: Mean energy loss of muons in 65mm of Lithium Hydride calculated from the Bethe equation. Using an effective molecular mass of Z_{eff} = 2.7325, and covering a range of muon energies from 100 to 1000MeV. This covers the range where the minimum ionising point of Lithium Hydride is expected.

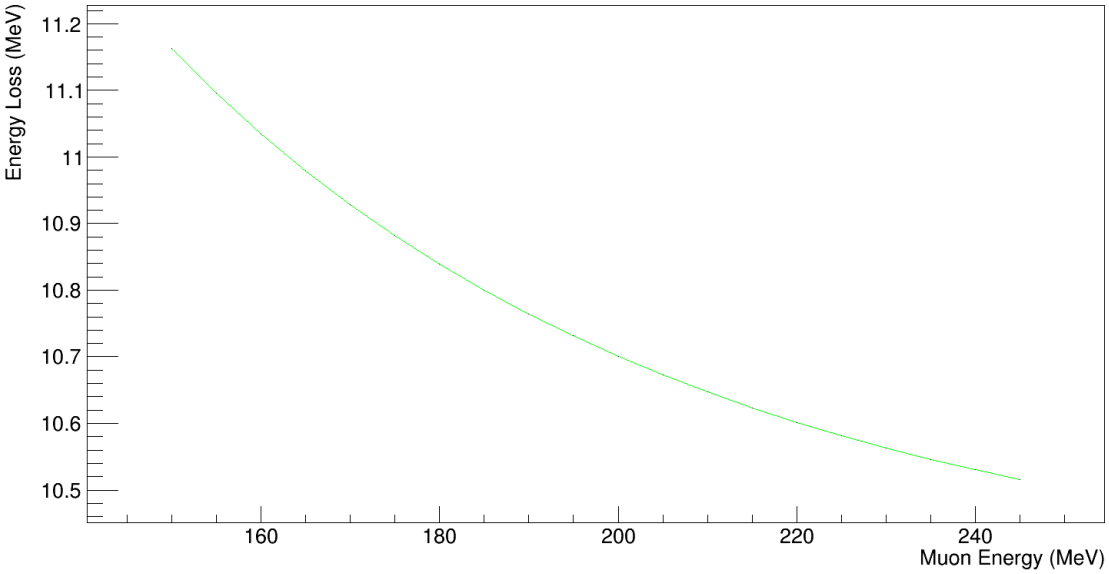

Figure 4.8: Mean energy loss of muons in 65mm of Lithium Hydride calculated from the Bethe equation, for the range of muon energies covered by the MICE experiment. Using an effective molecular mass of Z_{eff} = 2.7325.

The calculation to find the most probable energy loss was slightly simpler to run, as the

thickness of the absorber makes up part of the equation, and therefore the calculation doesn't require any iteration as the muon passes through the material. Figure 4.9 shows the most probably energy loss for a range of energies between 100 and 1100 MeV. The curve lies approximately 1MeV below the curve for the mean energy loss. Figure 4.10 shows a direct comparison of the two methods of calculation over the range of muon energies in MICE. At 200 MeV, the most probable energy loss lies at 10.05 MeV, whereas the mean energy loss lies at 10.70 MeV. This calculation therefore puts the most probable energy loss approximately 6% below the mean.

In practise, the most probable energy loss will be easier to measure than the mean energy loss, as it both will be easier to fit a function to the peak region to extrapolate values, and it will be less vulnerable to statistical fluctuations caused by the tail of the distribution.

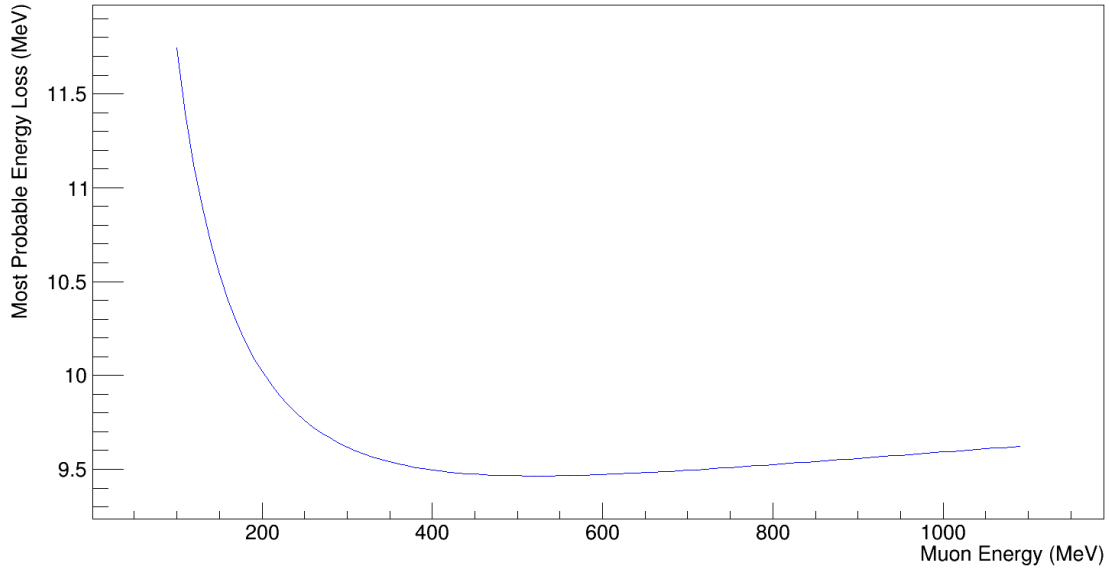

Figure 4.9: Most probable energy loss of muons in 65mm of Lithium Hydride calculated by equation 4.8. This is the point of the expected peak of the energy loss distribution.

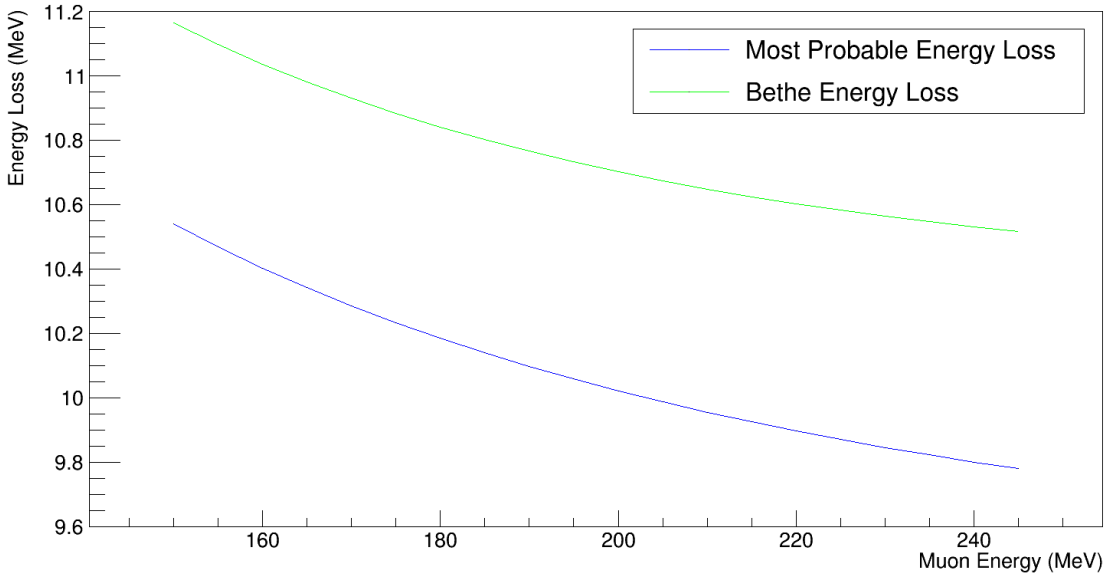

Figure 4.10: Most probable energy loss of muons in 65mm of Lithium Hydride calculated by equation 4.8 compared to the mean energy loss predicted by the Bethe equation, for the range of muon energies explored in the MICE cooling channel.

Chapter 5

Simulation of Energy Loss Measurement in Step IV

Step IV of MICE will provide the first measurements of transverse emittance reduction of a muon beam. This configuration of MICE is the first configuration to have the focus coil unit in the beam, and by extension the absorber. Tracker stations TKU and TKD are positioned directly either side of the absorber with nothing extra in-between. This makes Step IV the ideal opportunity to make measurements of muon energy loss inside the absorber.

At the time of writing, Step IV running with the solenoid field has not been completed. Therefore this chapter presents an energy loss analysis using results of Monte Carlo simulations of the Step IV setup produced in the MAUS software framework. Two methods of measuring the energy loss are presented. The first method uses the reconstructed muon momenta from the trackers to calculate the energy of the muon either side of the absorber, with the energy loss being the difference between the two. The second method uses the time-of-flight data from TOF1 and TOF2 to reconstruct the muon velocity either side of the absorber and get an energy loss from there. The second method is outlined in this chapter, and described in greater detail at the start of chapter 6.

5.1 Step IV

The Step IV configuration of MICE consists of one absorber unit but no RF cavities, meaning transverse emittance reduction will occur without the re-acceleration in the lon-

gitudinal direction anticipated in the final configuration. The absorber, a cylinder of Lithium Hydride, sits inside the AFC. Either side of the AFC are the two spectrometer solenoids. A schematic is shown in figure 5.1 and the components are described previously in chapter 3.

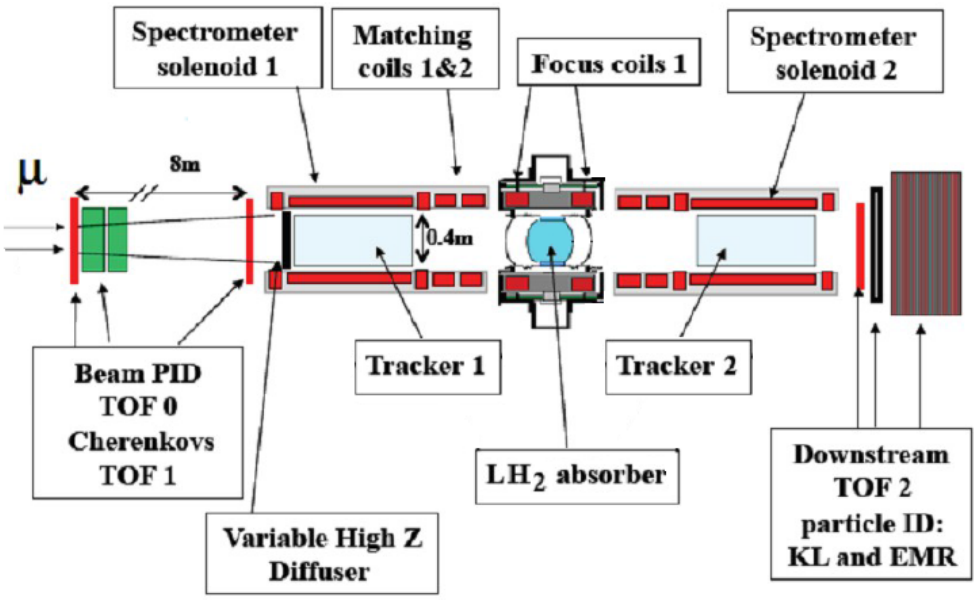

Figure 5.1: Labelled diagram of the MICE Step IV cooling channel.

5.2 SSD Descope

Issues during commissioning of the downstream spectrometer solenoid magnet (SSD) resulted in damage occurring in the magnet to its matching coil M1. Therefore the SSD will not run in the optimum 4T setup originally planned for the step IV running.
A new field map for the cooling channel was developed, that allow a 3T field in both SSU and SSD so that the tracker momentum resolution will not be too heavily compromised, and therefore the simulations were run primarily using the coil currents summarised in table 5.2.

Field maps of the magnetic field strength within the channel were produced using MAUS to demonstrate the difference between the expected field, and the descoped field. Figure 5.2 shows the reduced magnetic field in the channel, with a particular drop in field stength at 18m down the channel corresponding to the loss of the M1 coil. Figure 5.3 shows

	Current /A
SSU E2U	192.45
SSU CU	211.26
SSU E1U	187.112
SSU M2	236.83
SSU M1	135.21
FC	55.98
SSD M1	0
SSD M2	0
SSD E1D	132.95
SSD CD	150.11
SSD E2D	136.74

Table 5.1: Descoped currents used in the Step IV simulation.

the potential full field map. The main differences are the reduced fields in both solenoid magnets, with 3T in the SSU and 2T in the SSD. It can be seen in the new field map that the total magnetic field strength in the channel drops very low between the focus coil and the SSD. This cannot be compensated for by increasing the field strengths in SSD or the focus coil as the configuration must also protect the remaining coils of the SSD from further damage.

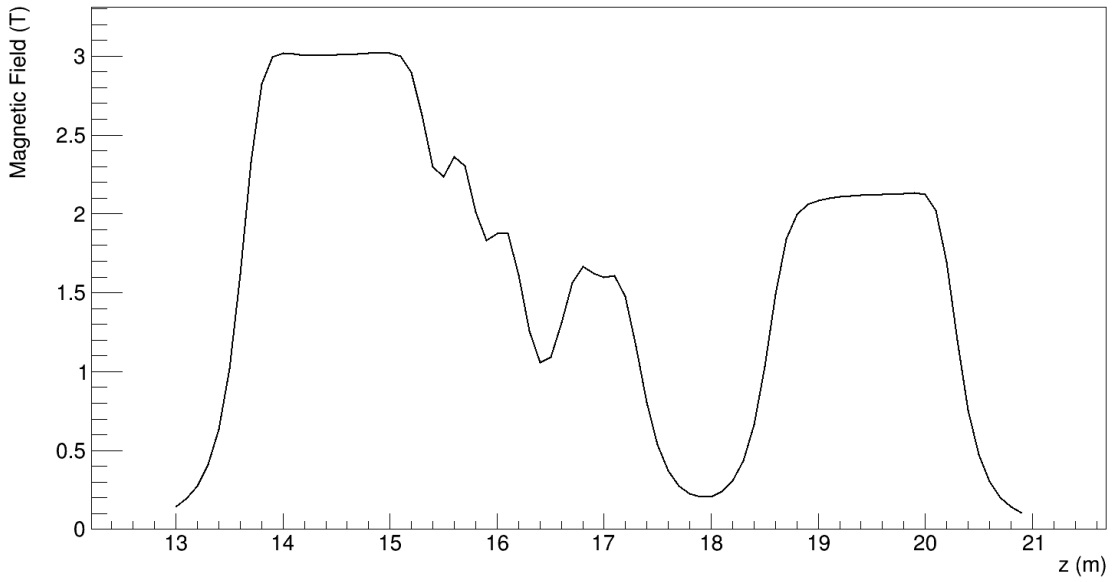

Figure 5.2: Map of the magnetic field strength through the cooling channel after the SSD descope. The initial peak at 3T corresponds to the upstream solenoid. There is a reduced 2T in the downstream solenoid to protect the magnet. At 17 meters lies the focus coil, with a peak magnetic field of 1.5T

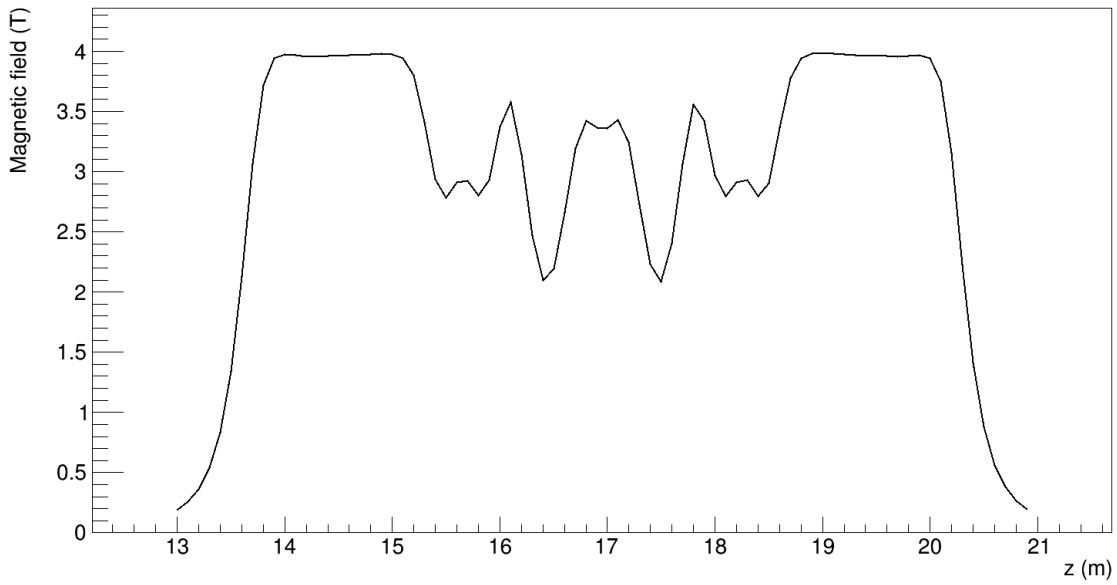

Figure 5.3: Map of the magnetic field strength through the cooling channel without the de-scope, with 4T in both solenoid magnets.

5.3 Simulation Details

In these simulations, we seek to make a measurement of the energy loss using the reduced field setup of MICE, as previous measurements have relied on a full 4T field through the solenoid magnets. Simulations of MICE were developed and run within the MICE Analysis User Software (MAUS) framework. MAUS uses the Geant4 physics libraries [62] to simulate interactions between the muons and the detectors, including scattering and energy loss. The different configuration of muon beam can be simulated using the MAUS BeamMaker, which controls the initial parameters of the simulated beam. In this way we can match the simulated beam to the real beam seen in MICE. A good example is seen using the dataset from run 07469 - one of the first runs with field in the SSU, and comparing this to monte carlo muon data. This comparison is carried out in the next chapter, where analysis on real data is carried out.

In our simulations a disk of Lithium Hydride was used as the absorber, with dimensions matching that of the real LiH absorber.

5.4 Calculating the Energy Loss

There are two methods used in the following sections to measure the energy loss in MICE. The first method is simpler to implement, however it requires a working cooling channel with field in the solenoid magnets, to allow full momentum reconstruction in the trackers.

The momentum of the muon can be reconstructed from the downstream tracker, and subtracted from the upstream momentum to obtain the energy loss in the absorber unit.

To correct for background sources of energy loss, first a measurement of the energy loss in the empty absorber is made. This will measure the contribution to the energy loss from materials such as the windows of the absorber unit. Then after this is taken, the energy loss can be measured with the absorber material in place.

The second method of measuring the energy loss involves using the velocity of the particle throughout the cooling channel, measured using the time-of-flight data obtained from the TOF detectors. This is a more complicated calculation, however does not require any field in the solenoid magnets. This method involves the following steps:

- First, the momentum of the muon after TOF1 is reconstructed.
- Using the known energy loss of the tracker planes, the velocity and energy of the muon is calculated at a point just before the absorber.
- Using the velocity of the muon before the absorber, the time taken for the absorber to travel from TOF1 to the absorber can be determined.
- This time is then compared to the time-of-flight between TOF1 and TOF2, to get the particle time of flight after the absorber to TOF2.
- Using a recursive method, the velocity of the muon after the absorber can be extrapolated.
- Once the velocities of the muon before and after the absorber are known, their equivalent energies can be calculated, and the energy loss measured.

This method is explored in further detail at the start of chapter 6. In this chapter, primarily the first method is explored using data from MAUS simulations of the cooling channel. In the next chapter, real data with no field in the solenoid magnets is used with the second method to measure the energy loss.

5.5 Momentum Reconstruction in Trackers

The Energy Loss of a muon in the MICE beamline from the tracker data is obtained by comparing the energy of a muon taken after the absorber to its momentum before the absorber and measuring the difference. Using the trackers positioned either side of the

absorber.

In the tracker analysis, simulated data reconstructed in the trackers is used to predict how well the energy loss can be measured in LiH. MAUS includes digitisation parameters for each detector which simulate accurately the resolution and response of each detector, and allows MAUS to treat simulated data just like real data for the purposes of testing the reconstruction and allowing analyses to be run against monte-carlo generated data. With this method one can draw conclusions on the accuracy of the final measurement

In the MAUS simulation, the simulated muons properties are measured throughout the simulated cooling channel in a series of virtual planes. This means that to get the properties of the ”true” simulated muon at any point, it is simply required to find the virtual plane at the desired longitudinal position, and this object will return the muon properties. This data is often referred to as the ”monte carlo truth data”, or simply ”truth data”, as it represent the properties of the muon unaffected by detector resolution.

The truth data obtained from the MAUS simulation will be used to find the momentum distribution of the simulated muons at various points throughout the cooling channel that correspond to the locations of the detectors. The truth data at these points can then be compared with the momenta of muons calculated using the reconstructed algorithms on the simulated digits data. Through this method a measurement of the resolution and accuracy of the reconstruction algorithms can be made.
The first step is to look at the distribution of the reconstructed muon momentum at each tracker vs the momentum of the truth data. This check ensures that the distribution of reconstructed muons matches what is expected from the simulation, and that the simulated beam is performing also as expected. Once this is done, the difference between the reconstructed momentum and truth momentum can be measured to obtain a residual difference for muons at each detector.

Finally, the momentum is converted to energy through $E^2 = p^2 + m^2$ and the energy loss of a muon can be measured. This is done for two sets of data. The first is a set of data that does not contain the primary absorber, so that contributions to the energy loss from extra sources such as air and the Aluminium windows can be measured. The second set contains the LiH disk absorber. From these, an average energy loss can be measured that only contains contributions from the Lithium Hydride.

Figure 5.4 shows the reconstructed momentum just before TOF1 using the rayner reconstruction algorithm [17]. This is a good indication of the shape of the momentum curve at the start of the cooling channel. The mean momentum is 217.6 MeV/c which is what is

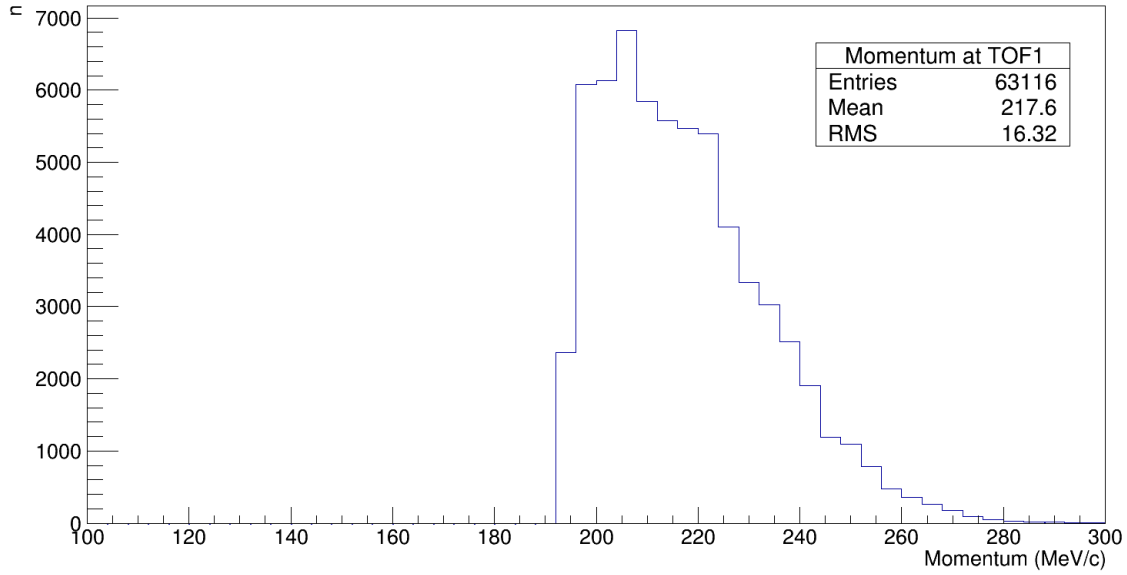

Figure 5.4: Momentum distribution at TOF1.

expected for this simulated beam, as the beam will lose momentum as it passes through the TOF1 detector to reach around 200 MeV/c in the upstream part of the cooling channel. Indeed, in figure 5.5 is shown the momentum distribution for muons at the upstream

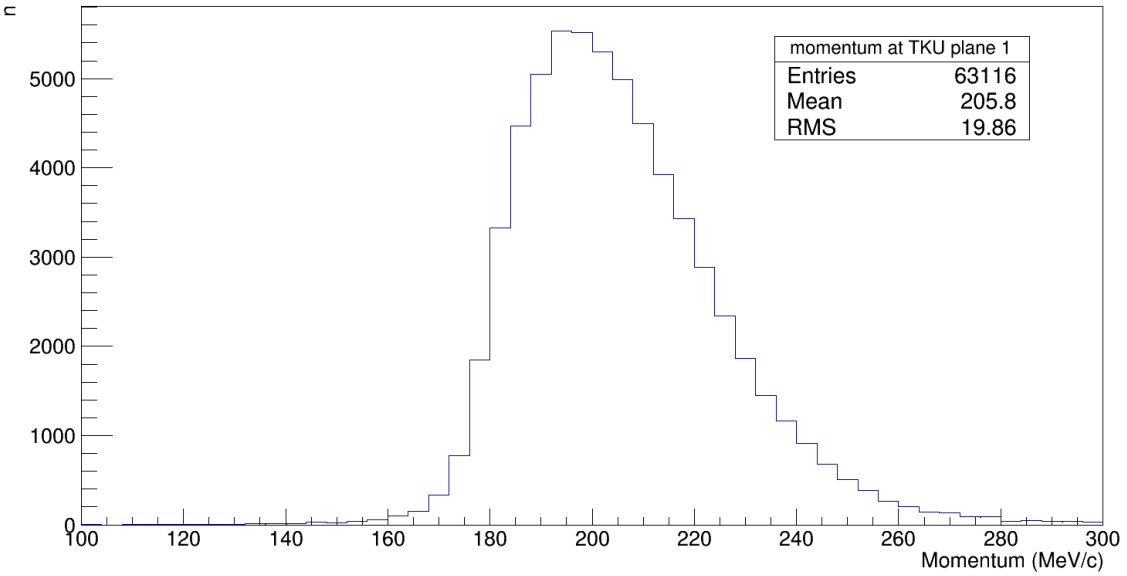

Figure 5.5: Momentum distribution at TKU1.

detector (TKU), at the plane closest to the absorber. It makes sense to measure the momentum at the closest planes to measure only the affects that happen inside the absorber unit. The distribution of the momentum follows the shape of the curve of the TOF1 momentum curve in figure 5.4, and the average momentum is lower due to the energy loss as the muon passes through the TOF1 detector and the planes of the detector.

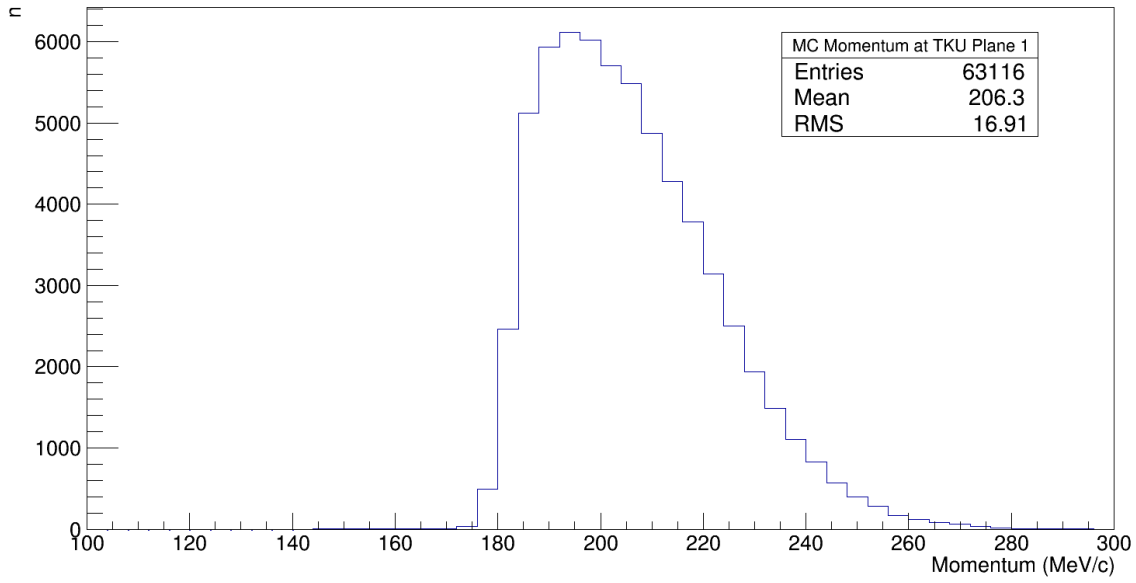

Figure 5.6: Momentum distribution from simulation data at TKU1.

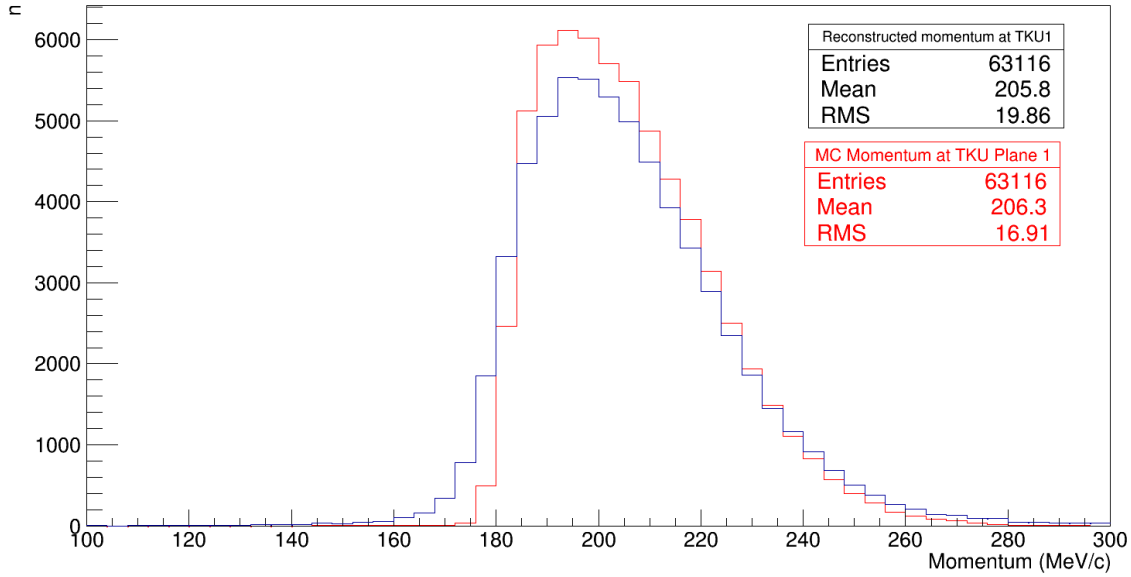

Figure 5.7: Comparison between reconstructed and simulated momentum at TKU plane 1.

Figure 5.6 shows the muon momentum data obtained from the monte carlo truth data at the same virtual plane where the tracker reconstruction at plane 1 occurs. Extracting this data allows us to make a comparison between the truth data and the reconstructed data and measure the performance of the reconstruction. Figure 5.7 shows the monte carlo truth and the reconstructed data sets for momentum at TKU overlaid. The shapes of the distributions are very similar, and the average momentum measured are also in agreement. However, the reconstructed momentum has a larger RMS. This is expected due to the resolution of the detectors smearing the distribution.

Figure 5.8 shows the residual plot of muon momentum for reconstructed and MC truth

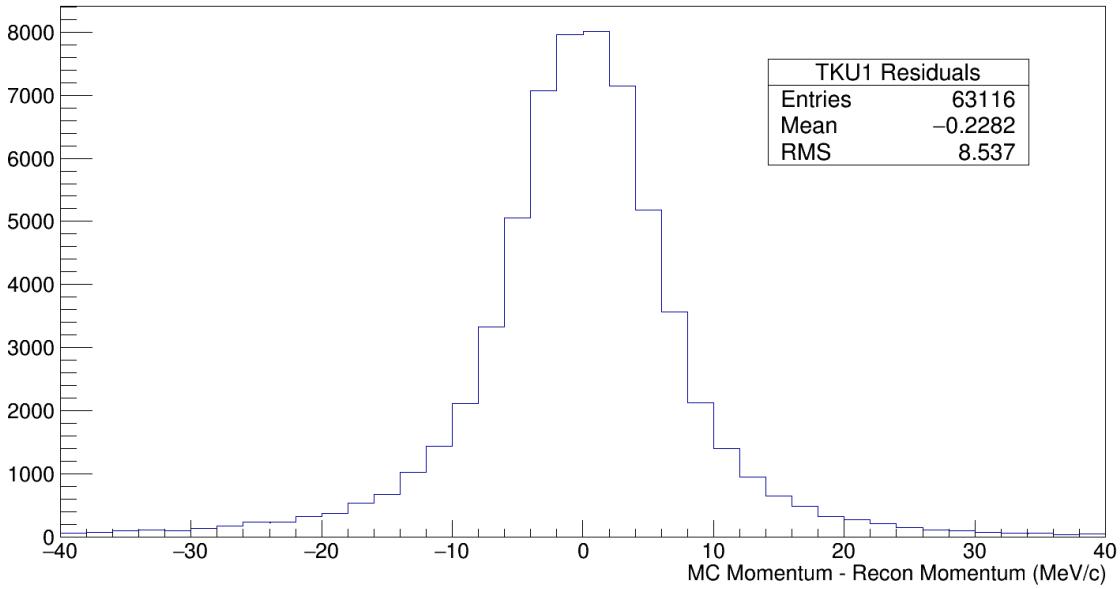

Figure 5.8: Difference between reconstructed and simulated momentum at TKU plane 1.

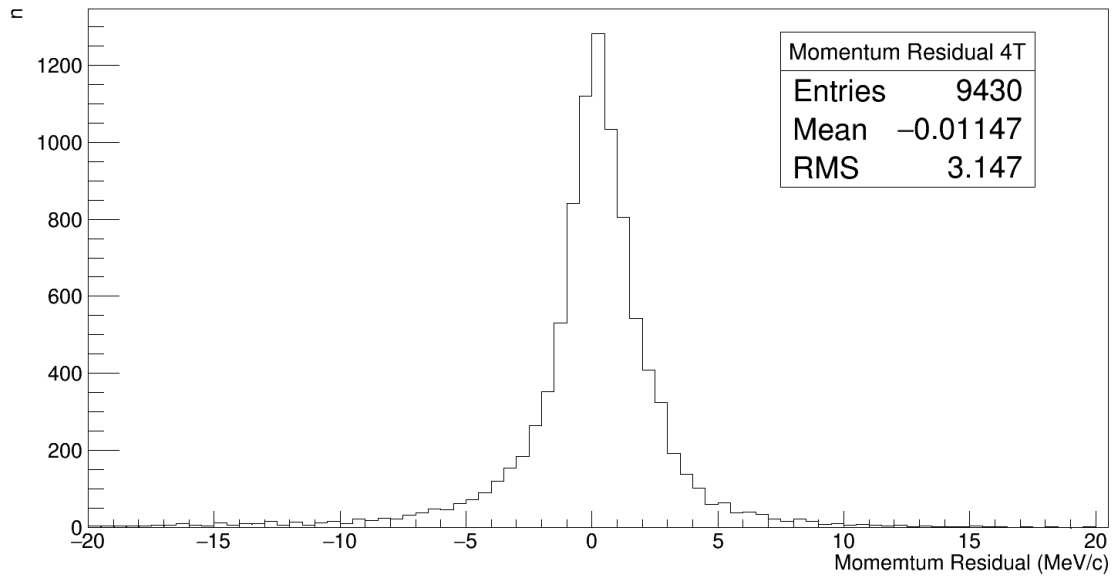

Figure 5.9: Difference between reconstructed and simulated momentum at TKU plane 1 for simulated data with 4T in the solenoid magnets. The width is slightly smaller than the residuals for the descoped field map.

muons in the descoped field. There is a small offset here of -0.22MeV/c indicating that the reconstructed momentum may be slightly higher than that seen, however it is easy to correct for this in the analysis. The RMS of the distribution is 8.5 MeV/c and provides an indication of the tracker performance. In this instance, it is much higher than the expected 3-4 MeV resolution when a 4T field is run in the SSU, due to the tracker reconstruction

relying on the helical track of muons to reconstruct momentum along the z-axis (along the beam). For comparison, an example of the possible residual with a 4T field is shown in figure 5.9.

Note that if the momentum is split into its transverse and z components (with z being in the direction of the beam), then its seen that the transverse momentum is very well reconstructed (see figures 5.10, 5.11) and therefore most of the contribution towards the resolution comes from the z momentum component as shown in figure 5.12.

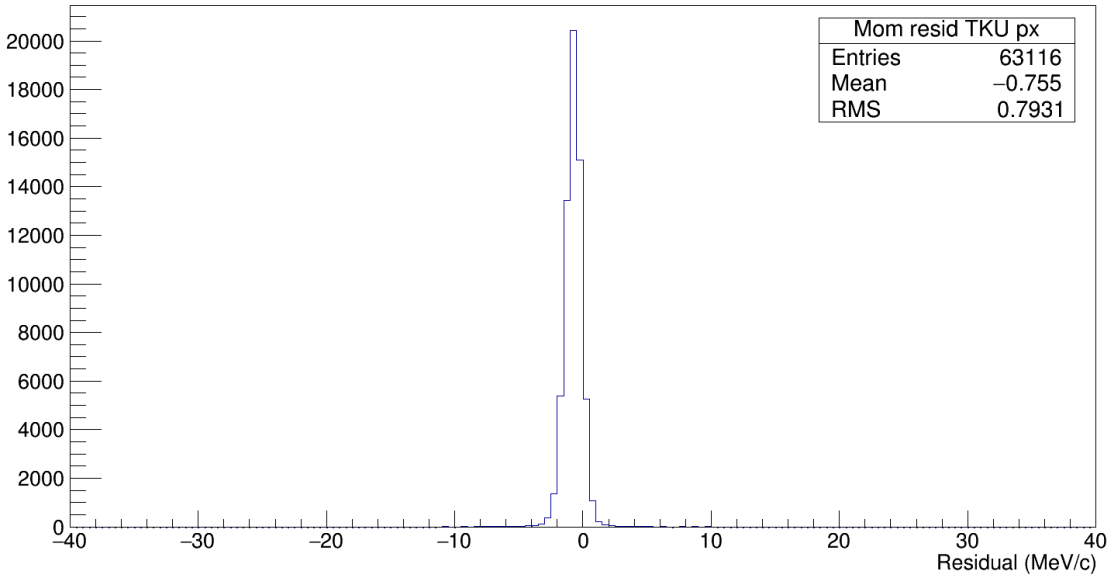

Figure 5.10: P_x residual for reconstructed and MC truth muons.

The figure 5.13 shows the momentum distribution for muons at the downstream tracking detector. Compared to the distribution shape of the TKU detector in figure 5.5, the main difference in features is the small tail to lower momentums at around 140-160MeV/c.

Comparing the reconstructed momentum to the MC truth data in figure 5.15, a similar pattern is seen as from the TKU (figure 5.7), where the reconstructed and simulated distributions share the same shape but the reconstructed momentum is wider.

Finally for the TKD, figure 5.19 shows the residual difference for the momentum for each muon. The mean is reasonably central, with a small offset, and the RMS is 7.95 MeV/c. This reasonably matches the RMS seen in the residual for the TKU in figure 5.8, which means the detectors are exhibiting identical behaviours in this simulation. Figures 5.16, 5.17 and 5.17 again show that the contribution towards the overall resolution of the momentum is dominated by the contribution of the longitudinal component.

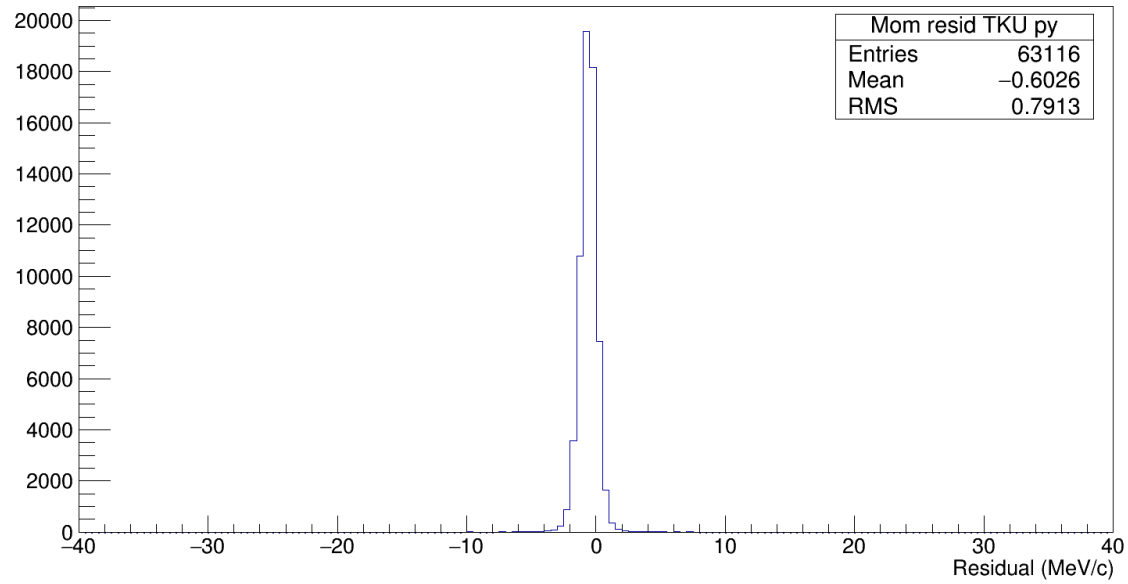

Figure 5.11: P_y residual for reconstructed and MC truth muons.

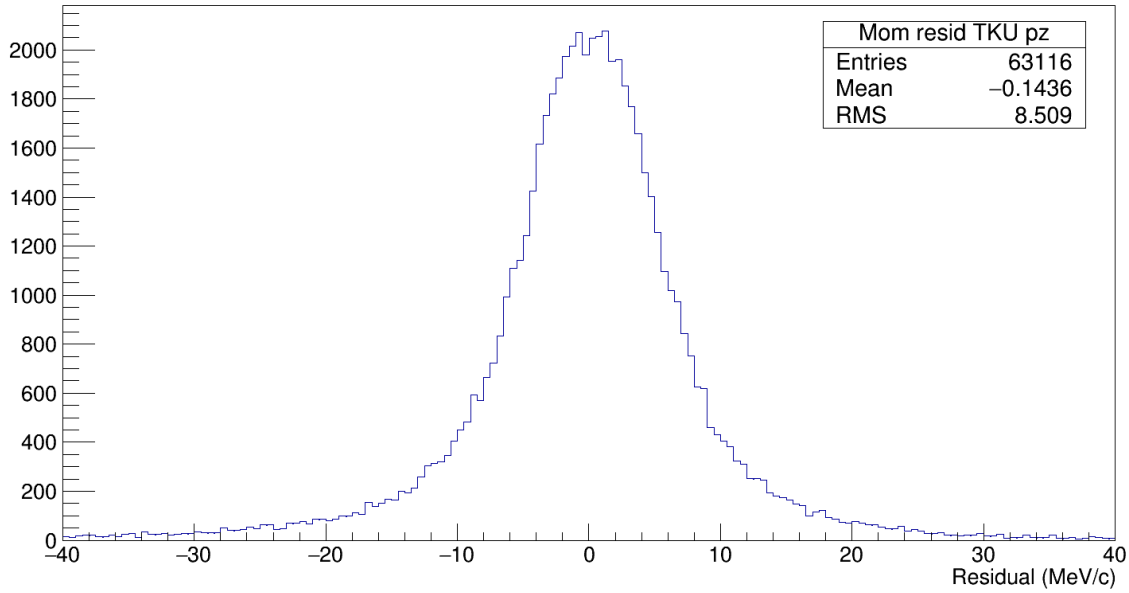

Figure 5.12: P_z residual for reconstructed and MC truth muons.

5.5.1 TOF1 to TOF2 time Discrepancy

In the reconstruction of MICE, there appeared a 0.5ns discrepancy between the reconstructed muon time-of-flight between TOF1 and TOF2. This is shown in figure 5.20. Although the cause of this discrepancy was not identified, the offset is easy to correct for in the reconstruction by simply subtracting 0.513ns from the time-of-flight between TOF1 and TOF2, shown in figure 5.21.

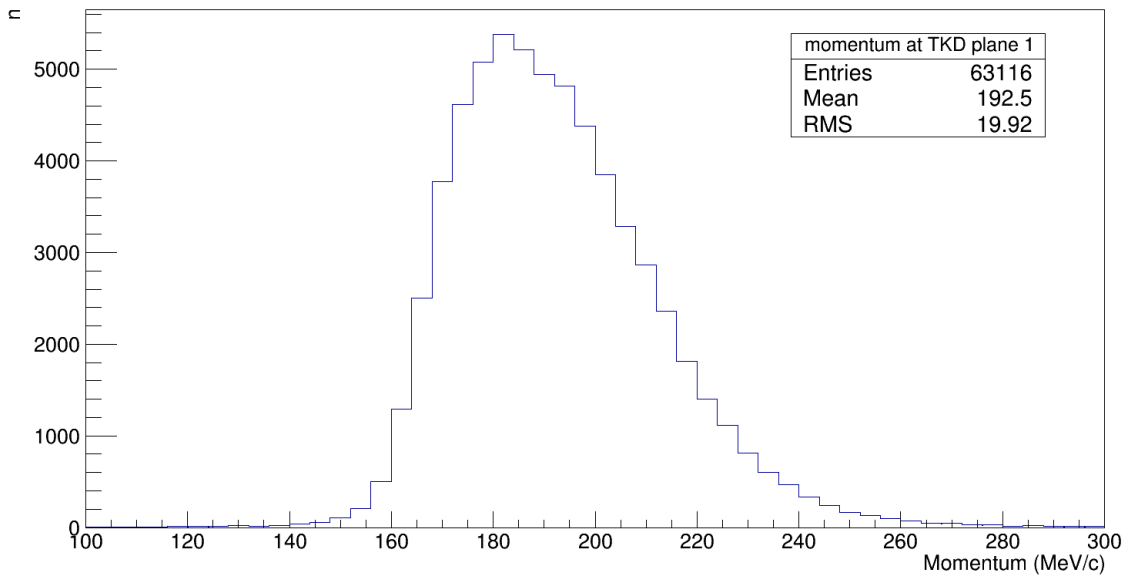

Figure 5.13: Momentum distribution at TKD.

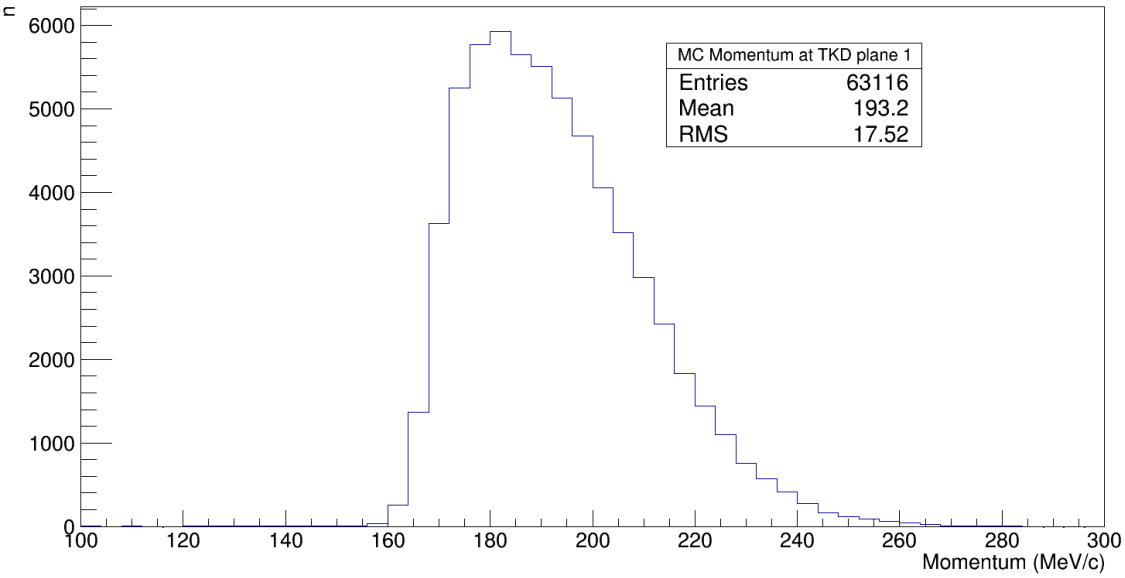

Figure 5.14: Momentum distribution from simulation data at TKD1.

5.6 Energy Loss

As previously discussed, the simulation was run with two main configurations. The first configuration does not have an absorber inside the focus coil, which allows a measurement of background energy loss processes and contributions to be made. This includes measuring the energy loss in the Aluminium windows of the focus coil. The second configuration then adds the LiH absorber disk. Once a measurement is taken for both configurations the energy loss contribution from only the LiH can be measured.

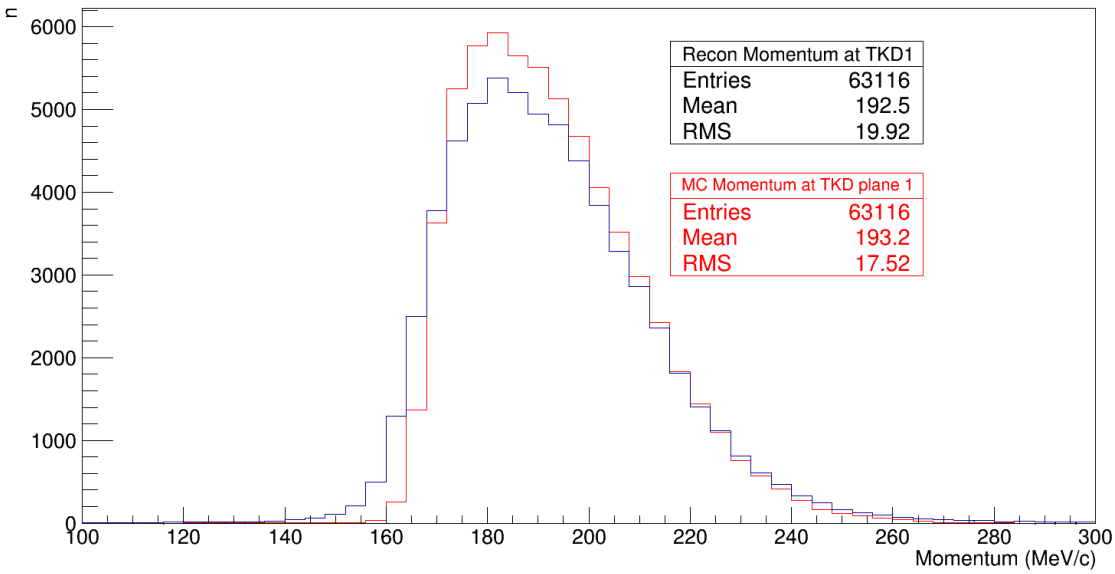

Figure 5.15: Comparison between reconstructed and simulated momentum at TKD plane 1.

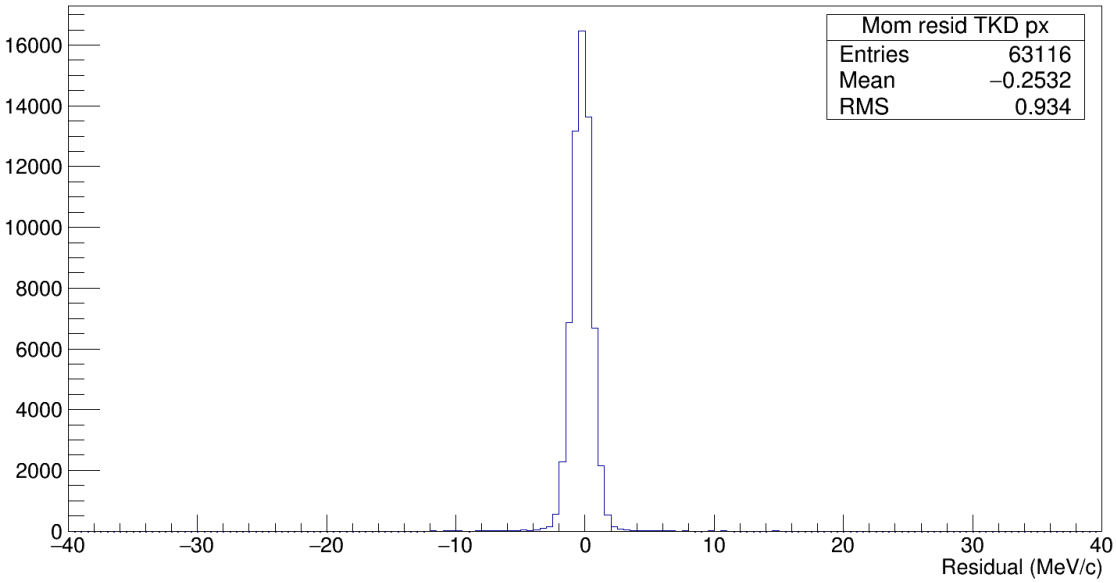

Figure 5.16: P_x residual for reconstructed and MC truth muons.

5.6.1 Uncertainties

The biggest contribution of error on the measurement will come from the performance of the detectors. As seen in figures 5.8 and 5.19, the resolution of the trackers with this reduced field is only around 8 MeV at best. Therefore a measurement of features of energy loss such as the amount of straggling will not be possible. However, it will be demonstrated later that it is still very possible to reconstruct an energy loss peak. By fitting to this peak a convoluted function with gaussian and landau parameters, it will be possible to make a measurement of the value of the peak. We choose these functions as the en-

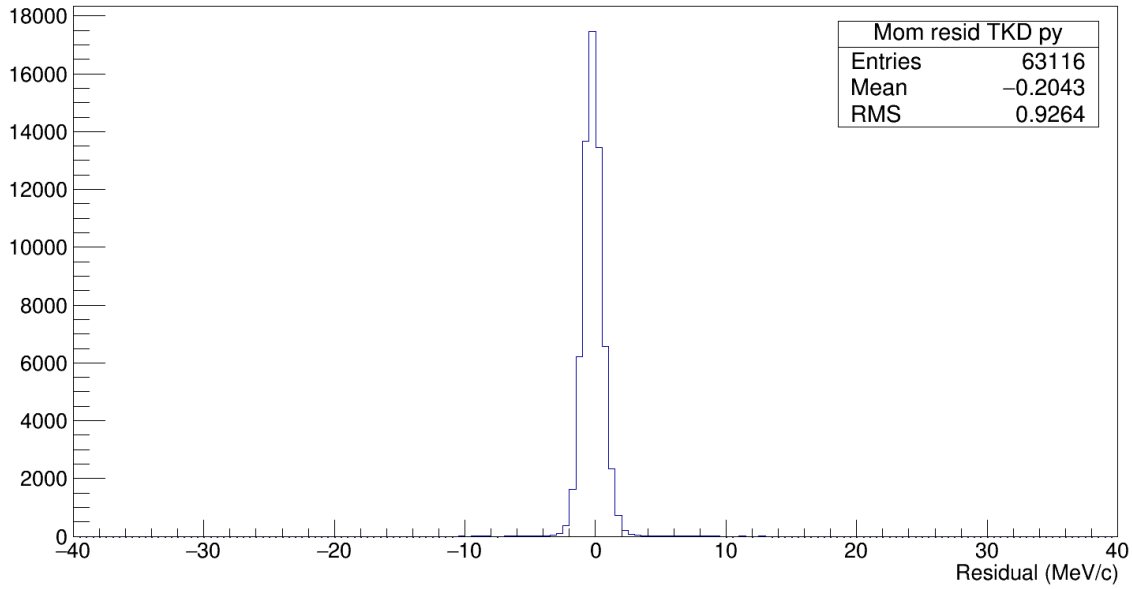

Figure 5.17: P_y residual for reconstructed and MC truth muons.

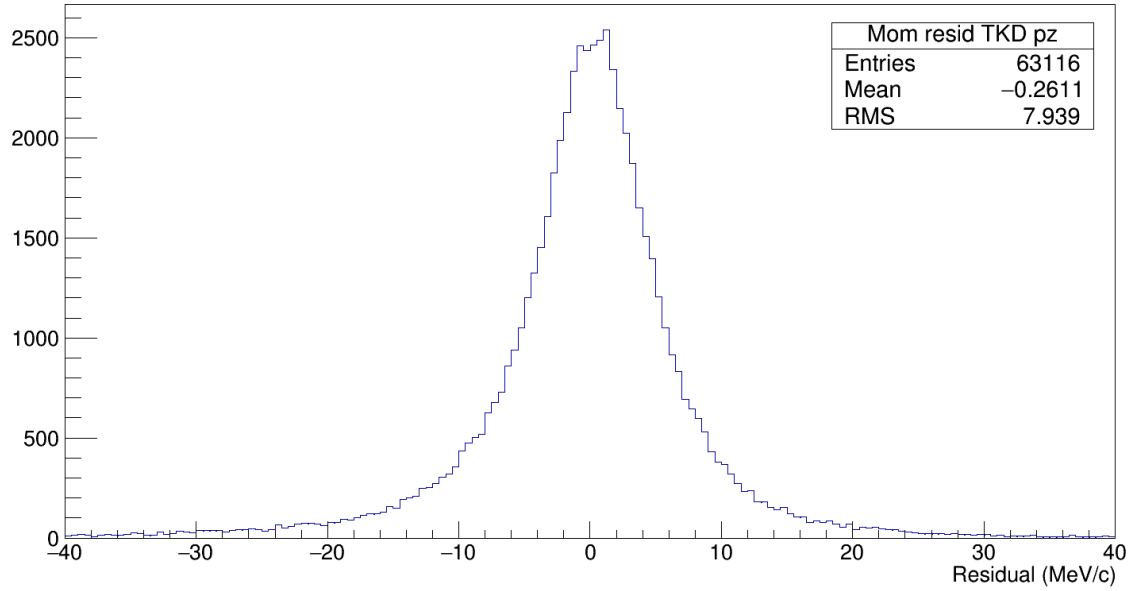

Figure 5.18: P_z residual for reconstructed and monte carlo truth muons.

ergy loss is expected to be best desbribed as a landau distribution. The error on the energy loss comes from the detector resolution which can be approximated to a gaussian function.

When fitting a landau-gaussian function to the data, effort is made to ensure that the curve best describes the peak region of the graph, as we are most interested in obtaining a value for the peak. This means however that the range of fit is often limited to the region of the peak.

Statistical errors on this measurement can be calculated by using the width of the distri-

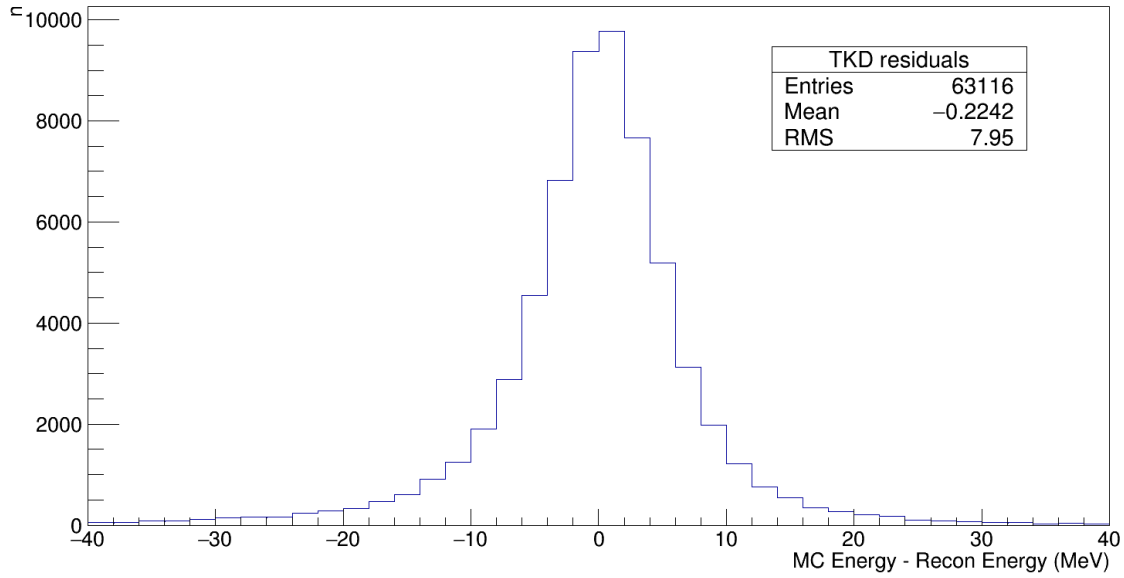

Figure 5.19: Difference between reconstructed and simulated momentum at TKD plane 1.

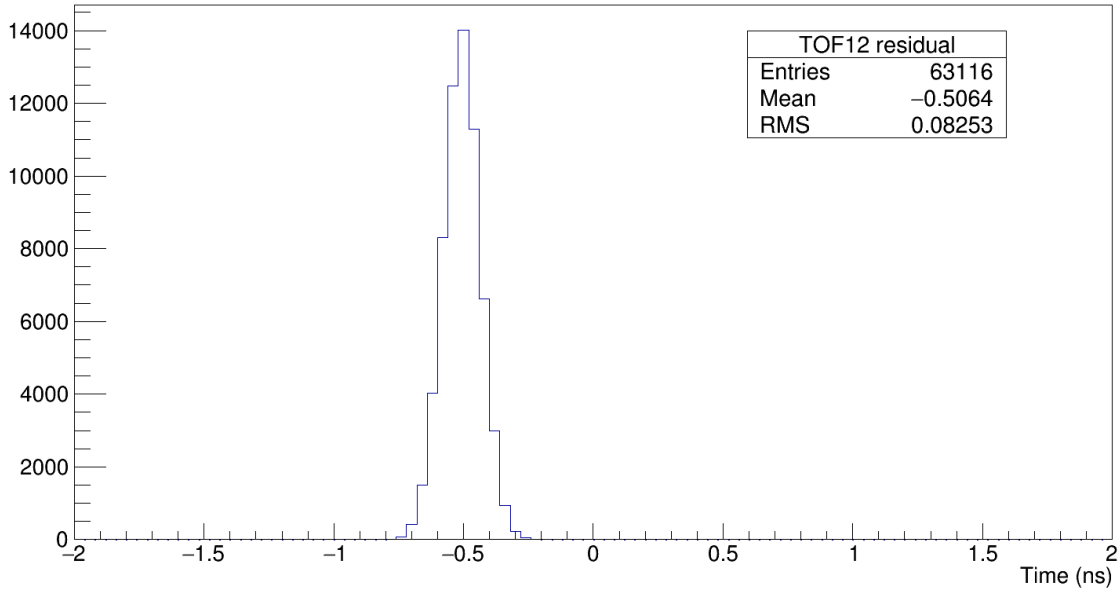

Figure 5.20: Non-corrected difference between MC and reconstructed time of flight between TOF1 and TOF2 after correction. Note the 0.5ns offset of the distribution from zero.

bution and consideration of the number of events that fit the selection criteria.

Other sources of uncertainties are generally negligible when compared to the detector effects. The Lithium Hydride disk used in MICE has been xray'd and the density was found uniform across the disk [7]. Contributions to the Energy Loss from extra sources such as air and the aluminium windows on the absorber unit inside the focus coil will be

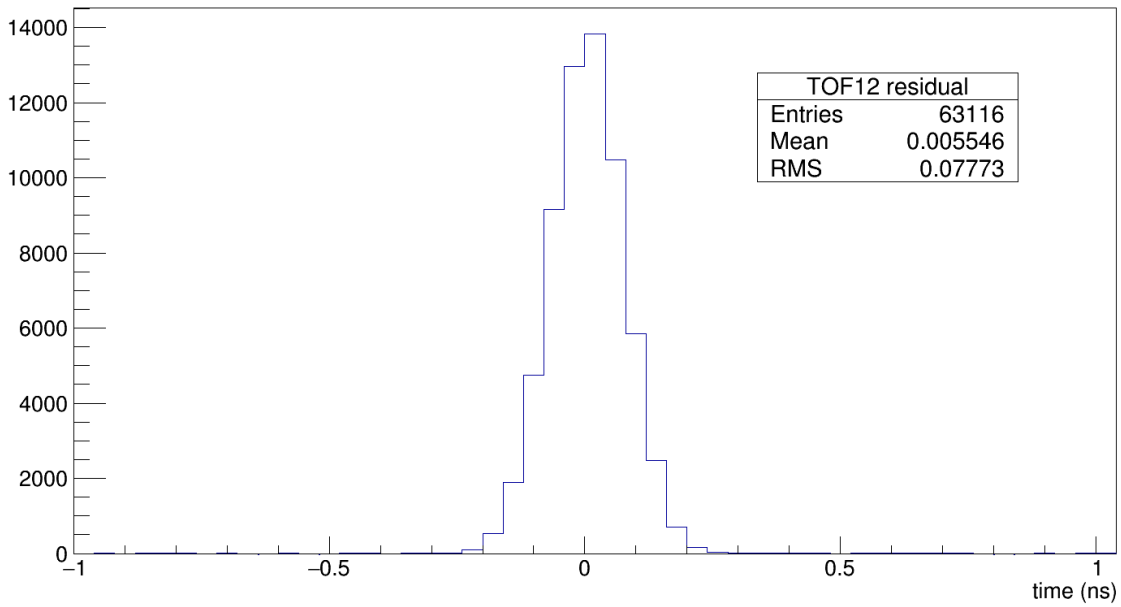

Figure 5.21: Residual difference between MC and reconstructed time of flight between TOF1 and TOF2 after correction.

accounted for by making an initial measurement of energy loss without the absorber in place.

5.6.2 Systematics

Systematic errors will predominantly arise from contributions towards the energy loss of muons from sources other than the Lithium Hydride absorber. Additional energy loss will, for example, take place in the detectors throughout the experiement (TOF detector, each tracker plane), and the air in the cooling channel. To account for this, measurements of the energy loss in the cooling channel without the LiH absorber in place are first taken. Figure 5.22, discussed further in the next section, gives a simulated value for the most probable energy loss in the cooling channel without LiH at 1.31 MeV. This value can later be subtracted from the measurement of energy loss including the LiH, to give only the contribution to the energy loss by LiH.

The residual plots discussed earlier in the chapter show that there is a relatively small offset between the true and reconstructed values for the particle energy in the detectors. We can account for this systematic by making a correction to the measured value.

5.6.3 Empty Absorber Unit

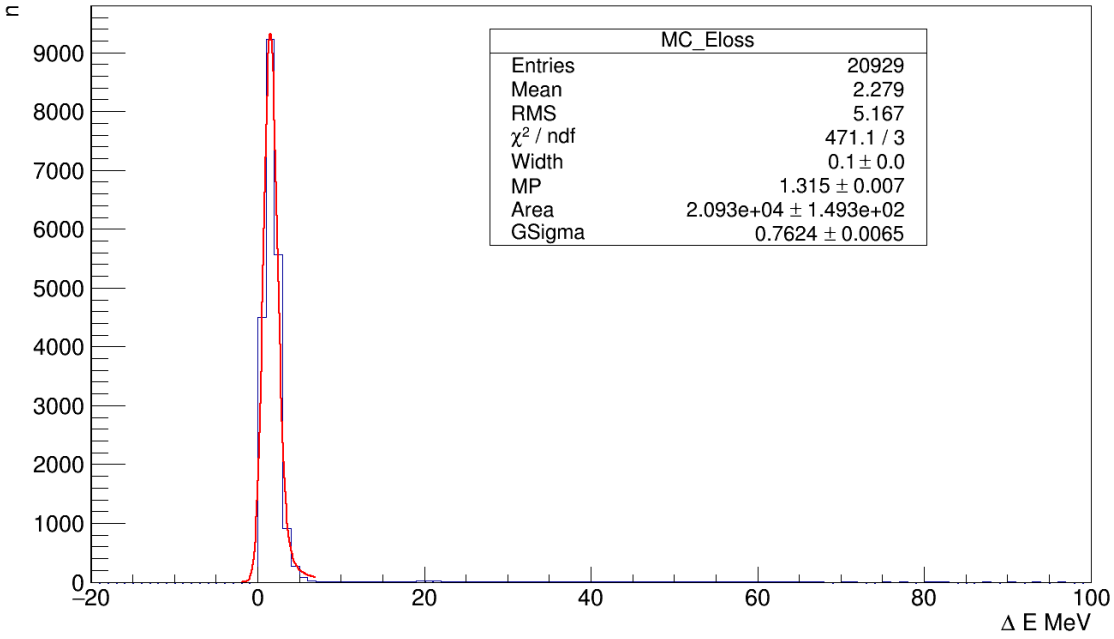

Figure 5.22: Monte carlo Energy loss measured in the Empty Absorber unit.

Figure 5.22 shows the simulated energy loss for muons passing through the absorber unit, where no absorber is present, meaning the only contributions are air and the Aluminium windows as previously discussed. The distribution has been fitted with a convoluted landau-gaussian function. The most probable energy loss will correspond to the MP parameter of the landau, which in this instance is 1.31 $\pm$ 0.03 MeV. This figure is in line with what is the predicted energy loss from the air and aluminium sources calculated using the Bethe equation in chapter 4.

In figure 5.23, the energy loss distribution for muons obtained using the reconstructed tracker data is shown. The peak is fitted with a convoluted landau-gaussian function. The most probable energy loss can be measured at 1.28 $\pm$ 0.06 MeV, which is in agreement with the simulated data. The statistical error on the most probable energy loss is calculated from the number of events, and the RMS of the fitted function.
This agreement is further demonstrated in figure 5.24, which shows the reconstructed energy loss overlaid onto the simulated-truth energy loss distribution. What is made clear by this plot is the effect on the shape of the distribution as a result of the resolution of the trackers. The ionising peak is much wider on the reconstructed energy loss with an increase on the RMS by around 7 MeV, making this almost entirely dominated by detector effects.

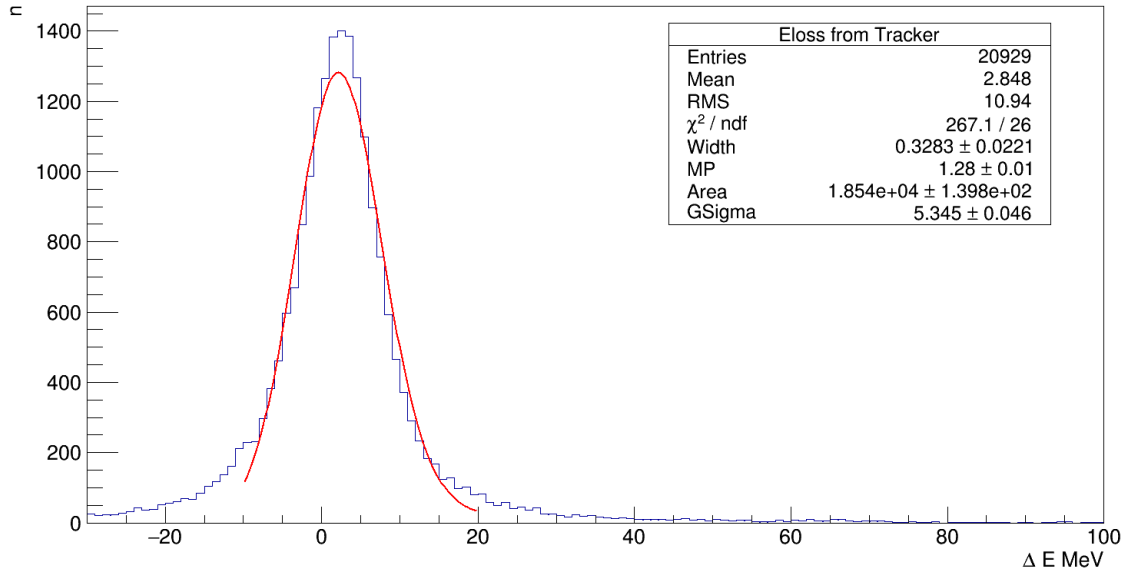

Figure 5.23: Reconstructed Energy loss for Empty Absorber data.

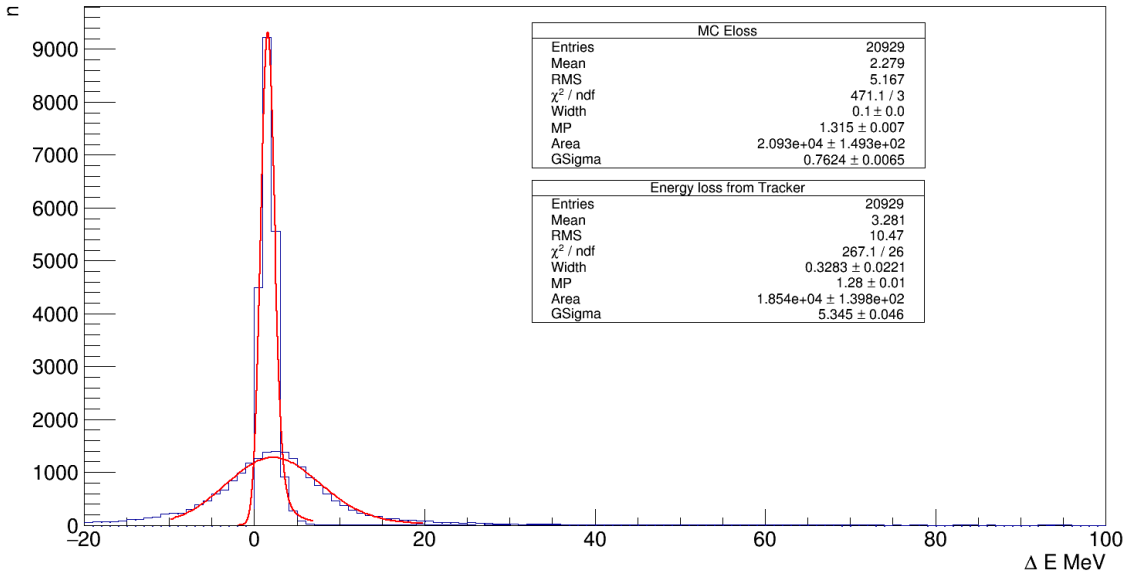

Figure 5.24: Reconstructed energy loss in the empty absorber for simulated muons passing through the absorber unit with the Lithium Hydride cylinder installed.

5.6.4 LiH Absorber

Figure 5.25 shows the simulated energy loss for muons passing through the absorber unit with the Lithium Hydride absorber present. As previously done, a convoluted gaussian-landau function has been fitted to the peak, which indicates that the most probable energy loss is at 10.63 MeV. The function was evaluated against various ranges of data in order to best fit the function to the peak region. If the contribution from extra sources is subtracted from the calcluated MP value, an energy loss from only the Lithium Hydride is measured at 9.32 MeV. This is in line with the expected energy loss calcuated in chapter 4 from the

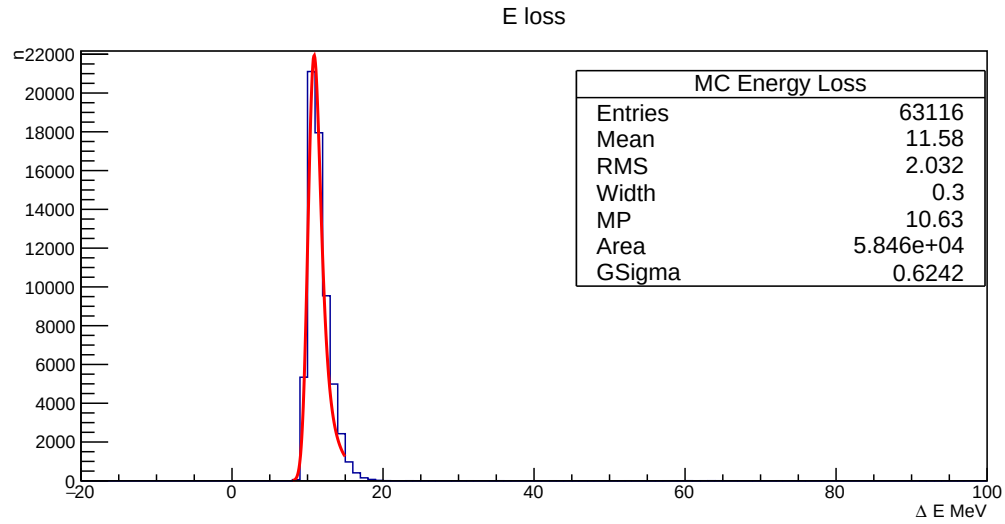

Figure 5.25: Simulated energy loss for muons passing through the absorber unit with the Lithium Hydride cylinder installed.

landau equations for energy loss.

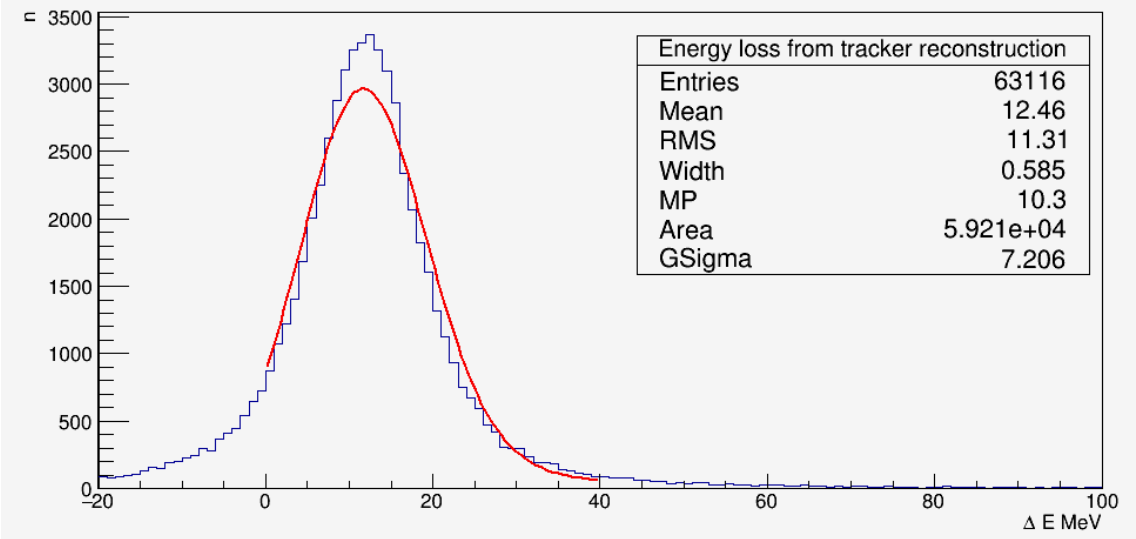

Figure 5.26: Reconstructed energy loss in Lithium Hydride for simulated muons passing through the absorber unit with the Lithium Hydride cylinder installed

Figure 5.26 shows the reconstructed energy loss measured from the LiH absorber. The mean of the distribution lies at 12.46 $\pm$ 0.04 MeV, which is influenced by the tail to high energy losses. Therefore as before a convoluted gaussian-landau function is fitted to the region with the peak. The MP, or minimum point, represents the most probable energy loss for muons passing through the material. In this instance the most probable energy loss lies at 10.30 $\pm$ 0.04 MeV. From this value we can take away the contribution to energy loss by the absorber, to obtain the erergy loss by LiH of 9.07 $\pm$ 0.12 MeV.

This is in agreement with the raw simulated data. Figure 5.37 shows the simulated and reconstructed distributions overlaid, and it can clearly be seen that the tracker resolution has had a significant impact on the shape of the distribution.

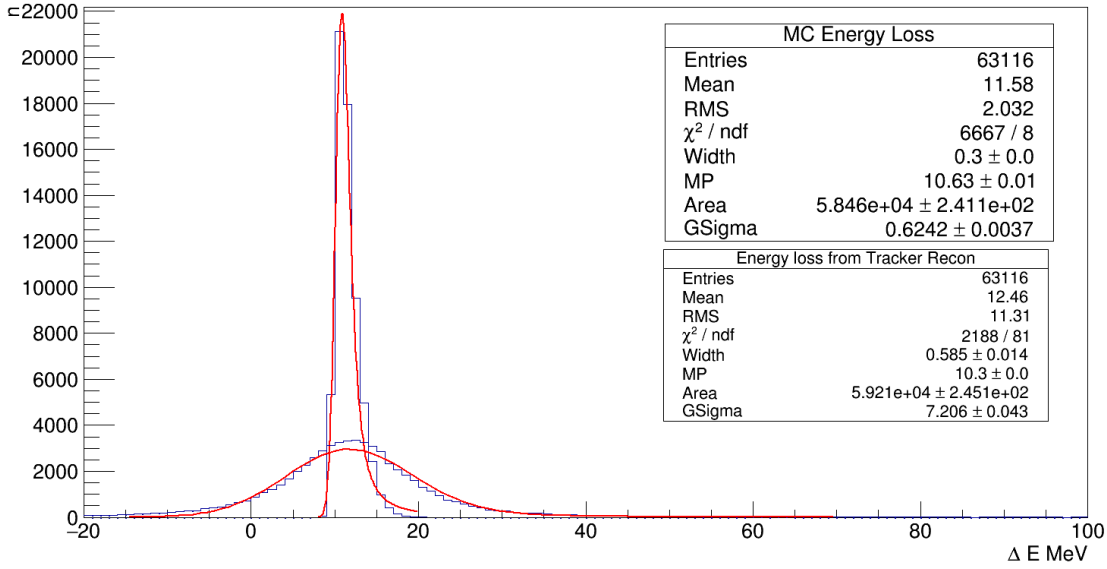

Figure 5.27: Simulated energy loss distribution compared to the reconstructed energy loss from tracker data.

5.6.5 Field-on Analysis Conclusions

So far, the most probable energy loss reconstructed in the simulation using the trackers has been in line with the most probable energy loss predicted by the simulation. The simulated data has identified potential sources of error, such as the offsets in residuals and in particular the offset between the reconstructed time-of-flight between TOF1 and TOF2. This offset has been investigated at length by the collaboration but to date no explanation has been found, so it is reasonable to consider this a systematic offset for the purpose of this analysis.

The energy loss distribution has a tail to high energies as expected, making a measurement of the mean energy loss difficult. However, the most probable energy loss is well measured, despite the fact that the trackers are unable to perform optimally due to the reduced field. The values given for the most probable energy loss at 9.07 ± 0.12 MeV are slightly below those predicted from calculation. This is most likely because the MAUS simulation is able to provide a better simulation of the interactions between the muon and the absorber during the muons passage through it.

5.7 Tracker vs Time reconstruction

In this section, a comparison is made between the energy reconstruction of the trackers versus the reconstruction by using the TOF data. Although the reconstruction for TOF data is designed to be used in the beam when there is no field, it can also be applied to field on data to improve the measurement. This also provides an opportunity to compare details of the measurement in each process and determine the relative performance of the methods. Ideally, both methods will be in agreement which will lead to an improvement of the resolution of the final measurement.

Figures 5.28 and 5.29 show the residual between the muon energy reconstructed from time, and the monte carlo truth momentum taken at virtual planes immediately either side of the absorber. Both residuals are centred on zero. After this comparison is made, then the energy loss for an empty absorber unit is measured.

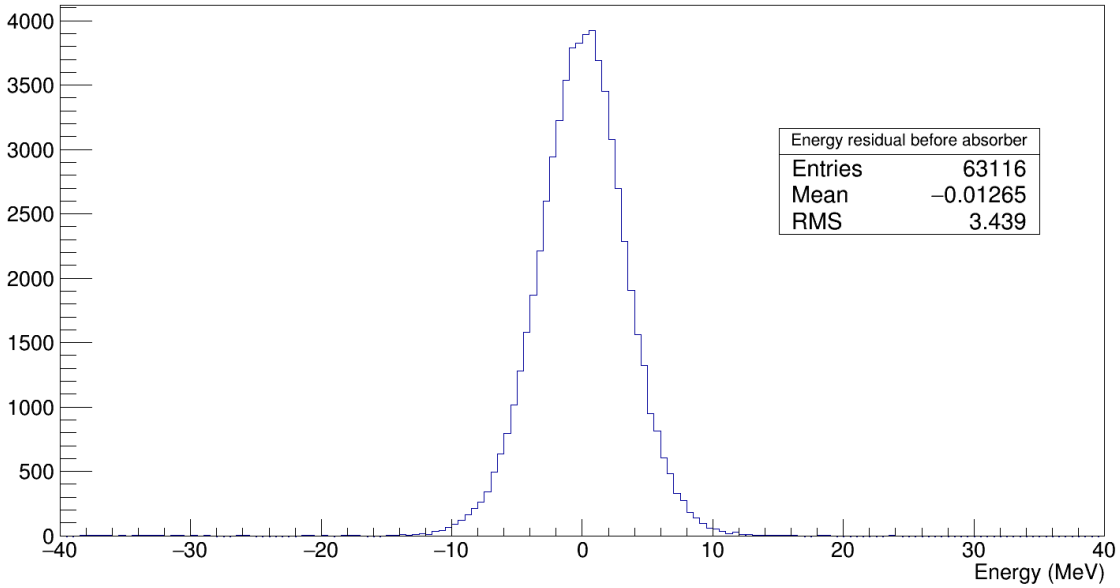

Figure 5.28: Residual between the monte carlo truth energy, and the energy reconstructed from time-of-flight data of muons just upstream of the absorber.

The energies measured either side of the absorber are also compared to the reconstructed energies measured from the trackers to check their agreement. Note that as there has been no data collected so far for field in the entire detector, these comparisons are made using the simulated Step IV dataset analysed in section 5.6.
The difference between energies measured before and after the absorber are shown in figures 5.30 and 5.31. In both instances, the energy measured from the time reconstruction is greater than the tracker energy by approximately 0.25MeV. This difference comes from the offset between truth and reconstructed energies of the trackers (see figures 5.12 and 5.18), as we showed in figures 5.28 and 5.29 that the energies reconstructed from the TOF

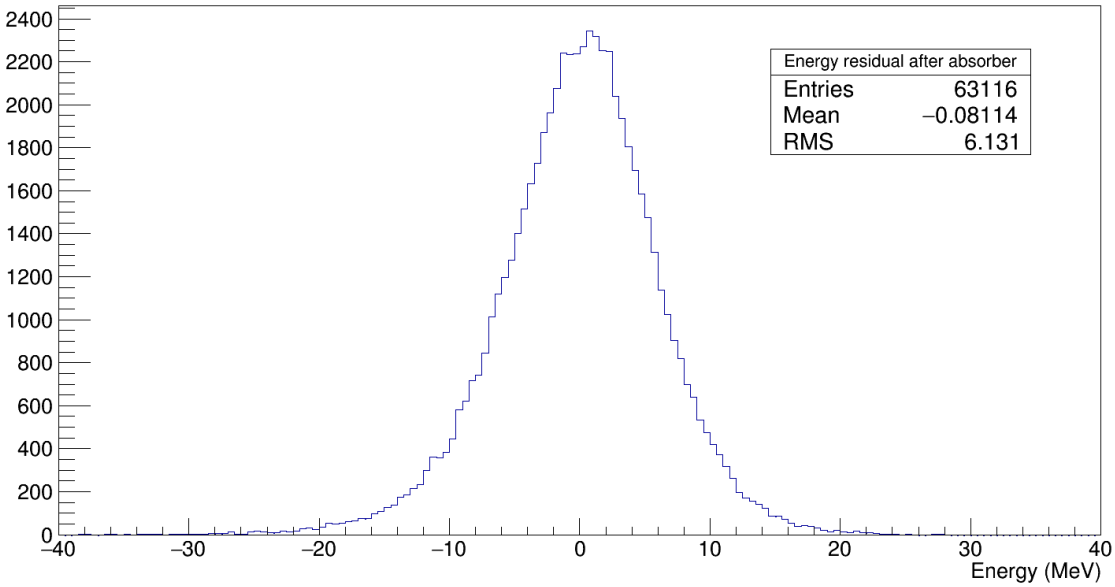

Figure 5.29: Residual between the monte carlo truth energy, and the energy reconstructed from time-of-flight data of muons just downstream of the absorber.

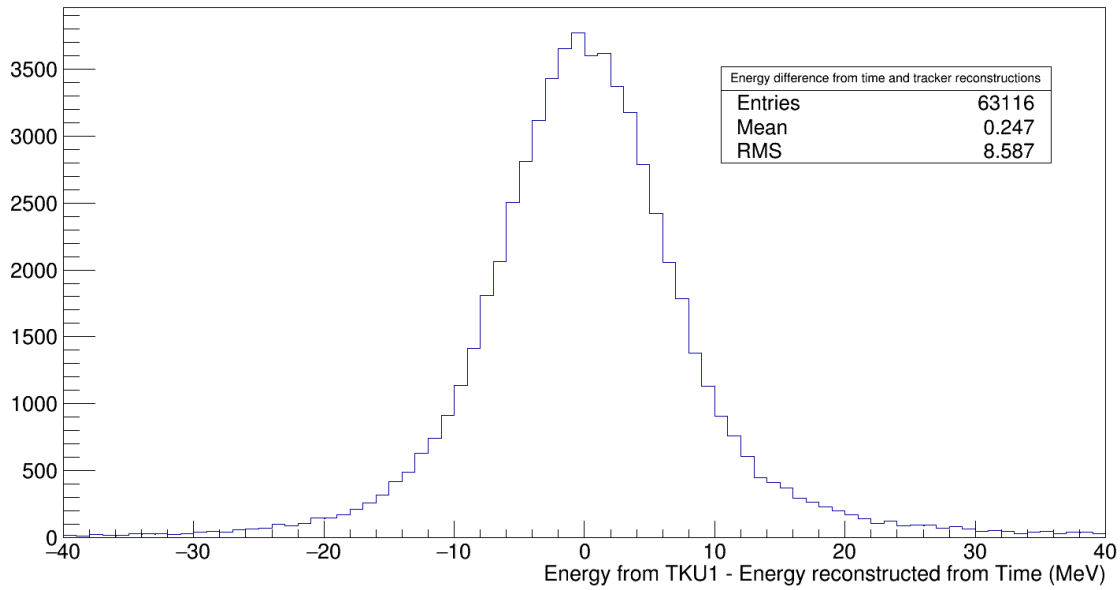

Figure 5.30: Difference between the reconstructed muon energy before absorber. The tracker contribution is measured at TKU plane 5, and the time contribution is measured close to the absorber.

data were in agreement with the truth data. In both plots, although there is an offset on the mean, this in both cases is smaller than the error on the mean, and therefore we can consider this an agreement.

The energy loss for an empty data set measured from TOF data is shown in figure 5.32, and compared to the simulated truth data in figure 5.33. Comparison of the peaks of the distribution through the fit indicates that they are in good agreement, with the MP of the

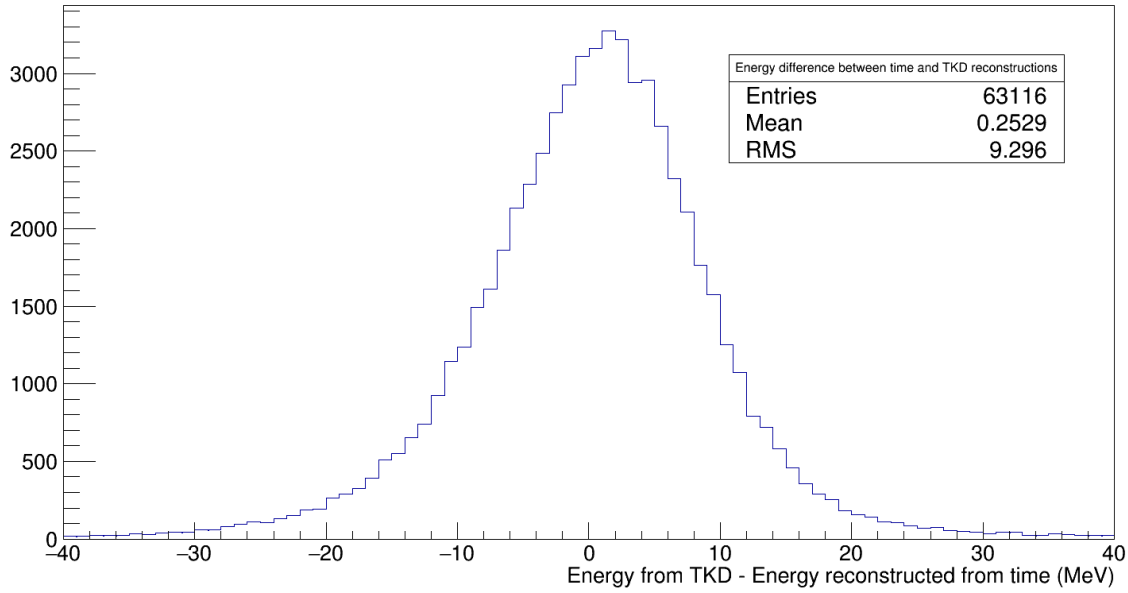

Figure 5.31: Difference between the reconstructed muon energy after absorber. The tracker contribution is measured at TKD plane 5, and the time contribution is measured close to the absorber.

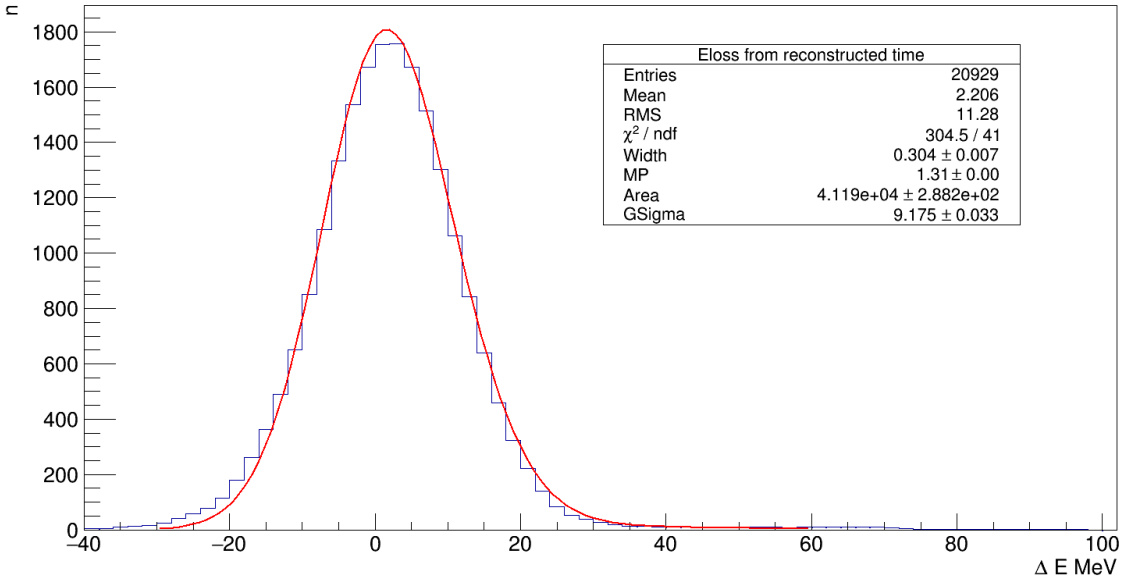

Figure 5.32: Simulated energy loss for empty absorber data reconstructed from TOF data.

TOF reconstructed energy loss measured at 1.31 ± 0.08 MeV.

Comparison between the measurements of energy loss from trackers and TOF data is shown in figure 5.34. The reconstruction from time has a wider peak in this plot, with a greater RMS and the fit is more dominated by the gaussian contribution from detector effects. However, the peaks as discussed before are in agreement, leading to the contribution that both methods are capable of measuring energy loss with an empty absorber.

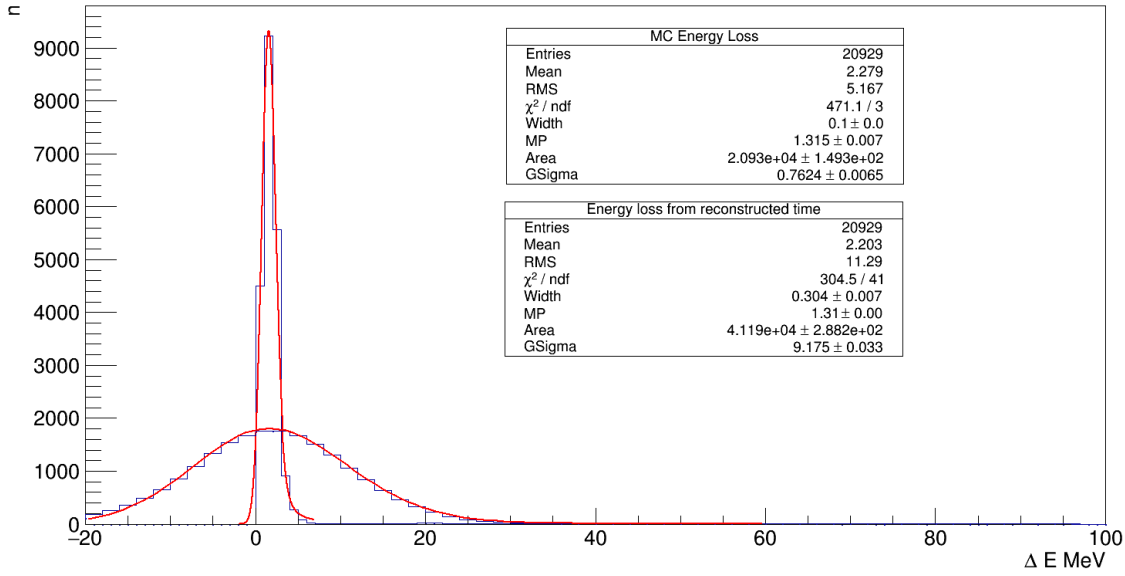

Figure 5.33: Simulated energy loss versus energy loss reconstructed from TOF data for empty absorber data.

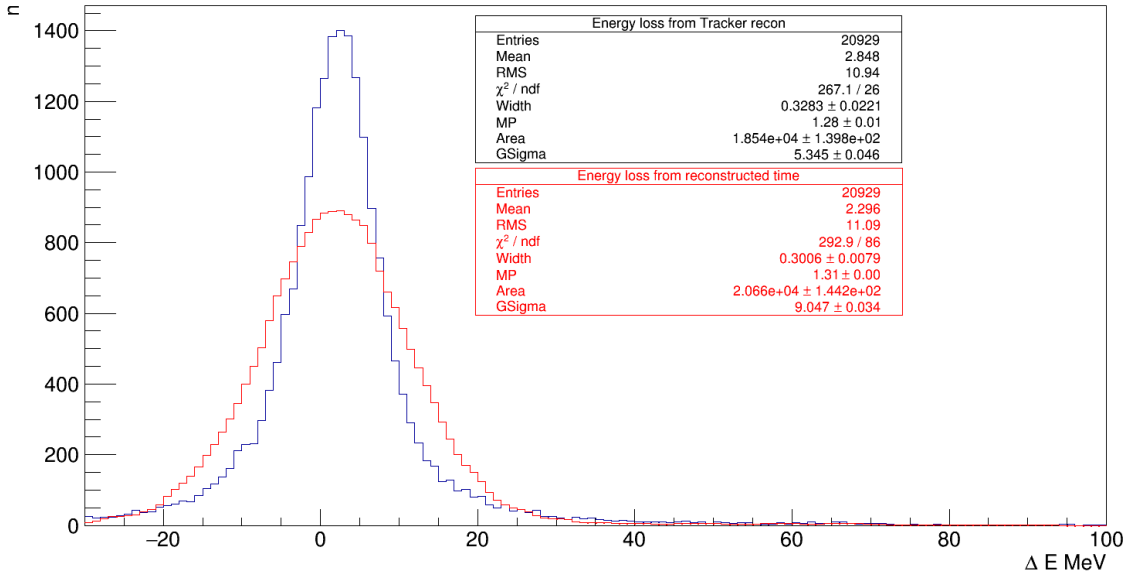

Figure 5.34: Overlaid energy loss distributions for empty absorber data obtained from tracker reconstruction and TOF reconstruction overlaid.

5.7.1 LiH Simulation data

The measured energy loss for LiH data is shown in figure 5.35, and measures a most probable energy loss of 10.39 ± 0.13 MeV. This is again in agreement with the simulated dataset as shown from figure 5.36, which has a most probable energy loss of 10.63 ± 0.001 MeV. This gives a result of the energy loss contribution from LiH of 9.32 ± 0.04

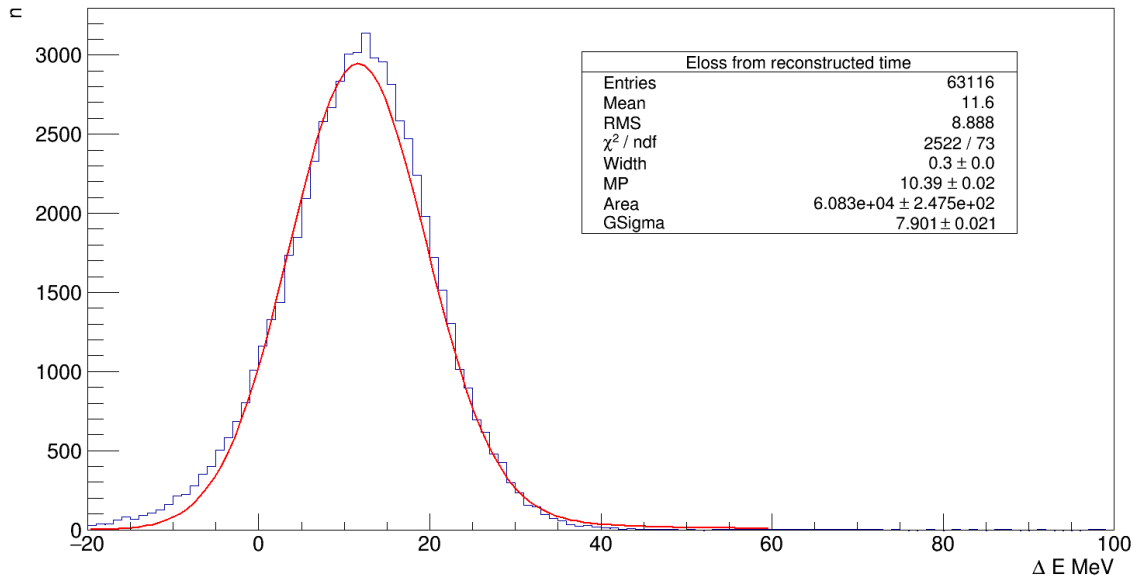

Figure 5.35: Energy loss for Lithium Hydride absorber dataset reconstructed from TOF data.

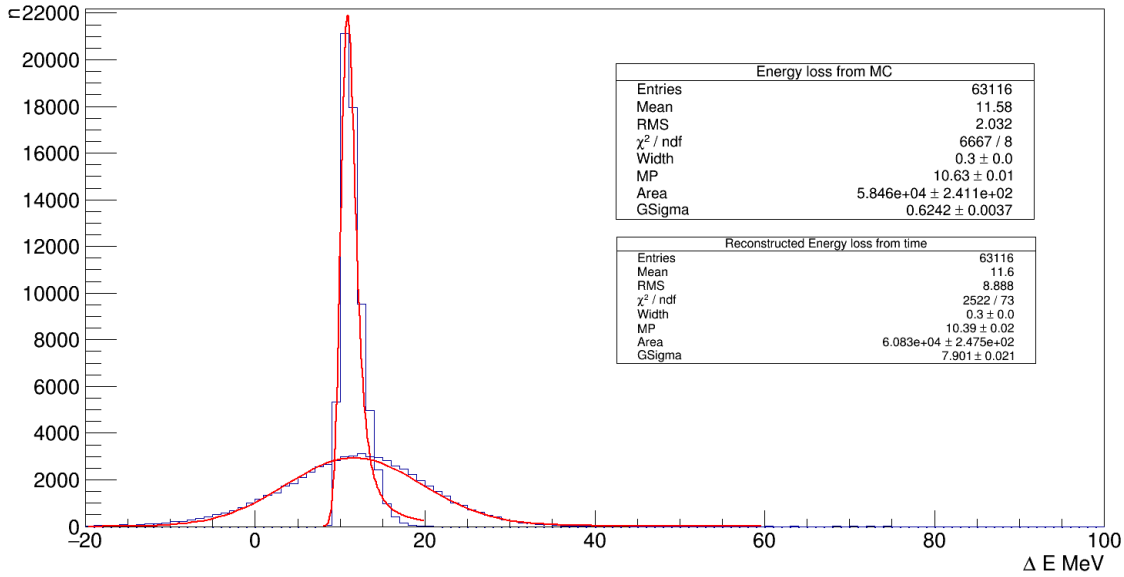

Figure 5.36: Simulated energy loss versus energy loss reconstructed from TOF data for LiH absorber data.

MeV. Finally, the energy loss distributions for LiH data obtained from tracker data are overlaid over figure 5.35 in figure 5.37. This final plot is particularly interesting, as at a glance there is not much difference between the two distributions, and the peaks are in close agreement.

This is a positive result. It confirms that the reconstruction method using TOF data works and is agreement with the tracker data. This means that it will be possible to analyse real data using the TOF method and make a good measurement of the energy loss. This is looked into further in the next chapter/section.

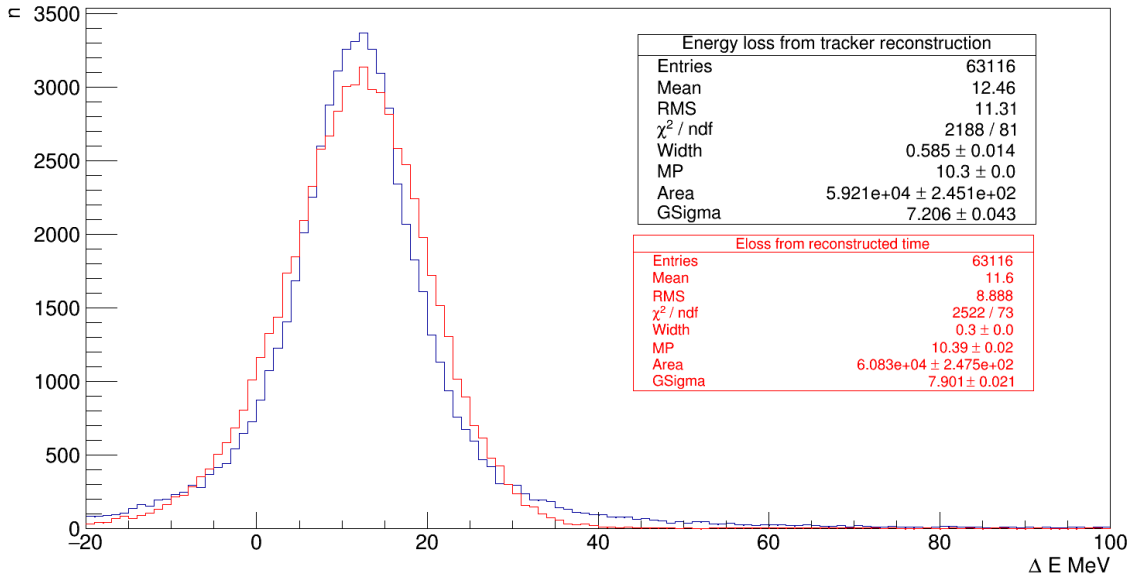

Figure 5.37: Overlaid energy loss distributions from LiH absorber dataset obtained from tracker reconstruction and TOF reconstruction.

5.8 Results

Table 5.2 summarises the results obtained from analysing the results of the simulated Step IV dataset. The first column of results is obtained from the most probable energy loss in each distribution, and the second column is obtained from the mean of the distribution. As expected, the mean energy loss is consistently higher than the most probable point. However, once background effects from the empty data set are accounted for by subtracting the empty data from the LiH data, then the difference between the most probable and average energy losses becomes much smaller.

Both methods of reconstructing the energy loss result in a measurement of the most probable energy loss that is in good agreement with the simulated data. Using the tracker reconstruction obtains a result with a difference of 3%, and the TOF reconstruction varies by approximately 2.3%. In both instances the reconstructed energy loss is lower than that seen in the MC data.

An energy loss of around 1.31MeV in the empty absorber is in line with what is expected. Originally it was predicted that energy loss from the Aluminium windows would contribute around 0.7MeV, and energy loss from air would be around 0.6MeV between the trackers.

The widths of the reconstructed energy loss distributions all lay at a range greater than 8MeV. This unfortunately makes it impossible to measure the width of the distribution,

Table 5.2: Results from the simulated Step IV analysis. The first column is the "Most Probable" energy loss, and the second is the average energy loss across the distribution.

		MP ΔE /MeV	Mean ΔE/MeV
Field on measurement MC Truth Data	Empty FC	1.31 ± 0.03	2.28 ± 0.04
	LiH Absorber in FC	10.63 ± 0.01	11.58 ± 0.01
	LiH Absorber corrected	9.32 ± 0.03	9.30 ± 0.04
Field on measurement Reconstructed from Tracker	Empty FC	1.28 ± 0.06	3.17 ± 0.07
	LiH Absorber in FC	10.30 ± 0.04	12.46 ± 0.05
	LiH Absorber corrected	9.02 ± 0.07	9.29 ± 0.09
Field on measurement Reconstructed from TOF data	Empty FC	1.31 ± 0.08	2.20 ± 0.08
	LiH Absorber in FC	10.39 ± 0.13	11.50 ± 0.04
	LiH Absorber corrected	9.32 ± 0.15	9.30 ± 0.09

and make comments on the straggling effects of the absorber.

The results of the simulated energy loss produce measurements for the energy loss that are lower than predicted from both the Bethe and Landau equations studied in chapter 3. The models of scattering and energy loss used in MAUS have previously been shown to produce different values to those obtained from the Bethe equation. And as the purpose of this simulation was to demonstrate the methods of energy loss measurement produced effective results, this is not a concern moving forward to look at real data.

Chapter 6

Energy Loss using Time of Flight

Between December 2015 and March 2016, data on MICE was collected with the absorber section both empty and containing the LiH disk. However, due to the issues with the SSD matching coil, there was no field in the cooling channel for the duration of this run period, as the data was collected with the main purpose of making the field-off scattering measurement of muons inside the absorber. With regards to the energy loss, without fields in the trackers it is not possible to use the trackers to make a direct measurement of the momentum either side of the absorber unit. However, as the energy losses caused by the tracker stations and TOF detectors are understood, it is possible to use the TOF detectors situated either side of the cooling channel to make a measurement of the mean energy loss caused by the absorber. It was sufficient to treat Energy Loss in the trackers as a single process in the center of the tracker, rather than 5 separate losses for each station.

6.1 Method Outline

Measuring the energy loss without any field in the solenoid magnets requires usage of the TOF detectors to reconstruct the velocity of the muon at points before and after the absorber. This method involves the following steps:

- First, the momentum of the muon after TOF1 is reconstructed.
- Using the known energy loss of the tracker planes, the velocity and energy of the muon is calculated at a point just before the absorber.

- Using the velocity of the muon before the absorber, the time taken for the muon to travel from TOF1 to the absorber can be determined.
- This time is then compared to the time-of-flight between TOF1 and TOF2, to get the particle time of flight after the absorber to TOF2.
- Using a recursive method, the velocity of the muon after the absorber can be extrapolated.
- Once the velocities of the muon before and after the absorber are known, their equivalent energies can be calculated, and the energy loss measured.

In the following sections the details of the algorithm are described.

6.1.1 Rayner Reconstruction for Momentum at TOF1

A measurement of the muon momentum at the TOF1 detector can be made using the timing and position information from the TOF detectors. In theory this is a simple measurement, as if the path length and time-of-flight is known from this information, and the path length of the muon between two TOF detectors is equal to the distance between them, then the momentum can simply be obtained from $p/E = s/t$, and the average momentum of the beam would be given as:

$$p(s,t) = \frac{ms/t}{\sqrt{1 - s^2/(ct)^2}} \tag{6.1}$$

The measurement bias can be given by

$$\frac{\Delta p}{p} = \frac{E^2}{m^2}\left(\frac{\Delta s}{s} - \frac{\Delta t}{t}\right) \tag{6.2}$$

What this means is that if the path length of a 200MeV/c momentum muon is underestimated, this will result in the momentum also being underestimated. This wouldn't be an issue if the space between the TOF0 and TOF1 detectors was empty, however there are the 3 quadrupole magnets positioned between them. As the muon traverses these fields, the path length will be increased. This means that in MICE if we used equation 6.1 to find the momentum of a muon, the momentum is on average underestimated by around 5MeV/c.

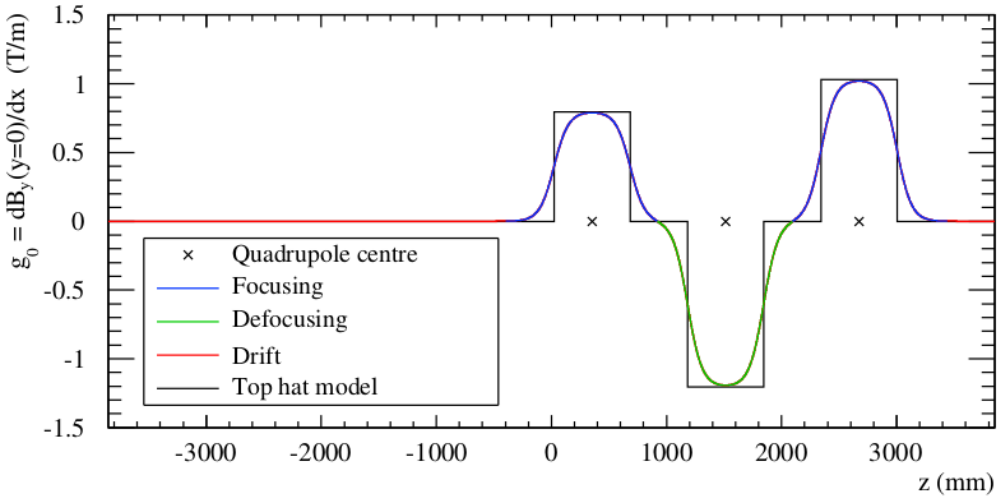

Figure 6.1: The axial quadrupole gradient in Q7, Q8 and Q9 between TOF0 and TOF1. The model used to parametrize the path length of the muon is also illustrated. The width of these top-hat models is equal the effective length of the quadrupoles.[17]

Mark Rayner in his thesis [17] developed a better reconstruction for the momentum at TOF1 by building additional iterative algorithms into the reconstruction to correct for the change in path length caused by the quadrupoles. The method involves making an initial estimate of the transverse momenta of the muon at TOF0 using the position of the muon at TOF0 and TOF1, and calculating elements of the transfer matrix of the muon. The muon path is then propagated through each quadrupole to find a path length for a given set of initial parameters x, x', y, y', p_z. After the path length through each quadrupole is calculated, the process is repeated in the next quadupole with a new set of parameters, so that the total path length can be built up. The total path length is then given as:

$$\begin{aligned} L + \delta^{rec} = & D\left(z_0, z_7 - \frac{1}{2}l_{eff}\right) + \left(l_{eff} + \delta_7^{est}\right) \\ & + D\left(z_7 + \frac{1}{2}l_{eff}, z_8 - \frac{1}{2}l_{eff}\right) + \left(l_{eff} + \delta_8^{est}\right) \\ & + D\left(z_8 + \frac{1}{2}l_{eff}, z_9 - \frac{1}{2}l_{eff}\right) + \left(l_{eff} + \delta_9^{est}\right) \\ & + D\left(z_9 + \frac{1}{2}l_{eff}, z_1\right) \end{aligned} \tag{6.3}$$

where z_n is the z-position of the muon at TOF0, Q7, Q8, Q9, and TOF1 depending on the index, δ^{est} is the estimated path correction, and the function $D(x,y)$ gives the distance between x and y. The details of how this result was approached is best described in the thesis of Mark Rayner [17]. The result of this algorithm is that the momentum of muons at

TOF1 can be measured at TOF1 with a resolution of order 3 MeV/c, which is dominated by the 70ps timing resolution of the detectors. Studies were done against monte-carlo data, and showed a good agreement with the simulated momentum in both transverse and longitudinal places, as seen in figures 6.2, 6.3 and 6.4.

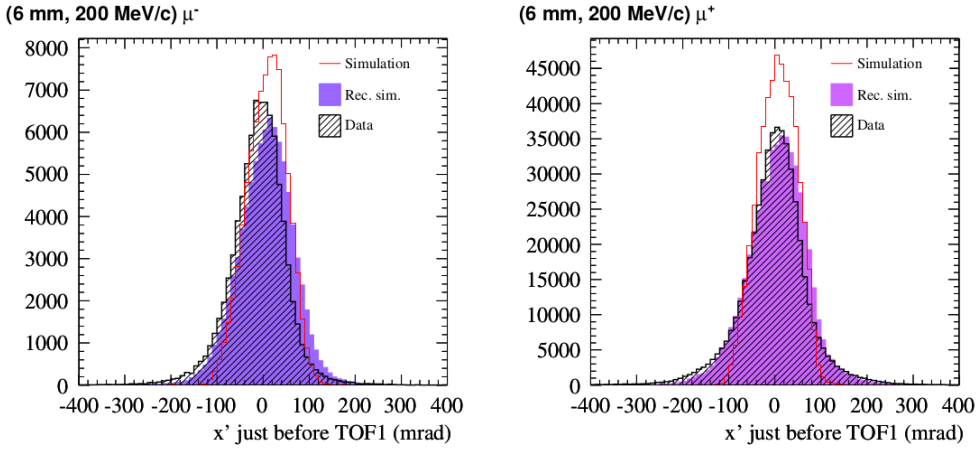

Figure 6.2: Comparison between measurements of x' in data and Step I simulation at TOF 1 for 200MeV/c muons[17]

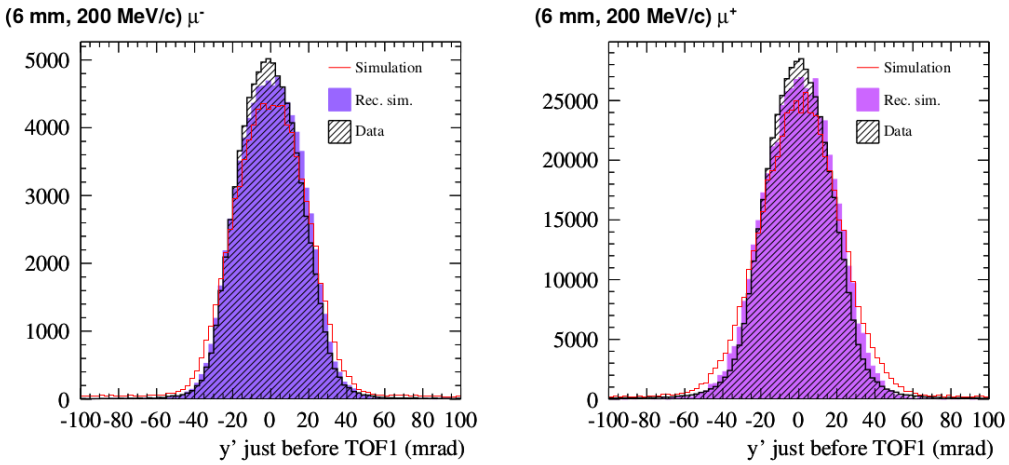

Figure 6.3: Comparison between measurements of y' in data and Step I simulation at TOF 1 for 200MeV/c muons[17]

6.1.2 Delta as a function of Energy Loss

As we are making time-of-flight measurements, it is useful to have an relation between the Energy Loss and the change in velocity of the particle. Consider the expression.

$$\beta = \frac{p}{E} \tag{6.4}$$

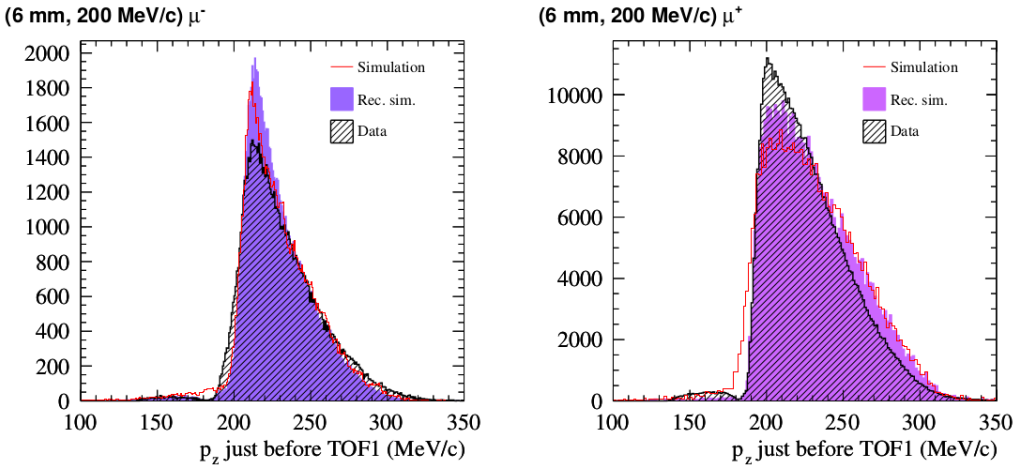

Figure 6.4: Comparison between measurements of z' in data and Step I simulation at TOF 1 for 200MeV/c muons[17]

this can be differentiated via the quotient rule to give

$$\frac{d\beta}{dE} = \frac{\frac{dp}{dE}E - p \times 1}{E^2} \tag{6.5}$$

$\frac{dp}{dE}$ can be resolved by using

$$p^2 = E^2 - m^2 \tag{6.6}$$

$$\frac{dp}{dE} = \frac{E}{p} \tag{6.7}$$

thus

$$\frac{d\beta}{dE} = \frac{E^2 - p^2}{pE^2} \tag{6.8}$$

$$d\beta = \frac{m^2}{pE^2}dE \tag{6.9}$$

$$\frac{d\beta}{\beta} = \frac{m^2}{pE^2}\frac{dE}{\beta} \tag{6.10}$$

$$\frac{d\beta}{\beta} = \frac{m^2}{pE^2}\frac{E}{p}dE \tag{6.11}$$

$$\frac{d\beta}{\beta} = \frac{m^2}{p^2}\frac{dE}{E} \tag{6.12}$$

or

$$\frac{\Delta\beta}{\beta} = \frac{m^2}{p^2}\frac{\Delta E}{E} \tag{6.13}$$

6.1.3 Velocity of Muon before absorber

To measure the energy loss of the muon inside the absorber, we want to know the change in velocity of a muon as it passes through, and therefore the velocity of the particle before and after must be estimated. The velocity of the muon before the absorber can be calculated by making a measurement of the velocity at the start of the cooling channel from the TOF0-1 measurement, then making an estimate of the velocity loss due to the TOF1 detector and TKU tracker stations.

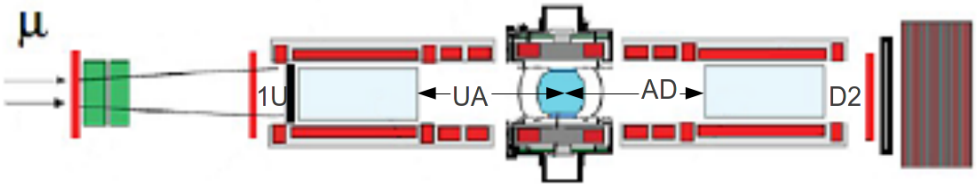

Figure 6.5: Annotated Step IV with the position of the muon in relation to the defined variables used for calculating field-off energy loss.

Its good to define some variables first that are used extensively in the following calculations, and figure 6.5 shows the location of the defined variables on the StepIV layout of MICE.

- t_{01},d_{01},v_{01} refer to the time, distance and velocity of a muon between TOF0 and TOF1. t_{01} is a measured quantity.
- t_{1u},d_{1u},v_{1u} refer to the time, distance and velocity of a muon between TOF1 and the TKU.
- t_{ua},d_{ua},v_{ua} refer to the time, distance and velocity of a muon between TKU and the absorber.
- t_{ad},d_{ad},v_{ad} refer to the time, distance and velocity of a muon between the absorber and TKD.
- t_{d2},d_{d2},v_{d2} refer to the time, distance and velocity of a muon between TKD and TOF2.

- t_{12},d_{12} refer to the time and distance between TOF1 and TOF2. t_{12} is the measurement made.

Firstly, using TOF0 and TOF1 a measurement of the velocity of the muon is made at the point immediately prior to TOF1. This can be adjusted using equation 6.13 by estimating the energy loss of TOF1 as a landau distribution with a peak at 10MeV, as estimated from the material, and putting this energy loss into the equation to get a change in velocity. This gives t_{1u},d_{1u} and v_{1u}. The same process is again followed, this time subtracting the

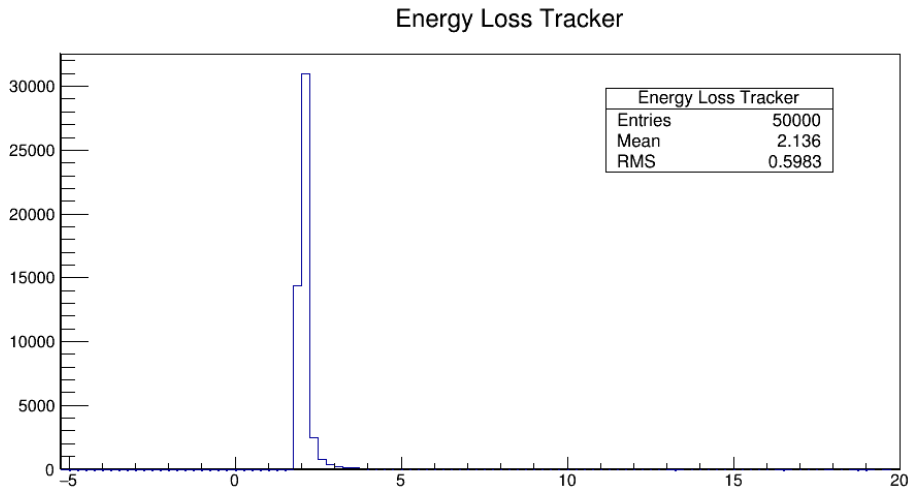

Figure 6.6: Model of overall Energy loss from the Tracker, based on MAUS simulation and data tables.

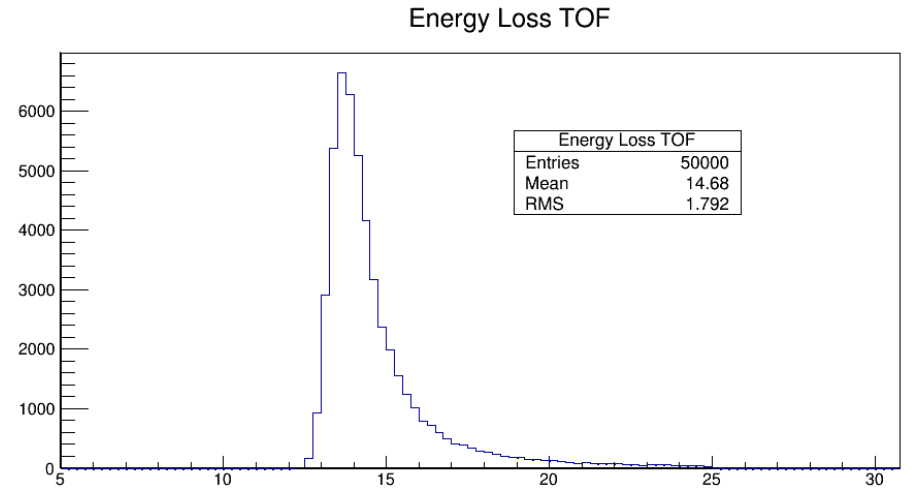

Figure 6.7: Model of overall Energy loss from the TOF, based on MAUS simulation and data tables.

change in velocity caused by energy loss in the TKU stations. This gives the velocity of

the particle before the absorber.

$$v_{ua} = v_{1u} - \beta_{1u}\left(\frac{\Delta E_{tracker}}{E_{1u}}\frac{m^2}{P_{1u}^2}\right) \tag{6.14}$$

6.1.4 Velocity of Muon after Absorber

Estimating the velocity of the Muon after the absorber is more difficult, due to the lack of further TOF detectors either side of the TKD. However the energy loss in TKD is known. Therefore an iterative process was developed to get an estimate for the velocity before the absorber.

Firstly, the average velocity between the absorber and TOF2 can be expressed as:

$$v_{a2} = \frac{d_{a2}}{t_{12} - t_{1u} - t_{ua}} \tag{6.15}$$

And the difference between v_{ad} and v_{d2} is

$$v_{ad} = v_{d2} + \Delta v_{tracker} \tag{6.16}$$

Where $\Delta v_{tracker}$ is obtained from equation 6.13.

If one first uses the measurement of v_a2 as a first guess for v_{ad}, then the energy loss in the absorber will be overestimated, as the average v_a2 is less than the velocity v_ad. However, we can make a condition on the time-of-flight of the particle through the cooling channel.

$$t_{12} - t_{1u} - t_{ua} - t_{ad} - t_{d2} = 0 \tag{6.17}$$

What equation 6.17 says is simply that the measured time between the TOF1 and TOF2 detectors should equal the sum of the estimated time-of-flights between the rest of the stages inside the cooling channel. Therefore, after v_{ad} is first guessed, we use equation 6.16 to get v_{ad} and hence times can be substituted into equation 6.17. If the result is greater than 0 then a new minimum for v_{ad} is defined, and vice versa for a value greater than 0. Then a new value for v_{ad} is defined from the average of the minimum and maximum. This algorithm them converges quickly on a solution for v_{ad}, which can then be compared with v_{ua} to give a solution for the energy loss. Figure 6.8 shows the effect of multiple iterations on the final energy loss measurement.

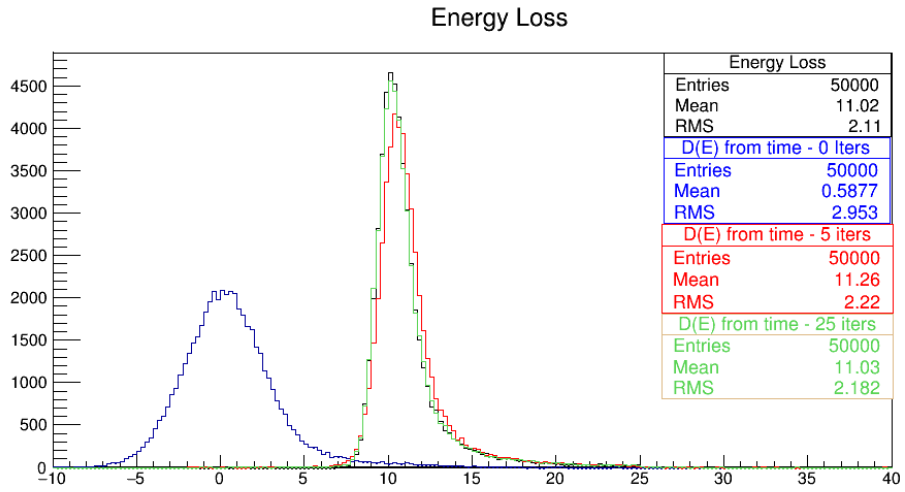

Figure 6.8: Effect on converging on v_{ad} through iteration on the final energy loss measurement. This plot is produced without consideration of the effect of the TOF resolution on the measurement, which is considered later.

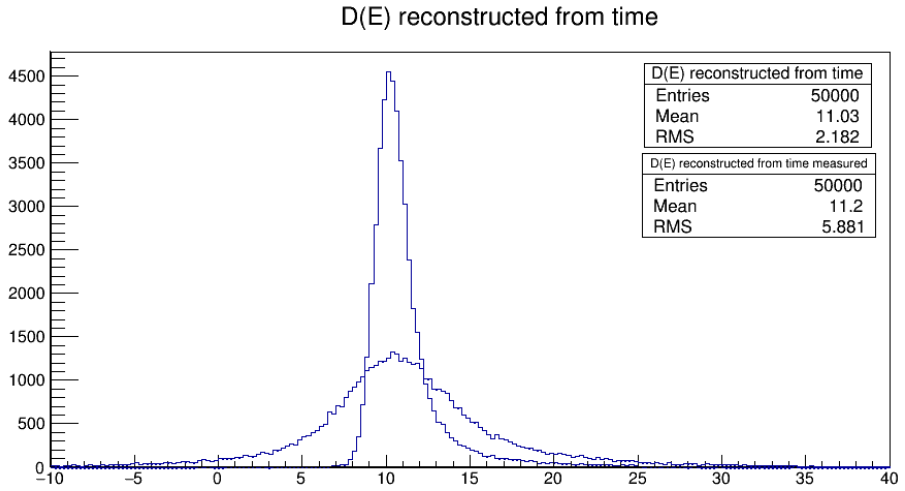

Figure 6.9: Effect of TOF resolution on Energy Loss measurement.

6.1.5 Python Simulation

To test the algorithm, an initial simulation was developed in Python to test different methods of measuring the energy loss from time of flight, using the resolution of the TOF detectors previously measured. This served to demonstrate the theoretical effect that the TOF resolution would have on the Energy Loss measurement. This is simple compared to the MAUS simulations run, but serves to demonstrate the process of the algorithm. Some muons are entered into the simulation with an initial momentum of 220 MeV/c. Energy loss is applied to the muons by subtracting from the momentum a value sampled from a landau distribution with a most-probable value of 10 MeV.

Two sets of data were collected from this simulation. The first set contained the raw values of momenta and energy calculated by the simulation - the ”truth” data. The second set made an initial estimate of how the momentum would be reconstructed at TOF1 by applying a gaussian smear of 3 MeV to the initial momenta, then used the algorithm outlined above to estimate the energy loss in the absorber using the time of flight data only. The results of this are shown in figure 6.9. The RMS of the measured Energy Loss is 5.881 MeV, which will give a statistical error on the mean measurement of 0.026 MeV assuming 50000 events are collected (This error will change depending on the number of events). The most probable point on the distribution can be measured with a low error.

From figure 6.9, it can be seen that the mean energy loss measured is in agreement between the truth values, and the reconstructed time values. Figure 6.10 from this simulation show the differences in the time-of-flight between the absorber and the downstream tracker position for the muons. The resolution of the time-of-flight is very small, in line with the resolution of the TOF detectors. Figures 6.11 and 6.12 show the residual between the reconstructed velocity and time of flight of the muon between the absorber and the downstream tracker. This region is particularly interesting as it is where the downstream energy is reconstructed for the energy loss measurement. In both plots, there is a residual with a mean about zero.

Although the final resolution is measured here at around 5 MeV, this initial simulation was simplistic and did not take into account additional contributions to resolution such as scattering effects and additional straggling inside the trackers. However, these can be best measured with the MAUS simulation, which is discussed next.

6.2 Monte Carlo Studies

As in previous chapters, MAUS was used to simulate the beamline. Muons were generated downstream of the cooling channel before Q7, with such properties that the muon beam in the cooling channel had a 3 mm emittance, and a gaussian distribution of momenta. The fields were configured so that the solenoid magnets were turned off, and there was no field in the Focus Coil. Therefore the only fields affecting the muon beam are the Quadrupole magnets Q7, 8 and 9. The geometry of the simulation used is referred to as version 152 in the configuration database, and represents the latest survey information at the time of running. The simulation was run with 3 different momentum distributions, with means of 170 MeV/c, 200 MeV/c and 240 MeV/c which is representative of the real datasets collected.

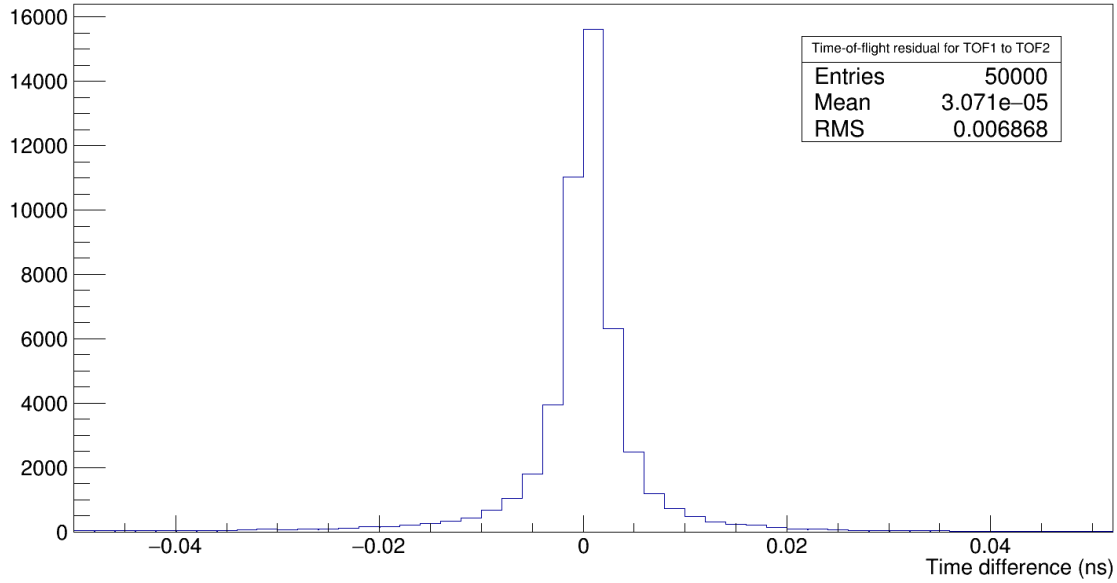

Figure 6.10: Difference between reconstructed and simulated time-of-flight between TOF1 and TOF2.

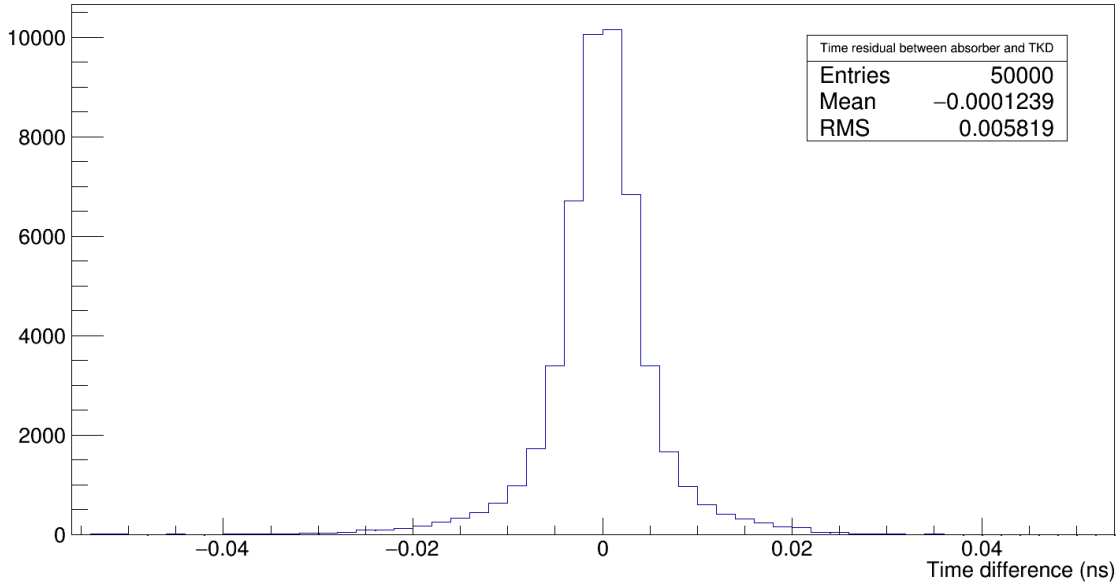

Figure 6.11: Difference between reconstructed and simulated time-of-flight for a muon between the absorber and the downstream tracker.

6.2.1 Cuts on simulated data

Due to the wide distribution of the muon energy loss, it is important when making cuts not to throw away too many events and only make cuts when it is essential. Cuts are made to select muons using timing information between TOF0 and TOF1, where events that have a time-of-flight between TOF0 and TOF1 between 28 and 40ns. It is also required that a hit is recorded in each TOF detector, and each plane of the trackers. This indicates that the particle stayed inside the beam aperture throughout its passage down the cooling

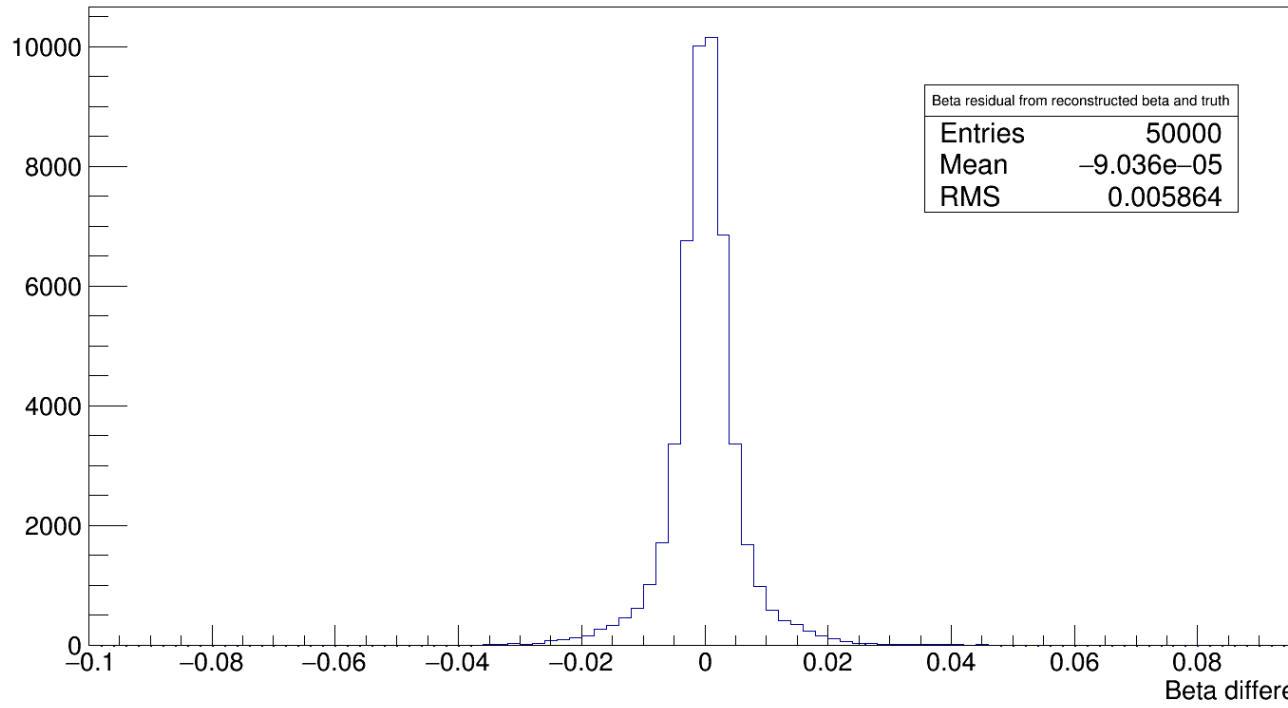

Figure 6.12: Difference between reconstructed and simulated velocity in terms of the relativistic unit beta between the absorber and the downstream tracker.

channel. A further cut is taken in the TKU stations where the distance of the muon from the center of the beam has to be less than 50 mm. This is taken to select muons that are paraxial, and have a small momentum component in the transverse plane.

6.2.2 Uncertainties

As previously discussed, the greatest source of error on this measurement will be the resolution of the detectors. In this instance the TOF performance is what is important. The TOF detectors have a timing resolution of 50/60ps for each detector, which corresponds to a momentum resolution of approximately 2 MeV/c. This is however also subject to reconstruction efficiencies. As shown by the residual plot for momentum reconstructed at TOF1 in figure 6.18, the width of this distribution indicates that the resolution of the momentum at TOF1 is 3.4MeV/c. Note that this is not equal to the expected resolution of the energy before the absorber, as the muon en route to the absorber might suffer different energy losses from detector sources than those predicted. From the python simulation it was estimated that these inaccuracies would lead to a further 4MeV/c contribution to momentum RMS. Equating this to energy, this means that the final resolution on the energy loss from detector and reconstruction should be around 7-8MeV, depending on the

momentum range.

6.2.3 Systematics

Systematic errors in the experiement primarily arise from contributions to the energy loss from sources other than the LiH. These are accounted for by taking a measurement of the energy loss in the cooling channel without the LiH disk, and subtracting this from the measurement with the LiH to obtain the contribution from LiH only.

Using residual plots showing differences between simulated truth-data and reconstructed measurements in the simulation, it is possible to also account for systmatics created by offsets between the reconstructed and true measurements produced mby detectors. As a result the systematic errors are well understood in the measurement and have been corrected for in the final measurement.

6.2.4 TOF time and momentum reconstruction

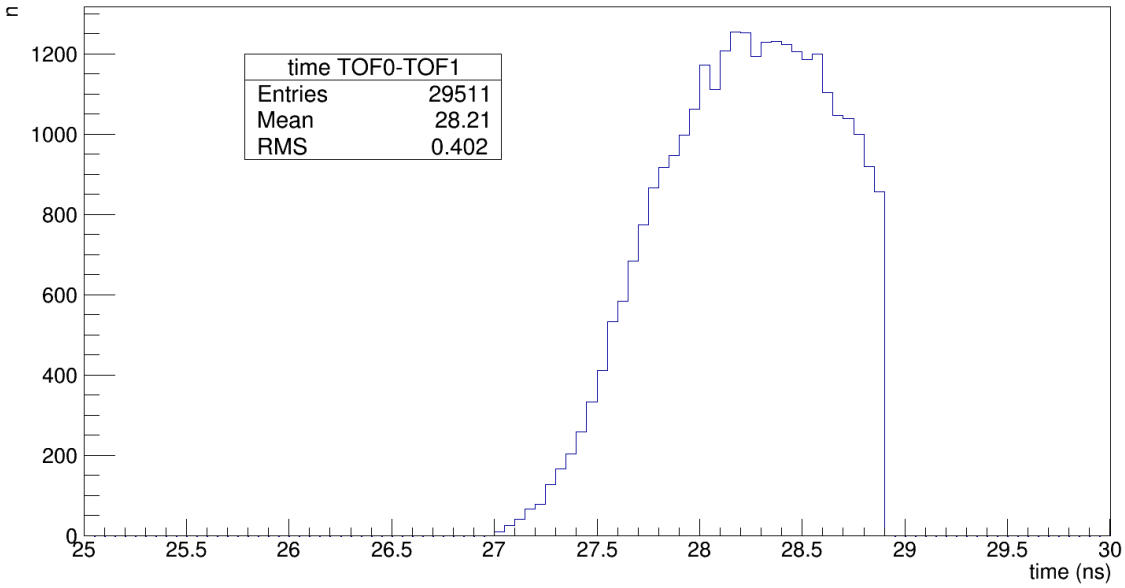

Figure 6.13: Reconstructed time of flight for Muons between TOF0 and TOF1.

The time of flight of muons between the TOF detectors is proportional to the muon momenum as shown below in figure 6.15. This means similar features will be seen when comparing the momentum distribution taken at TOF1 and figure 6.13, and momentum after the absorber and the time between TOF1 and TOF2. Figure 6.13 shows the distribution of the muon time-of-flight between TOF1 and TOF2. There is a cut-off around 29ns where a cut on the data was taken to avoid reconstruction affects shown in figure 6.41.

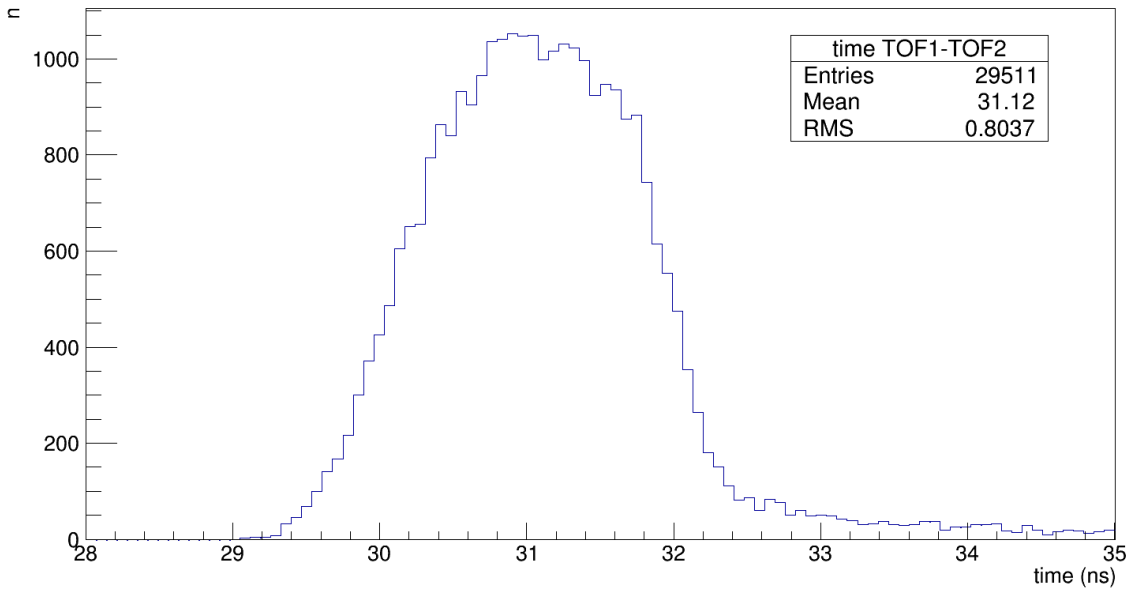

Figure 6.14: Reconstructed time of flight for Muons between TOF1 and TOF2.

However the rest of the distribution shows a gaussian shape.

Looking at the time-of-flight between TOF1 and TOF2 in figure 6.14 the most obvious feature is a tail that extends towards high values of time. It is expected that some muons will suffer more energy loss than others, where they will lose energy through processes other than ionisation energy loss such as scattering and scraping against the beam apertures. We have taken cuts particularly to reduce the number of muons that may have been affected by other sources of energy loss, however some tail due to rare high-energy loss events are not be avoidable. This feature is expected to appear again in the momentum distributions.

6.2.5 TOF reconstruction effects on Energy Loss

In the algorithm, the energy of a muon before the absorber is calculated by finding the muons momentum at TOF1 using the Rayner reconstruction algorithm, and then using an assumed energy loss to make a good prediction of what the energy of the muon might be after it has passed through the TOF1 detector, and the 5 tracker planes in TKU. It is a good check therefore to ensure that there is consistency between these measurements.

Firstly, the momentum reconstructed at TOF1 is calculated using the time-of-flight of the muon recorded between TOF0 and TOF1. Therefore a strong correlation between these two variables is expected.

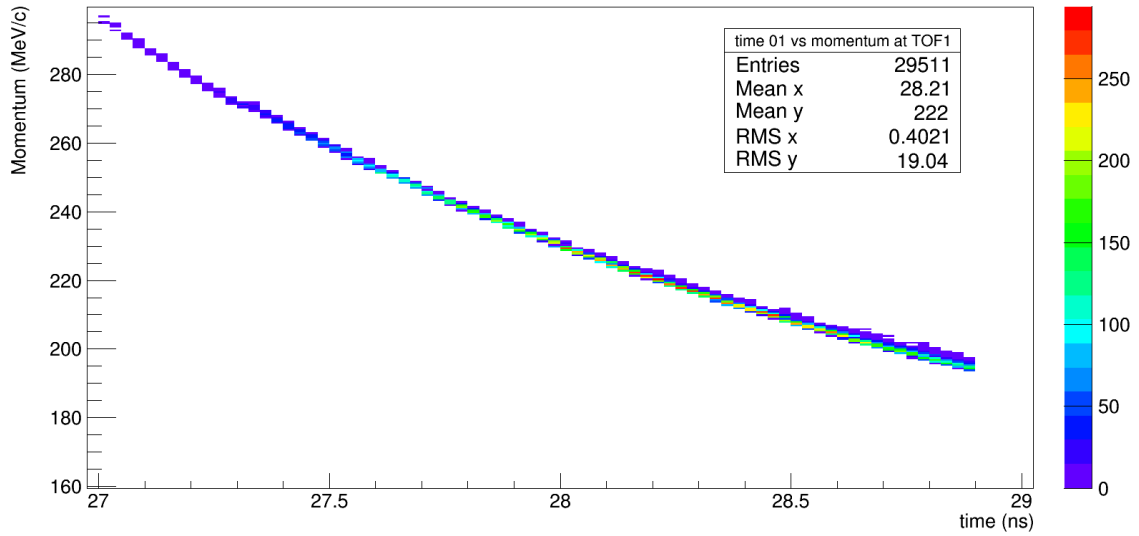

Figure 6.15: Comparison between muon momentum at TOF1 vs reconstructed momentum before the absorber.

In figure 6.15, it is indeed shown that the momentum produced from the reconstruction is related strongly to the time-of-flight. Note that there is not a direct correlation because the Rayner code takes into account the location of the muon at the TOF detectors, and how the path of the muon would have been affected by the quadrupole magnets Q7, Q8 and Q9.

Figure 6.16 shows the relationship between the momentum at TOF1 and the calculated

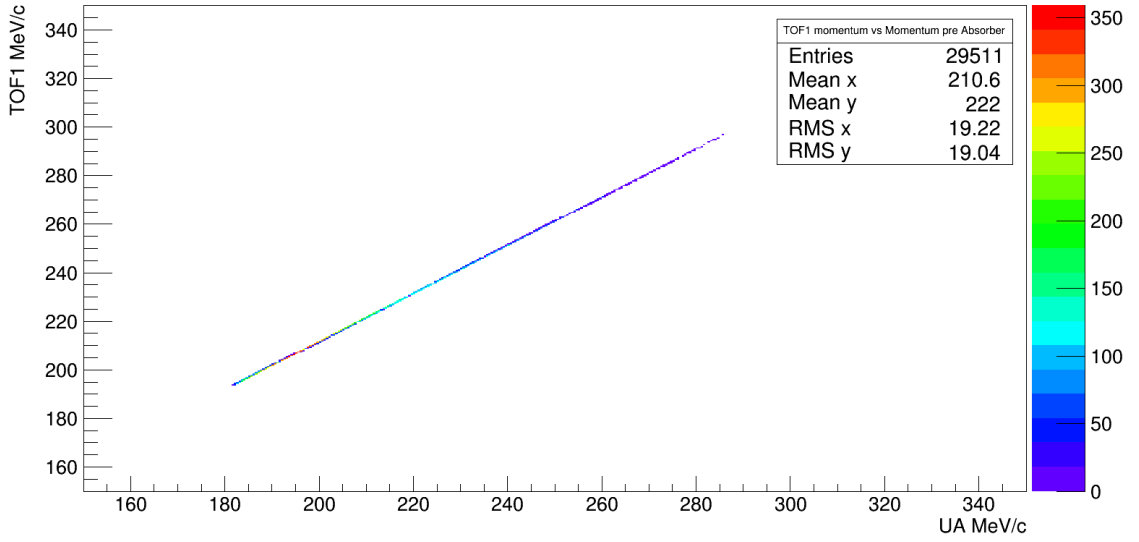

Figure 6.16: Comparison between muon momentum at TOF1 vs reconstructed momentum before the absorber.

momentum before the absorber. Because the energy loss imposed on the muon has a narrow landau distribution, the narrow relationship shown is to be expected.

Figure 6.17 shows the distribution of reconstructed muons just after TOF1, accounting

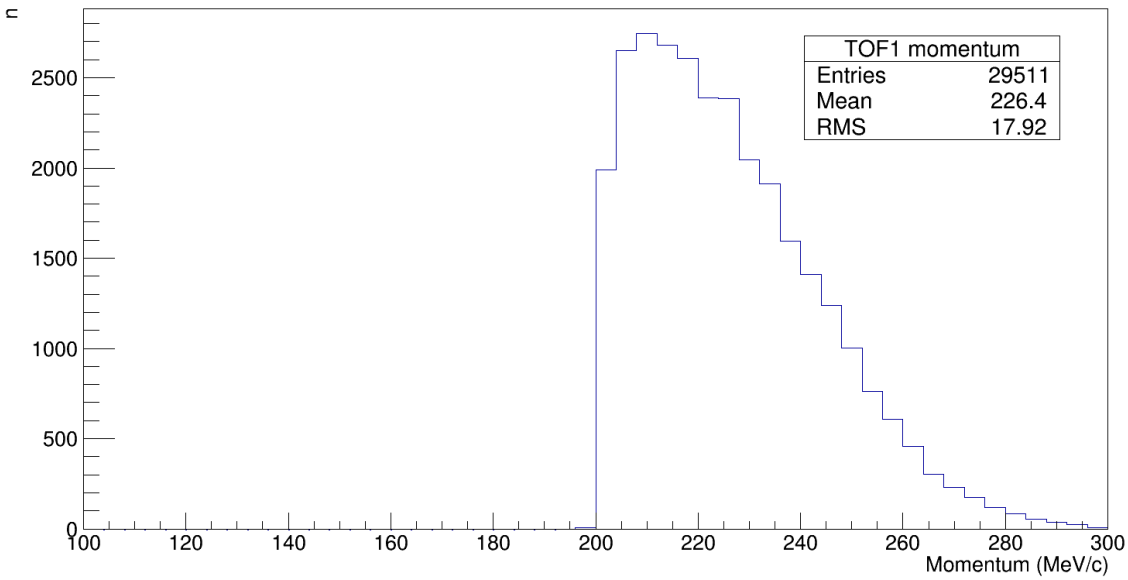

Figure 6.17: Momentum distribution at TOF1.

for the energy loss of the TOF detector of 10.6 MeV. This distribution can be shown to be very similar to the distribution of energy preceding the absorber in figure 6.19. The difference between the reconstructed momentum and the monte carlo true momentum is shown in figure 6.18.

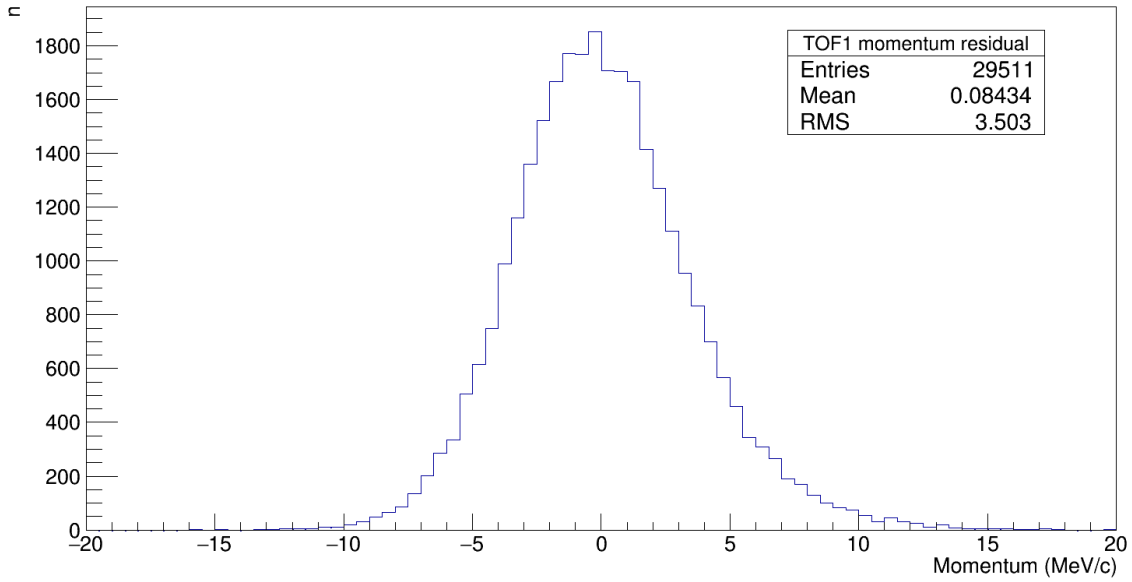

Figure 6.18: Residual between monte carlo and reconstructed momentum at TOF1.

6.2.6 Reconstructed and Simulated Energy Distributions

Throughout the cooling channel, it is generally expected that the shape of the momentum distribution stays the same. Therefore, we expect the reconstructed momentum distributions throughout the cooling channel to be comparable. Figure 6.17 above already shows the reconstructed energy at the TOF1 detector for a 200 MeV/c simulated beam, and acts as a good reference to an expected momentum/energy distribution.

The following plots use data from two sources. One set of plots retrieve the momentum information from the monte-carlo truth data provided by the simulation. The other set of plots get the momentum information from the reconstruction information only, meaning that they use the algorithm for calculating energy from the TOF times described previously. It is also useful to overlay the plots and make a direct comparison of the distributions. Residual plots that show the difference between the reconstructed and MC truth energies have also been produced.

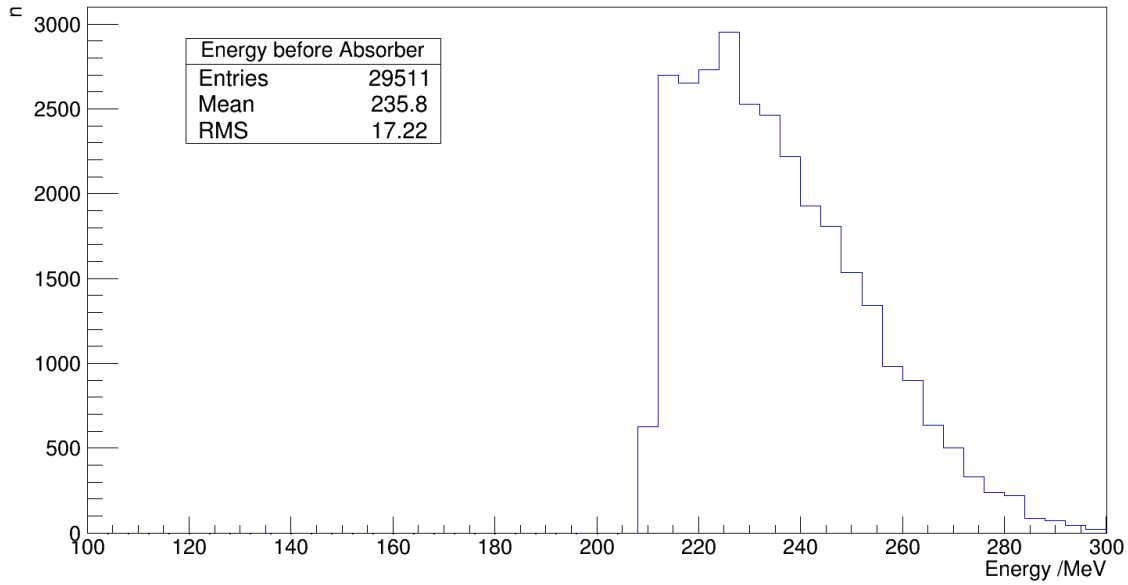

Figure 6.19: Reconstructed Energy distribution before the absorber.

For both the reconstructed data distribution and the MC truth data the distribution matches what is expected when compared with the TOF1 distribution of energy in figure 6.17. This is very much as expected, as before the absorber there are few sources of energy loss that could affect the beam. For example, the planes in the tracker only cause a net energy loss of around 2 MeV. This matches the setup taken with real data, so there is no need to add one, however if the diffuser was in place this would also only have a small effect on the distribution.

Figure 6.22 shows the distribution of differences between the reconstructed muon energy

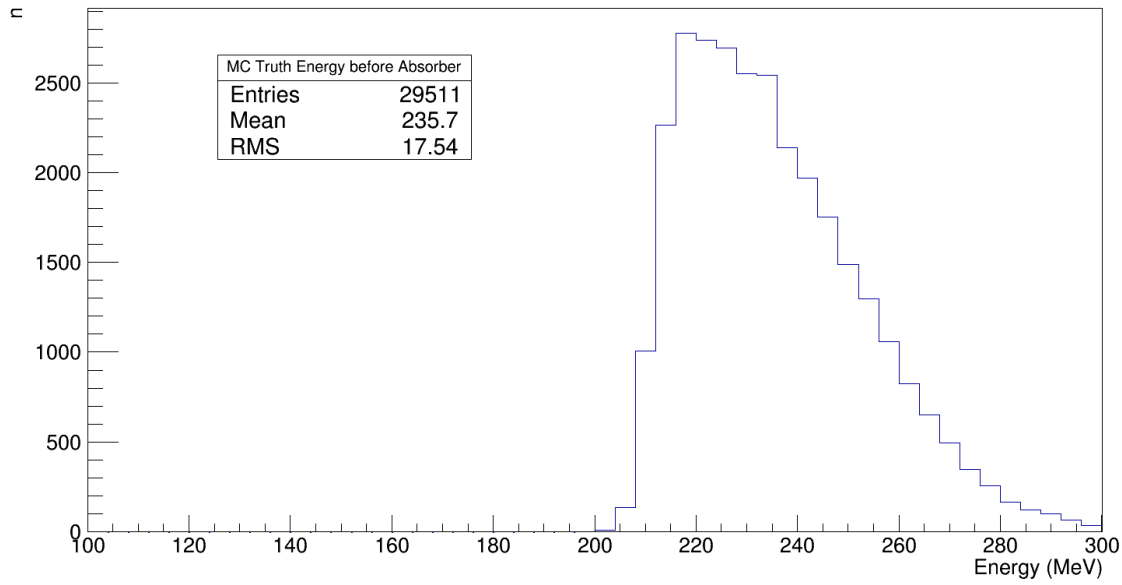

Figure 6.20: Energy distribution obtained from the truth data of simulated muons before the absorber.

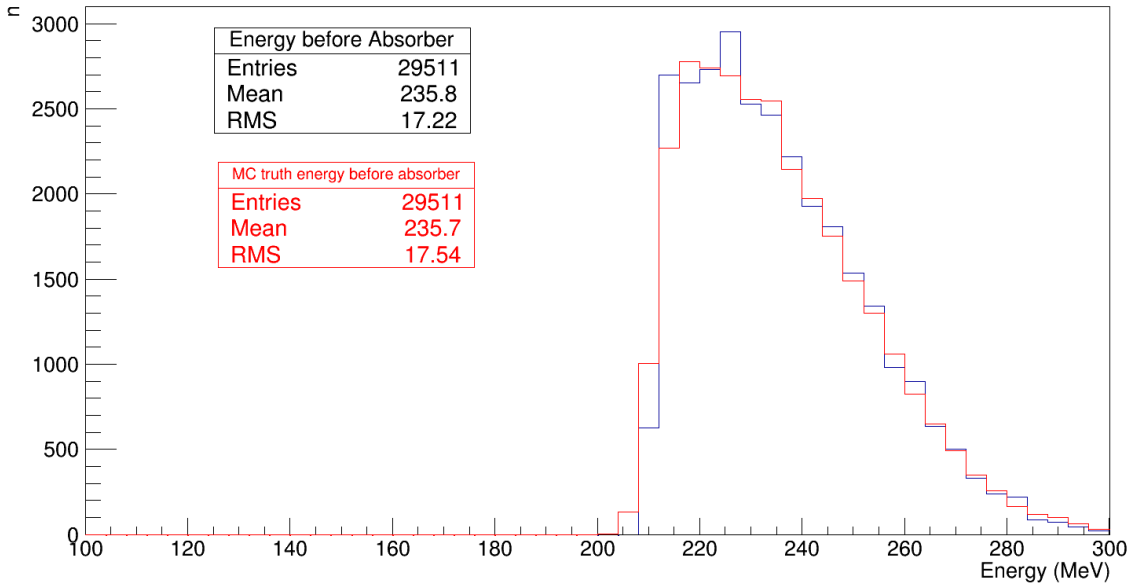

Figure 6.21: Comparison of the energy distribution of MC truth data and reconstructed of muons before the absorber.

and the MC truth data calculated on a particle-by-particle basis. The distribution of the residual has a mean of 0 MeV, which indicates that on average muons before the absorber are reconstructed with the correct energy. There is also a reasonably narrow width on the distribution of 3.5 MeV, indicating good resolution of reconstruction at this point.

An interesting feature of both the reconstructed and monte-carlo energy distributions in figures 6.23 and 6.24 is the tail of muons at energies below 190 MeV. This feature is seen in both the MC and Reconstructed dataset, and is an indication of the number of muons

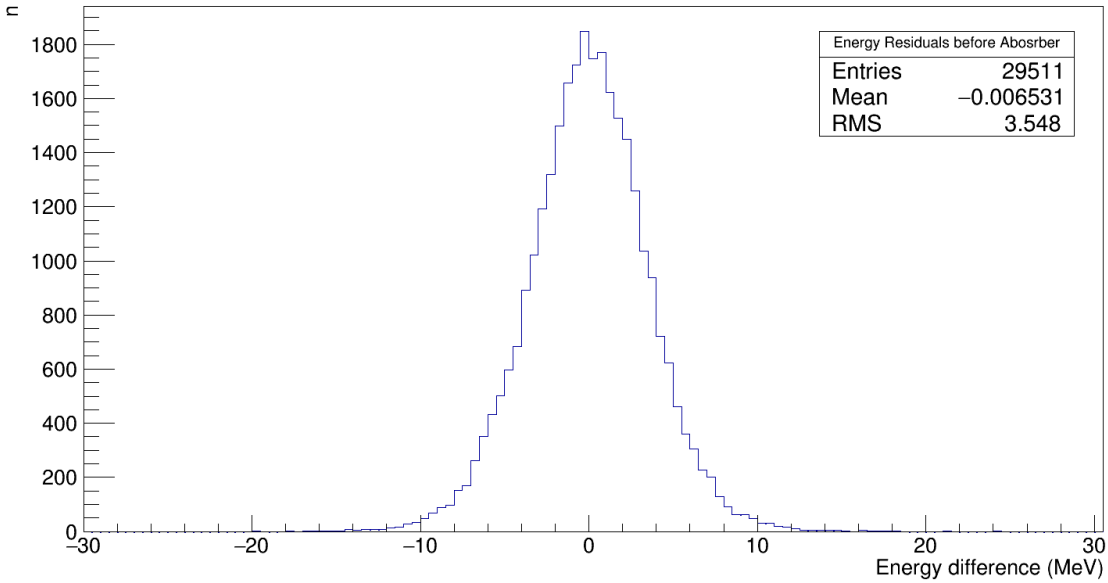

Figure 6.22: Comparison of the energy distribution of MC truth data and reconstructed of muons before the absorber.

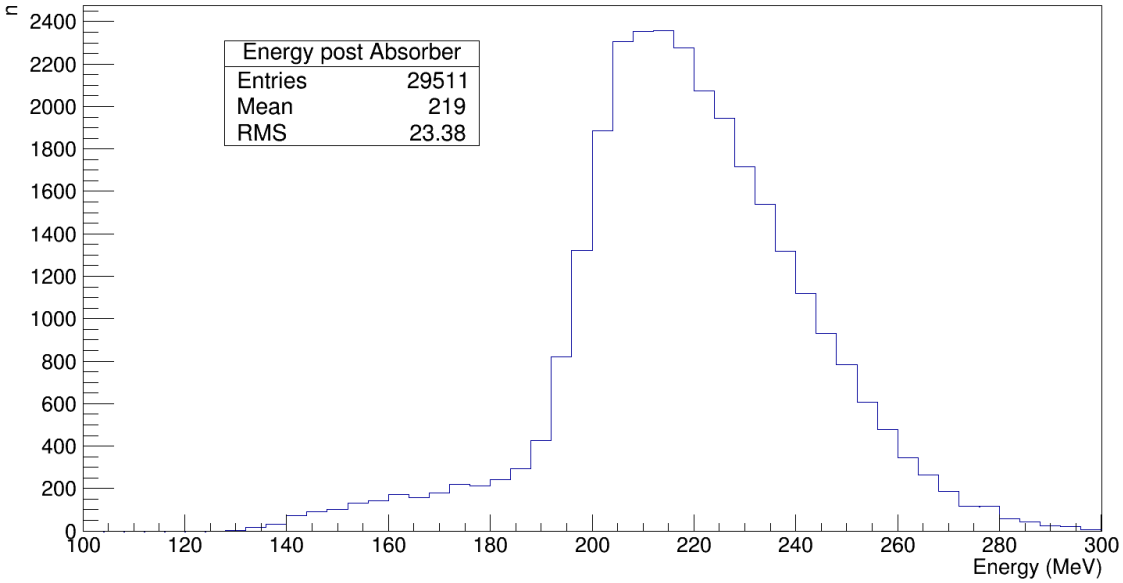

Figure 6.23: Reconstructed Energy distribution after the absorber.

that are losing more energy in the absorber unit due to processes other than ionisation, such as scattering.

In figure 6.25 it is seen that the distributions of energy of muons after the absorber are also in good agreement. The residual plot 6.26 showing the difference between the reconstructed and monte-carlo energies has its mean centred around zero as before. As both residual plots have a mean of zero, this is a good indication that the mean energy loss will also be agreement with simulated data. The width of figure 6.26 is wider than figure 6.22

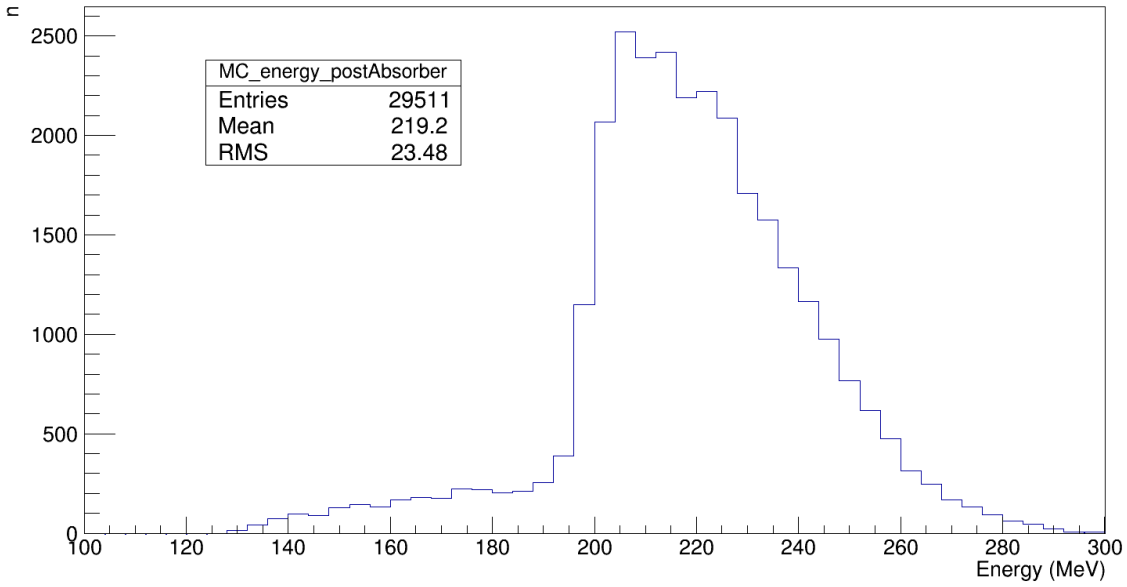

Figure 6.24: Energy distribution obtained from the truth data of simulated muons after the absorber.

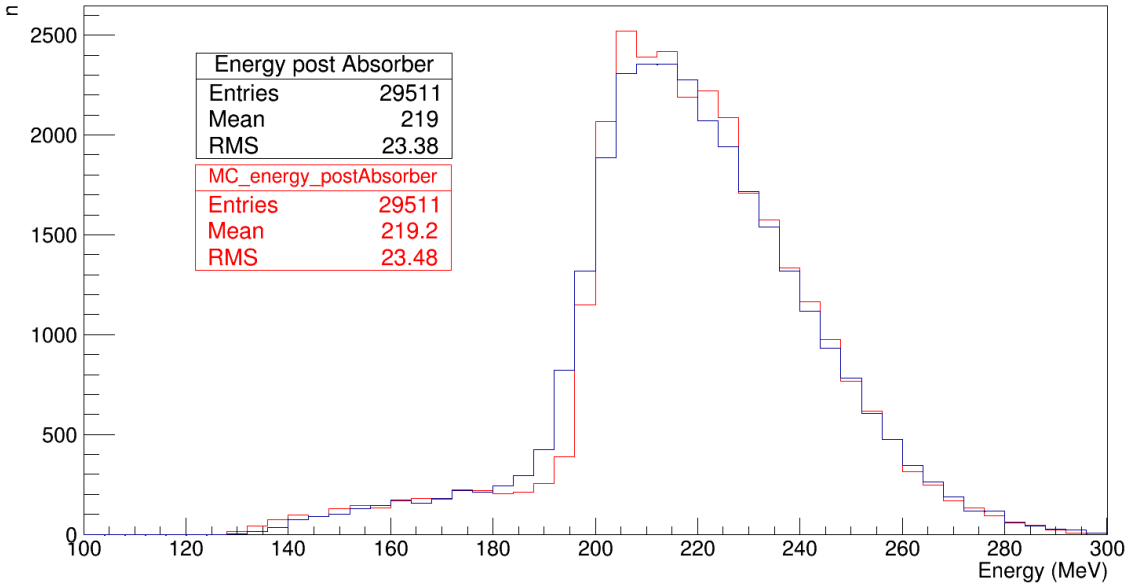

Figure 6.25: Comparison of the energy distribution of MC truth data and reconstructed of muons after the absorber.

with an RMS of 6.3 MeV.

This increased width is to be expected, as due to the nature of the algorithm an overestimate of the energy before the absorber will result in an underestimate of the energy after the absorber to ensure that the muon time-of-flight between TOF1 and TOF2 remains consistent with the measurement taken. Unfortunately there is little that can be done about this, but the resolution remains comparable to that achievable by the tracker detectors at

this energy.

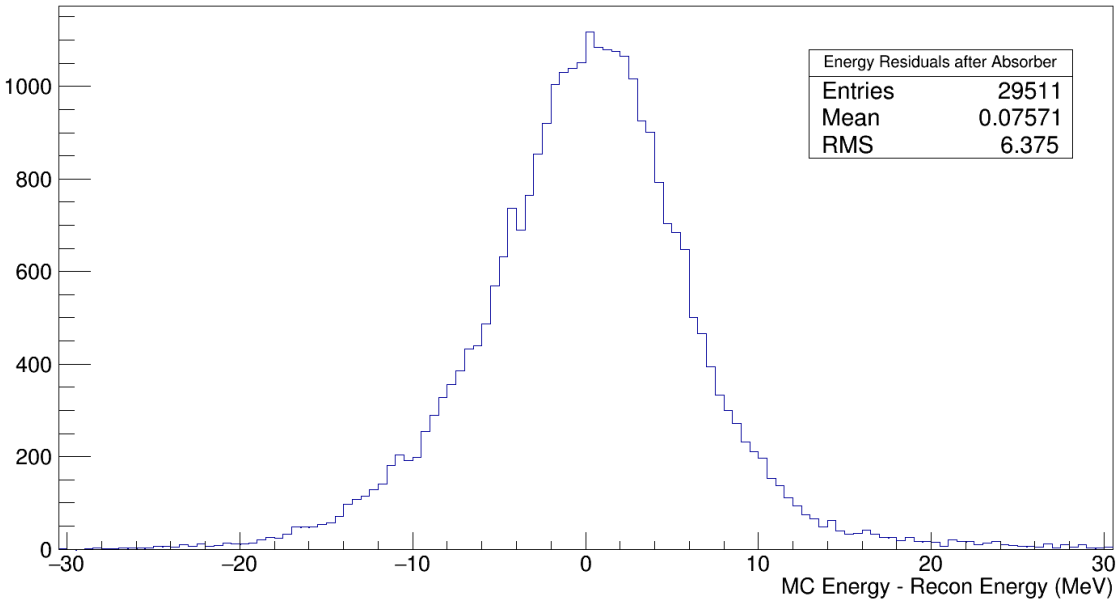

Figure 6.26: Comparison of the energy distribution of MC truth data and reconstructed of muons after the absorber.

6.2.7 Simulated Energy Loss with no Absorber

The first step of the analysis is to look at data simulated without the Lithium Hydride absorber in place, which allows the background contributions to muon energy loss to be measured independently. With the simulated data, it is useful to make additional comparisons between reconstructed data from the TOF information, and the monte-carlo truth data, in order to find resolutions of the measurements at different points.
In figures 6.27 and 6.28 are shown the residuals between reconstructed muon energies and energies obtained from the monte carlo truth data. Both residual distributions have a normal distribution with a mean centred around 0. The width of both distributions is also good, with the resolution before the absorber at 4.78 MeV and after at 6.34 MeV. Notable on the downstream residual are the tails to differences of 20 MeV or more. This will contribute to the tails on the energy loss distributions.

Figure 6.29 shows the energy loss distribution obtained from the MC truth data. This reflects the energy loss of background components as programmed into MAUS. Interestingly there are some muons in the simulation that have a high energy loss of greater than 10 MeV, with a small excess of events with an energy loss of around 20 MeV. In this instance, it is likely that these muons have either hard-scattered from one of the detectors, or the aluminium. They might also have scraped against the solenoid material. However,

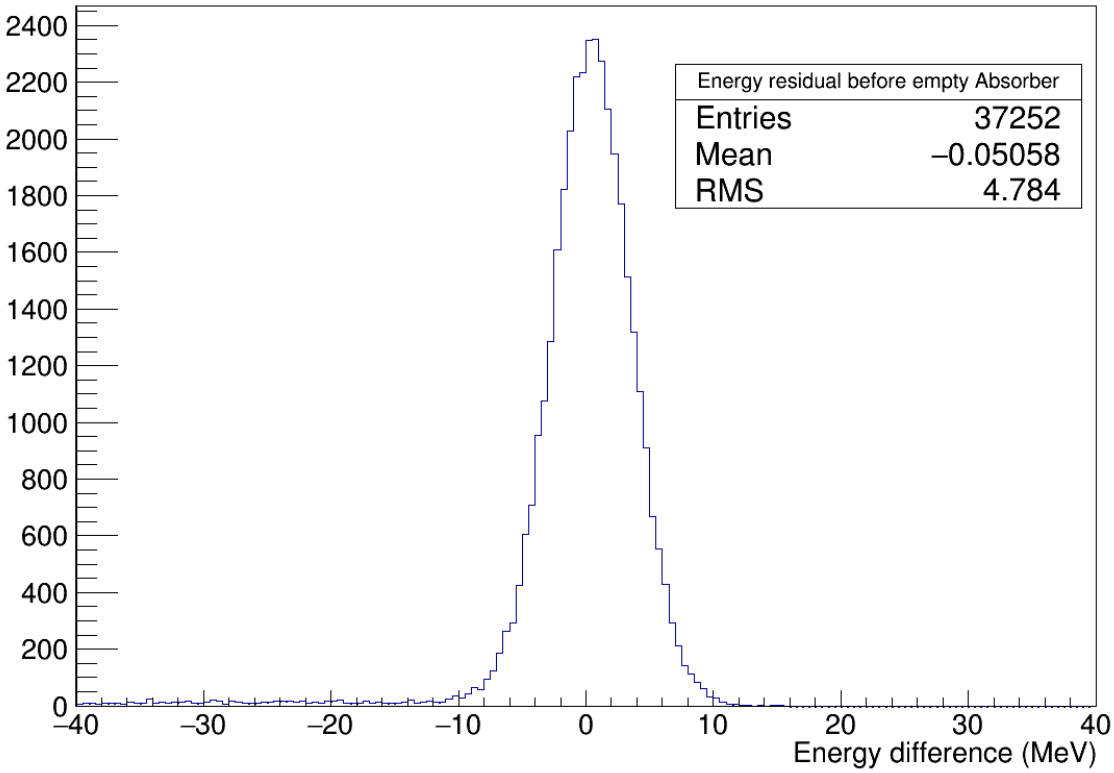

Figure 6.27: Difference between simulated and reconstructed muon energy before absorber for empty set data.

the main region of interest in the distribution remains the peak. The landau-gaussian fit to the peak gives an most probable energy loss of 1.504 ± 0.005 MeV.

The energy loss reconstructed from TOF data for the simulated empty absorber set is shown in figure 6.30. Overlaid with the simulated set in figure 6.31, it is seen that both distributions have an average agreement at the peak, with the most probable energy loss at the reconstructed peak of 1.42 ± 0.01 MeV. The width of the reconstructed dataset is around 8 MeV larger than the simulated data which is a direct result of the reconstruction resolutions of the TOF detectors as shown in the residual plots 6.27 and 6.28.
There is also an immediately apparent tail to large ΔE in figure 6.30. This is a result of the large tails seen in the initial energy distributions to low energy values.
The measurements taken for the empty absorber can now be used later to find the energy loss from only the LiH in the cooling channel.

6.2.8 Simulated Energy Loss in LiH

At this point we have a good understanding of the energy distribution of muons throughout the cooling channel, so the energy loss inside the absorber can be looked at. The

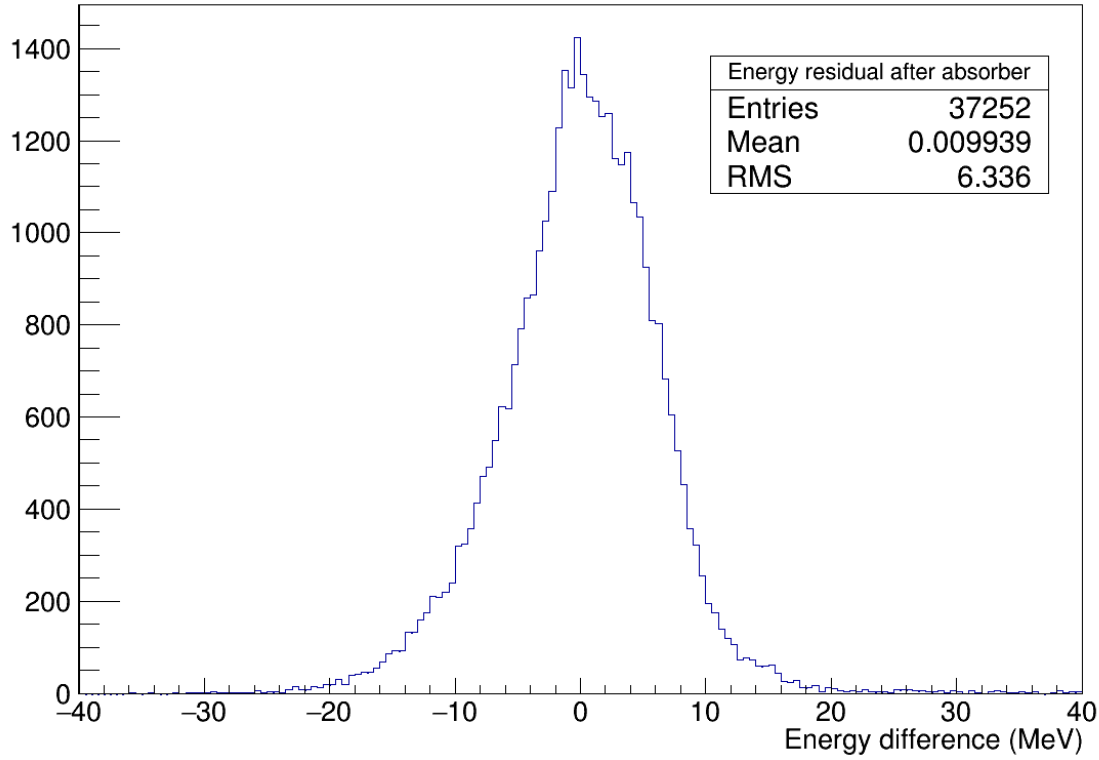

Figure 6.28: Difference between simulated and reconstructed muon energy after absorber for empty set data.

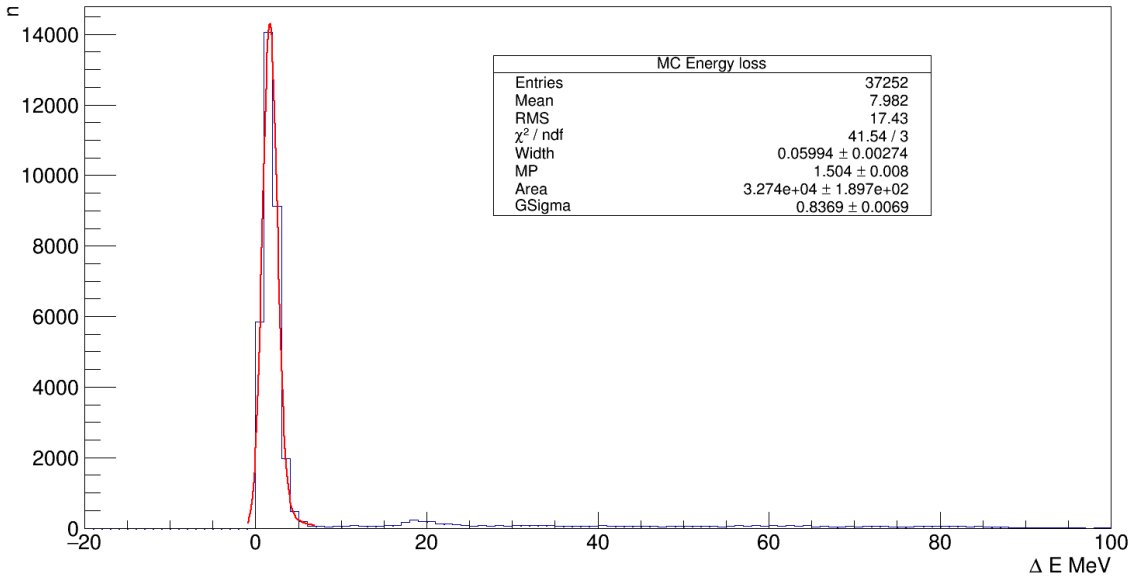

Figure 6.29: Simulated energy loss in the LiH absorber measured from MC truth data either side of the absorber.

energy loss caused on a muon by the absorber is calculated by subtracting the energy of the muon after the absorber from its initial energy, as described previously.

As previously stated, this data is collected from the same simulated 200 MeV/c muon

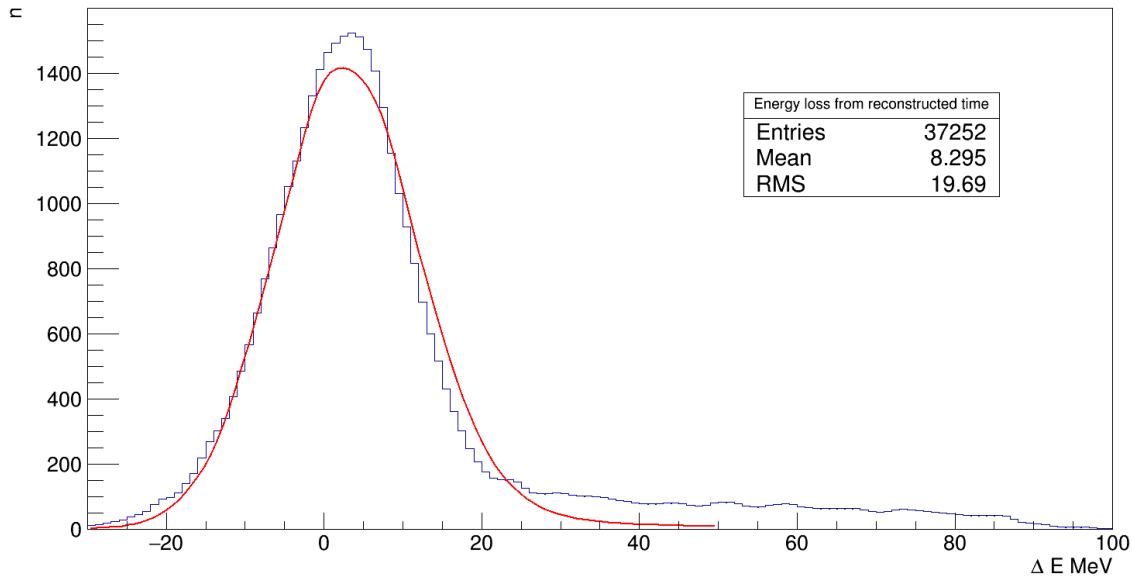

Figure 6.30: Energy loss of simulated muons with no absorber in the cooling channel.

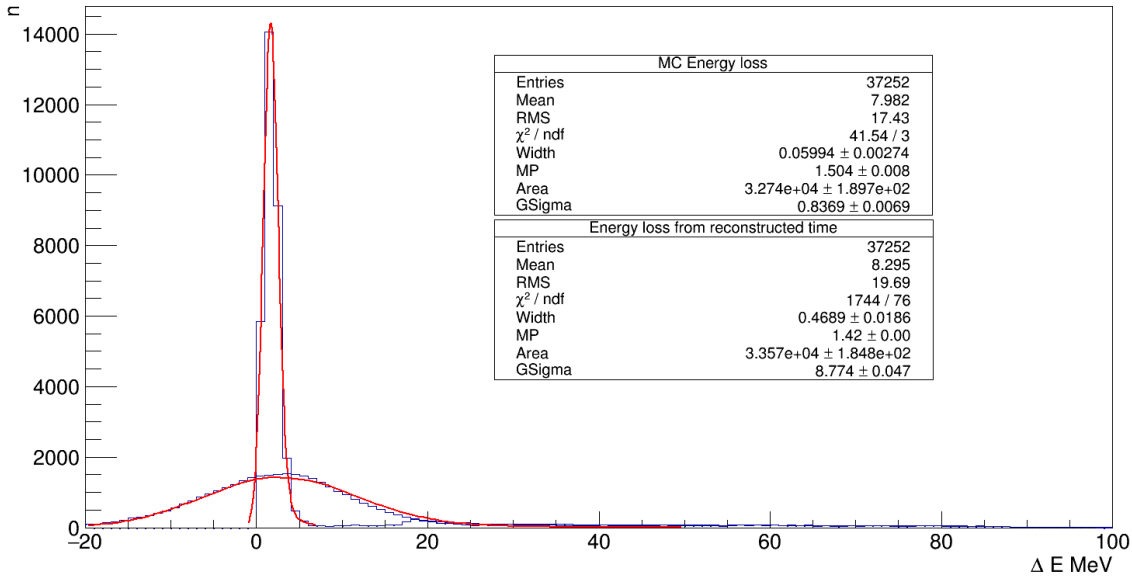

Figure 6.31: Comparison between monte carlo energy loss and energy loss reconstructed from time-of-flight of muons in the cooling channel with no absorber material.

beam data set. Plots are produced using the truth monte-carlo data and the reconstructed data using the TOF information.

Figure 6.32 shows the energy loss seen from the monte-carlo truth data fitted with a convoluted landau-gaussian function. Of particular interest is the parameter ”MP” which represents the most probable energy loss of the distribution. This value represents the most probable energy loss of Lithium Hydride, and represents the most likely energy loss of a muon traversing the material. This value is obtained through the Bethe and Landau

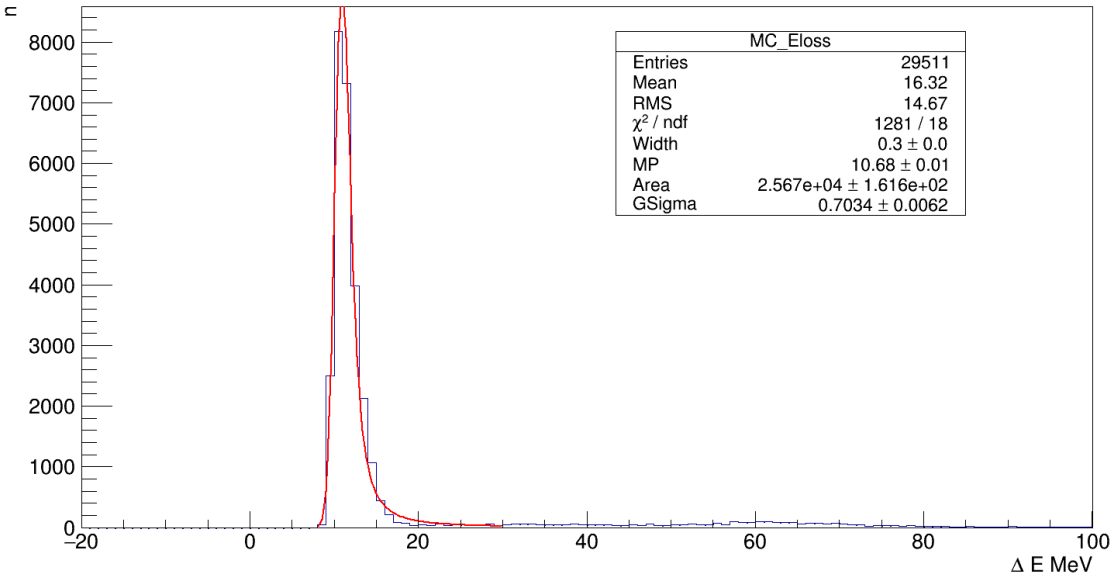

Figure 6.32: Simulated energy loss in the LiH absorber measured from MC truth data either side of the absorber.

equations as described in chapter 4.

We expect that the reconstructed energy loss plot will look as if figure 6.32 was smeared by a further gaussian with a width of the resolution of the energy measurement, which in this instance is 6.5 MeV obtained from the resolution of the energy after the absorber. A similar effect is shown in figure 6.31 with the empty absorber data.

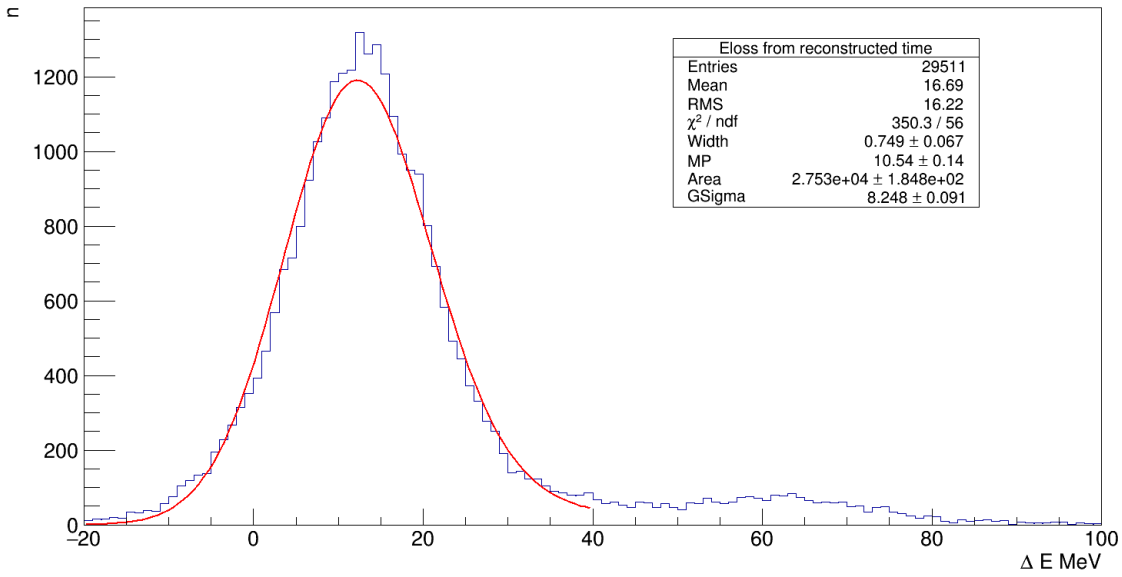

Figure 6.33: Simulated energy loss in the LiH absorber reconstructed from TOF data.

The MP of the landau fit contribution is 10.54MeV $\pm$ 0.04MeV, which is in good agree-

ment to the MP of the monte-carlo plot. This good agreement is further demonstrated when the reconstructed energy loss is overlaid on the monte-carlo plot, as shown in figure 6.34.

In figure 6.34, it is seen that there is a long tail extending to high energy losses in both the monte-carlo and the reconstructed plot. This relates to the tail seen in the energy distributions in figures 6.23 and 6.24. When the plot is adjusted to a logarithmic scale on the y-axis, these tails can be compared. This is shown in figure 6.35. Firstly, it can clearly be seen from this plot that the distinctive Energy loss peak at around 10MeV is smeared on a gaussian to form the shape of the peak seen in the reconstructed energy loss plot. Secondly, the tails are in good agreement and match eachother closely. This is important as it confirms there is not an issue with the reconstruction algorithm in particular that would result in this large tail to high energy loss.

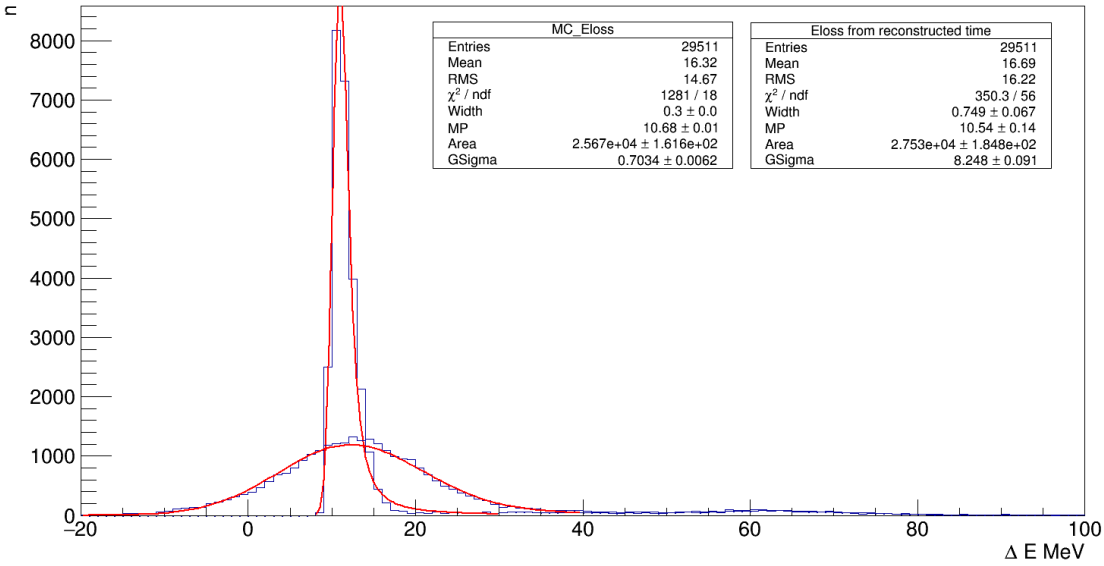

Figure 6.34: Reconstructed energy loss and energy loss from monte carlo truth data.

6.2.9 Energy Loss as a function of Momentum

The energy loss can vary slightly as a function of momentum, as per the Bethe equation in 4.6. Although the range of momenta we can explore using MICE is small, it is nevertheless interesting to investigate this effect.

Figure 6.36 shows the energy loss reconstructed for a 200MeV/c Muon beam against the measured momentum of each muon at TOF1. There is no correlation between the mo-

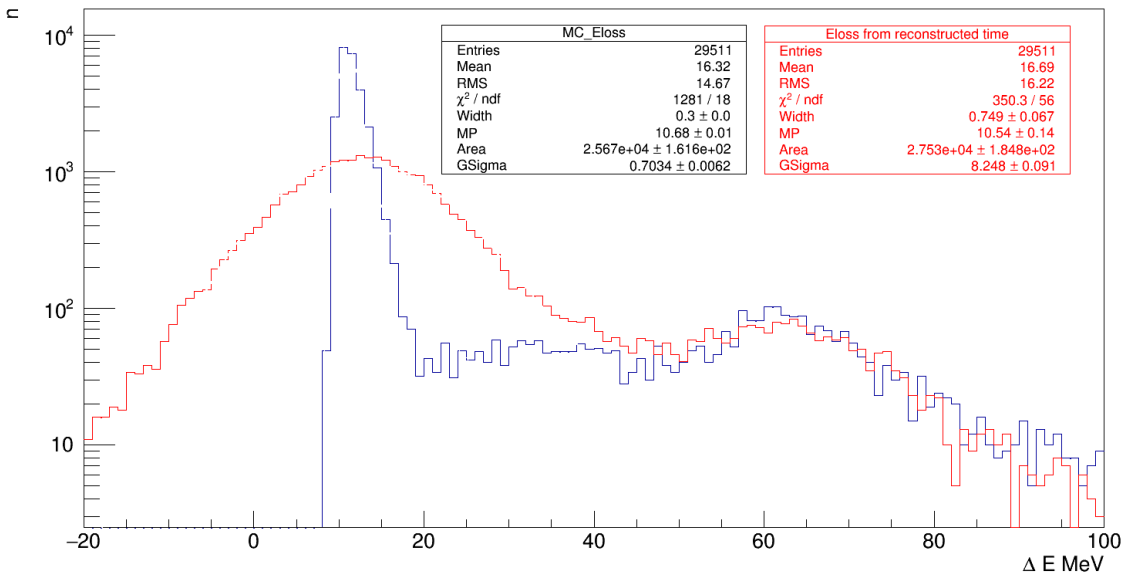

Figure 6.35: Figure 6.34 plotted on logarithmic scale to show similarities in the tail towards high Energy losses.

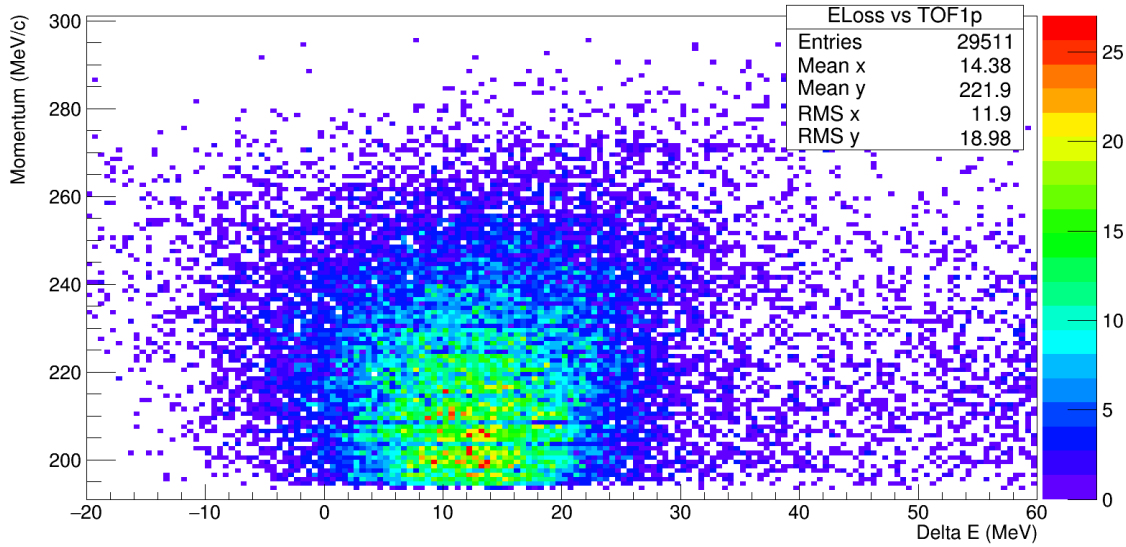

Figure 6.36: Momentum of muons at TOF1 vs the energy loss observed from the absorber.

mentum at TOF1 and excess energy loss, generally the energy loss is focused around a mean of 14.38 MeV as seen in figure 6.33.

6.2.10 Conclusions on monte carlo study

Using a simulation of the MICE experiment, we have shown that using the time reconstruction method developed, it is possible to make a measurement of the average energy loss seen in LiH. This measurement compares well to monte-carlo truth data and therefore

we should feel confident in applying this to data collected from the MICE beamline with no field.

6.3 Real Data

6.3.1 Momentum verification with SSU

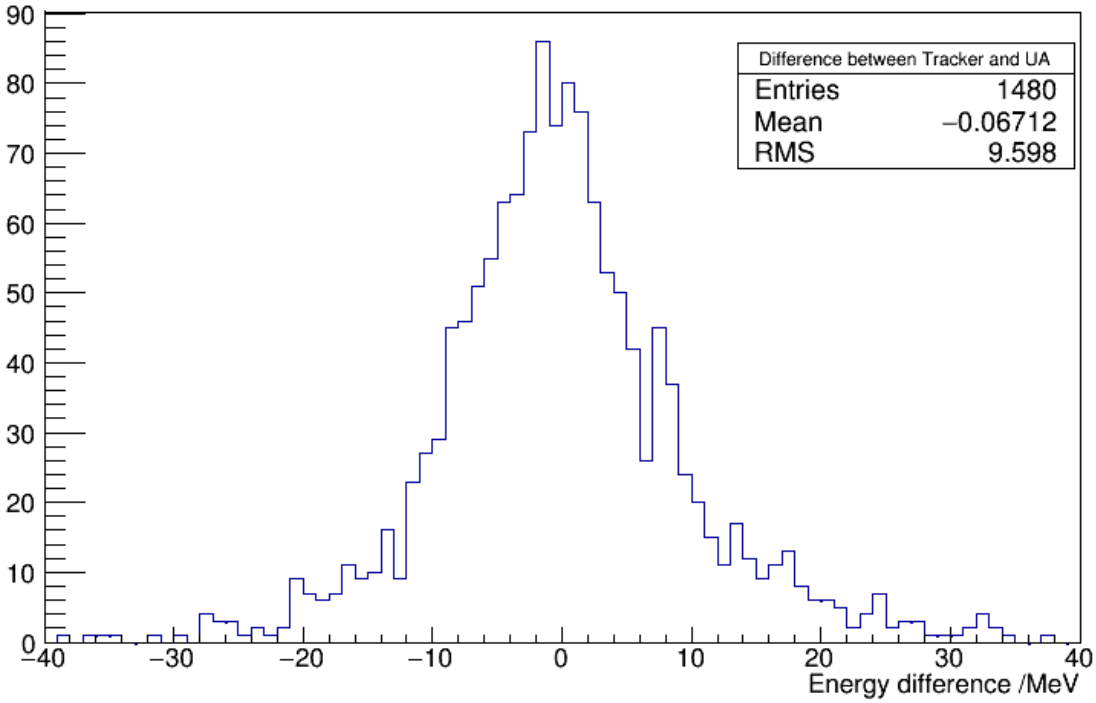

Figure 6.37: Difference between TKU momentum and reconstructed momentum from TOF1 data before absorber.

Data collected in MICE run 07469 contained data with a 4T field in the SSU solenoid, meaning some momentum reconstruction could take place in the upstream tracker. Figure 6.37 shows the difference between the muon momentum reconstructed at the upstream tracker from both the tracker data, and the timing data. The statistics are low as a requirement of the comparison is for muons to reach TOF2, and in this configuration beam inflation was sufficient after the absorber to lose many muons in the downstream part of the cooling channel. The error on the mean is calculated at 0.25MeV, and using this we can state that the calculation from the timing information is in agreement with the momentum reconstructed from the tracker.

6.3.2 Empty Absorber

Some data was initially collected with no absorber in the cooling channel to allow background energy loss sources to be measured, these can later be accounted for to find the contribution from the LiH absorber only. The cuts taken on this data are the same as described in section previous, with the addition of an extra timing cut on TOF1 and momentum cut above 220 MeV to find the most reliably reconstructed muons. This is the same cut that will be used with the LiH data. After the cut, there are only around 8k muons that are accepted by the analysis, however this is enough to find a mean energy loss of the empty absorber.

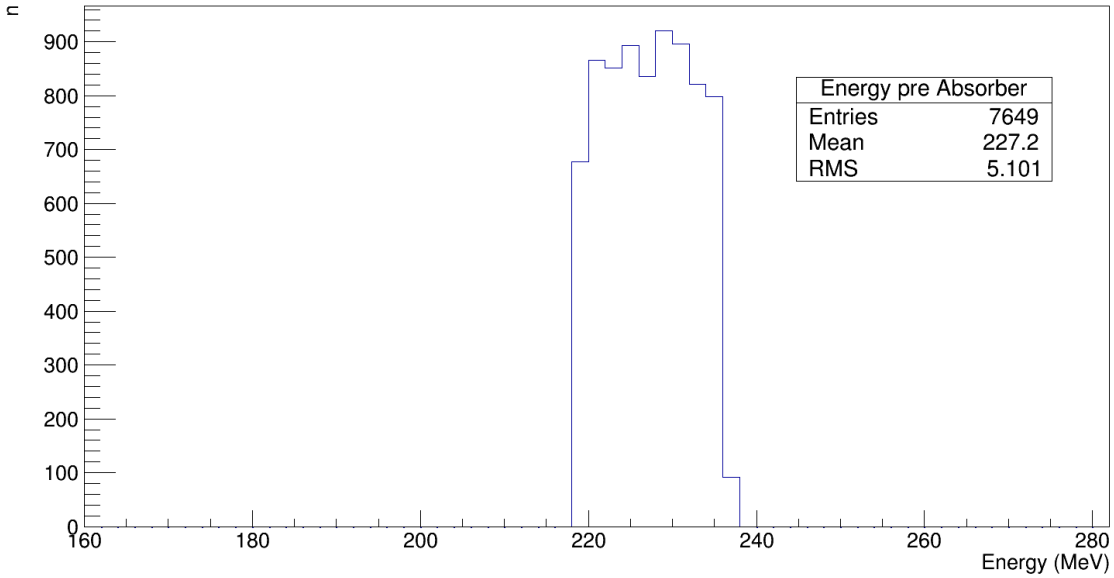

Figure 6.38: Energy of muons reconstructed prior to the absorber.

Figures 6.38 and 6.39 show the distributions of energy for muons reconstructed from TOF data either side of the absorber. Figure 6.38 shows energy before the absorber, and on here the effects of the cuts taken are clearly apparent with slices either side of the distribution. Figure 6.39 shows energy after the absorber. This second plot is clearly effected by the resolution of the detectors, with a much larger RMS of 22 MeV. Furthermore, it shows a tail leading to low energies. Muons that have undergone energy loss processes in the aluminium windows such as scattering will contribute to this tail, and a similar effect can be observed in the simulation.

Figure 6.40 shows the energy loss distribution for muons in the cooling channel with no absorber. Although the mean of the distribution lies at 9.67 ± 2.1 MeV, the peak is the important part of the distribution. Fitting the landau-gaussian convolution to the peak gives an MP landau parameter of 1.12 ± 0.11 MeV. Varying the parameters of the fit was

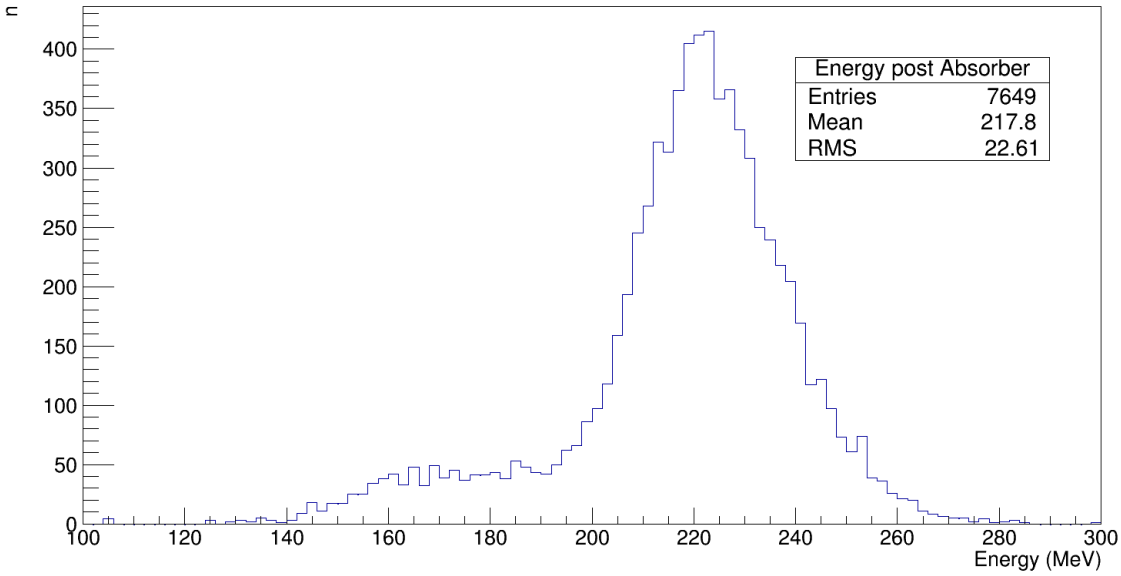

Figure 6.39: Energy of muons reconstructed after to the absorber.

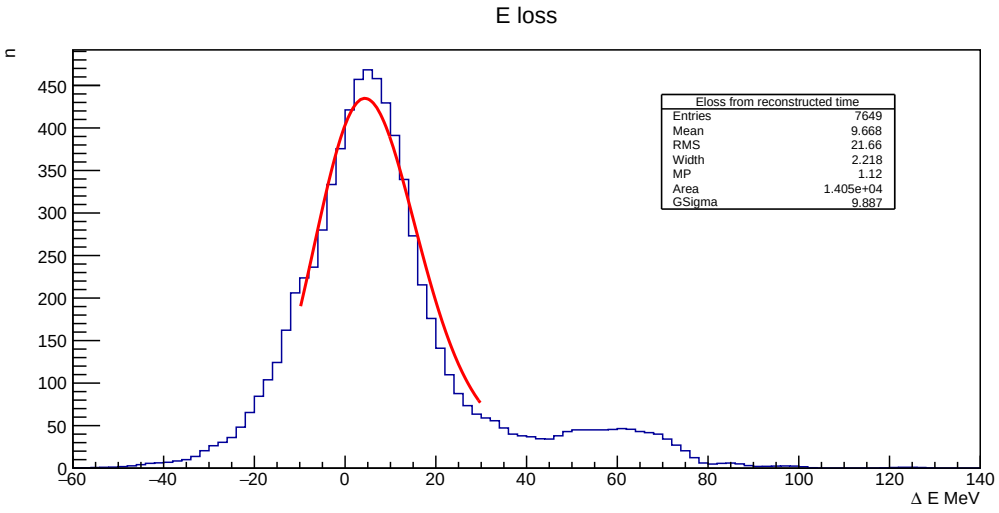

Figure 6.40: Energy loss of 200MeV/c Muons in the absorber cell without the LiH absorber. Measured using time of flight information obtained from the TOF detectors.

attempted in order to improve the fit, however it was found that the fit was not dependant on the range fitted to. This is representative of what energy loss should be expected from the aluminium and air contribution in the absorber unit.

The tail to high energy losses mirrors what was seen in the simulated data previously. Some contribution to this will be from muons that have undergone scattering in the cooling channel and lost a lot of energy in that process. Another small contribution will be from the detector resolutions. However, as it is possible to measure the peak directly and accurately, these effects can largely be ignored in favour of pursuing the measurement of the minimum ionising point.

6.3.3 LiH Data with 200 MeV/c beam

For real data with a 200 MeV/c muon beam, extra cuts were taken on the time-of-flight information at TOF1 to ensure that the muon region only was selected. An addition cut was made on muons with a momentum reconstructed at TOF1 greater than 220 MeV/c, as it appeared these muons did not have a correctly reconstructed momentum at TOF1, which would adversely effect the Energy loss measurement. This is shown in figure 6.41. Figure 6.42 shows the time-of-flight of muons between TOF0 and TOF1 after the cuts have been made. The distribution now is clearly a slice of data, but a large number of muons are still included in the dataset with 16k muons suitable for analysis.

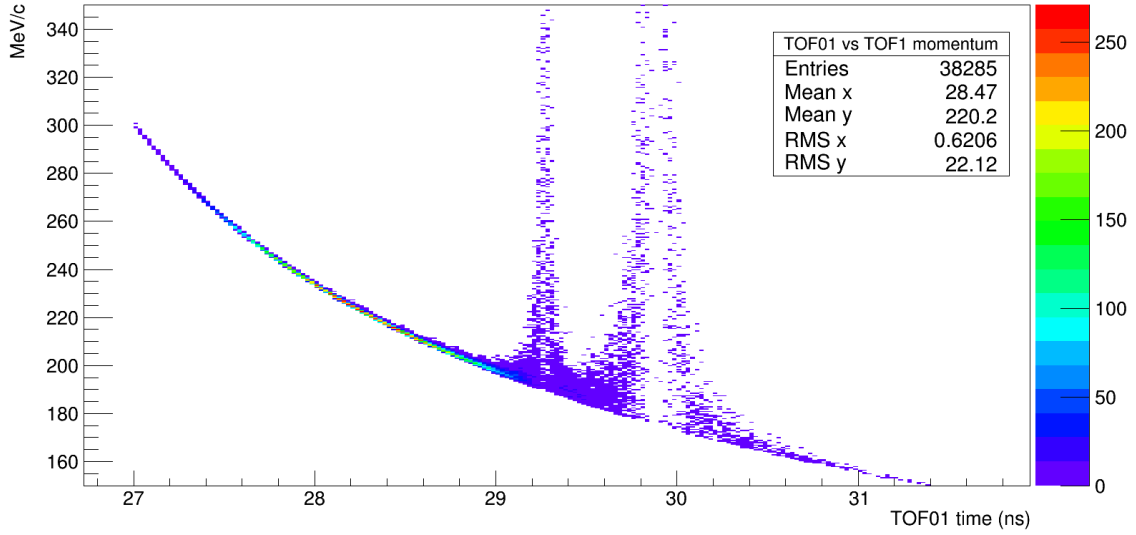

Figure 6.41: Time of flight between TOF0 and TOF1 vs the reconstructed momentum at TOF1. No timing cut has yet been taken.

The momentum of muons immediately prior to the absorber is reconstructed using the momentum reconstructed at TOF1 by the Rayner reconstruction method. Figure 6.43 shows the distribution of the corresponding muon energy. The average energy of the muon beam is at 222 MeV. The effects of the cuts taken are seen in the distribution, with clear slices taken either side of the peak. Figure 6.44 then shows the comparison between the momentum of muons reconstructed at TOF1 against the momentum prior to the absorber. As expected there is a linear relationship between the two.

Downstream of the absorber, the muon energy distribution shown in figure 6.45 has a measured mean energy of 206.3 MeV. This distribution has a clear tail to low energies, mirroring what was seen in the simulated data in figure 6.24. This is a direct result of the straggling that takes place in the absorber due to energy loss processes other than ionisation.

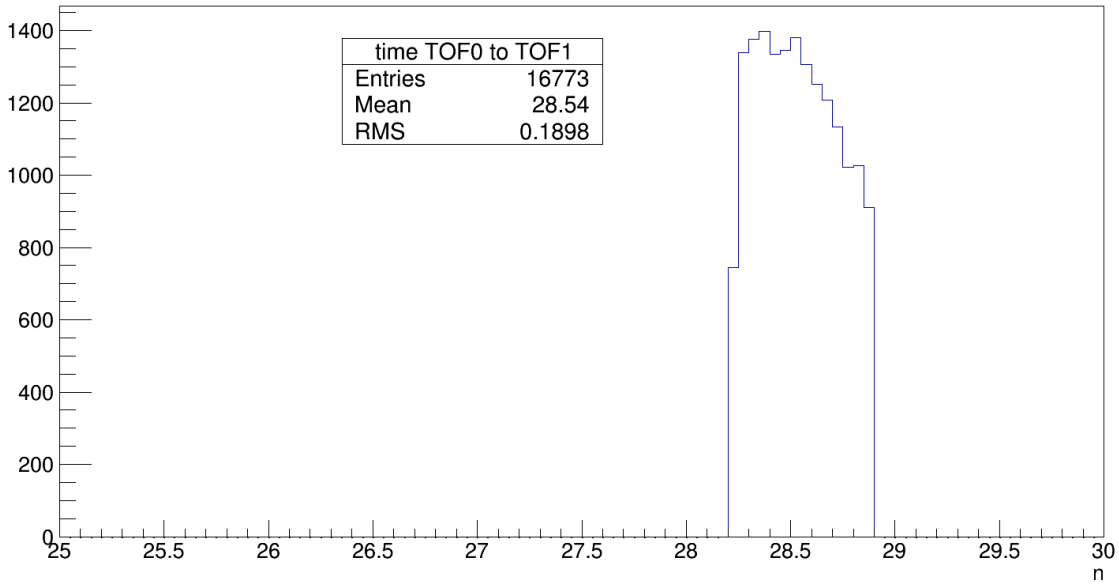

Figure 6.42: Time of flight between TOF0 and TOF1 after timing cuts.

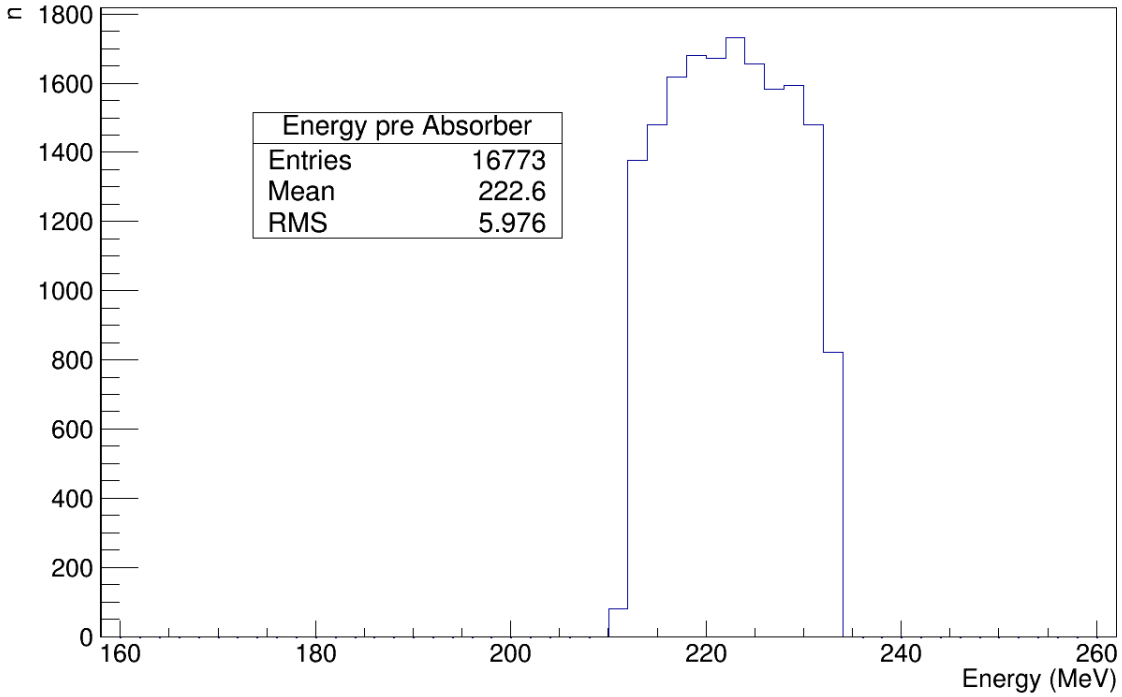

Figure 6.43: Energy of muons reconstructed prior to the absorber.

Figure 6.46 finally shows the energy loss of muons in the LiH absorber, reconstructed from time-of-flight information from the 3 TOF detectors. There is a long tail to high energy losses as a result of straggling in the LiH, however unfortunately the resolution of the measurement is not sufficient to suggest what proportion of muons are affected. The mean of the distribution lies at 16.16 ± 0.16 MeV. The peak is fitted with a Landau-gaussian convoluted function as with previous plots, so that the peaks can be directly compared. In this instance the landau MP parameter is fitted with a value of 10.35 ± 0.08

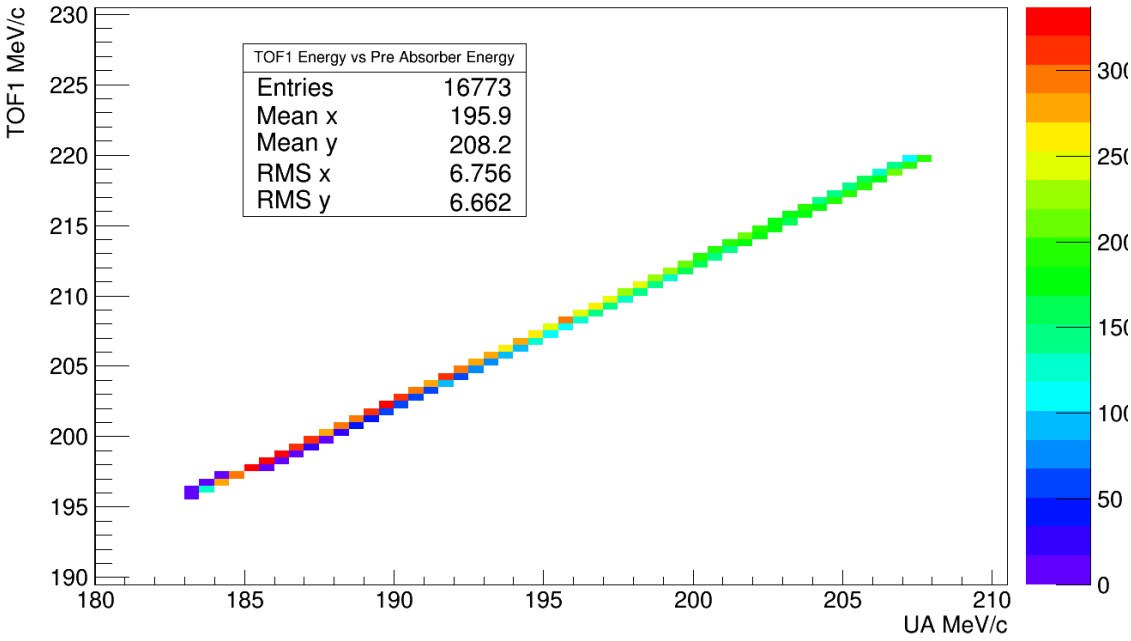

Figure 6.44: Momentum of muons at TOF1 vs the momentum of muons reconstructed prior to the absorber.

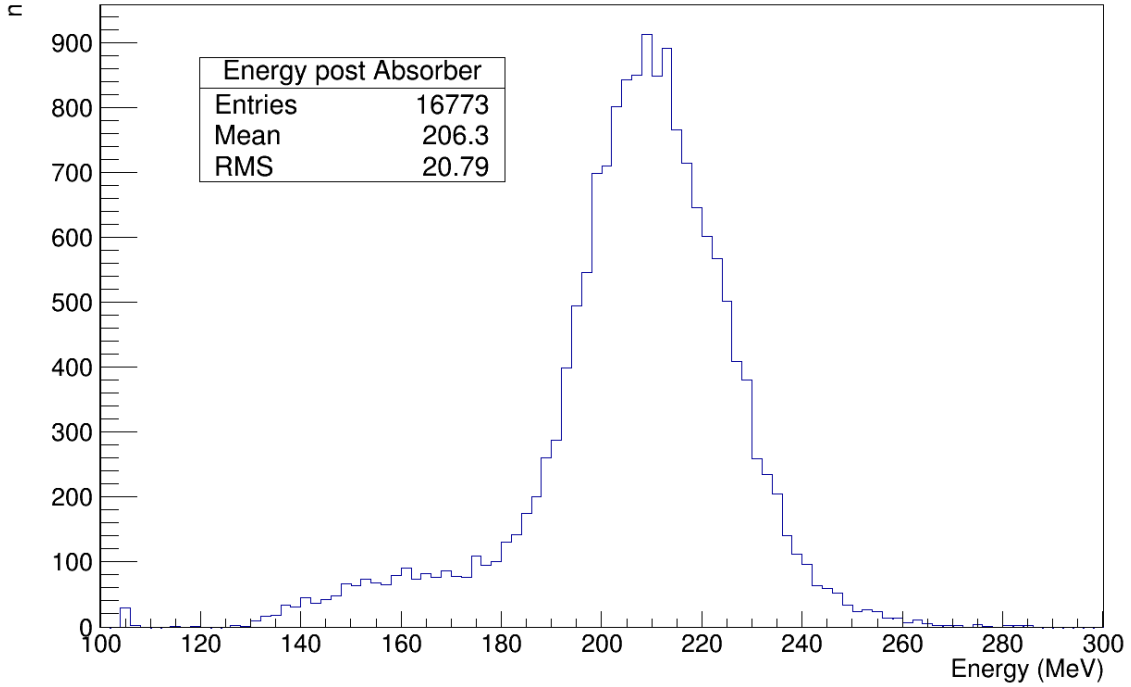

Figure 6.45: Energy distribution of muons after the absorber unit.

MeV. This differs from the peak measured in the simulation by 0.2 MeV. If the energy loss measured in the empty absorber is subtracted from this, then the most probable energy loss of 65mm of Lithium Hydride can be measured at 9.23 $\pm$ 0.13 MeV.

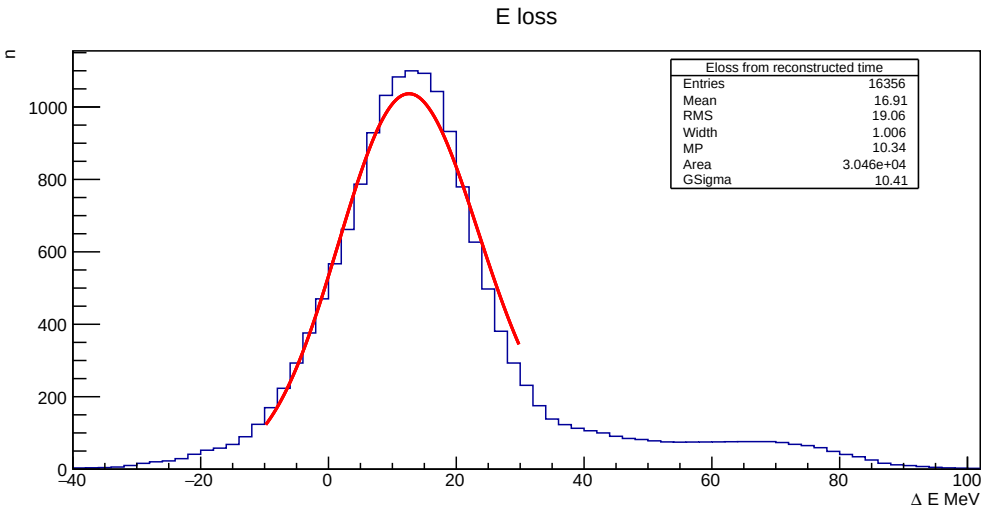

Figure 6.46: Energy loss of 200MeV/c Muons in 65mm of LiH and the absorber cell. Measured using time of flight information obtained from the TOF detectors.

6.4 Results Summary

6.4.1 Energy Loss Measurement

		MP ΔE /MeV	Mean ΔE/MeV
Field off measurement 200MeV/c MICE Data	Empty FC	1.12 ± 0.11	9.67 ± 0.25
	LiH Absorber in FC	10.35 ± 0.08	16.16 ± 0.16
	LiH Absorber only	9.23 ± 0.13	6.49 ± 0.30

Table 6.1: Results of Energy Loss by 200MeV/c Muons from 65mm Lithium Hydride.

Table 6.4.1 contains the results for the first measurement of Energy Loss by muons with momenta 200 MeV/c. Using only the time-of-flight detector data to measure the muon velocity, the most probable energy loss in 65mm of Lithium Hydride is therefore measured at 9.23 ± 0.13 MeV. This means that the modal stopping power of Lithium Hydride can be measured at $\frac{dE}{dx} = 1.42 \pm 0.02$ MeV g^{-1} cm^2. The modal energy loss rather than the mean energy loss measured has been quoted, as the mean is significantly skewed by the long tail when measuring the energy loss with no absorber, and therefore is not as reliable as the most probable energy loss. The accuracy of this measurement to 1.4% will be useful in understanding the transverse cooling measured in MICE Step IV.

		MP ΔE /MeV	Mean ΔE/MeV
Field on measurement MC Truth Data	Empty FC	1.504 ± 0.005	7.98 ± 0.09
	LiH Absorber in FC	10.68 ± 0.01	16.32 ± 0.09
	LiH Absorber only	9.18 ± 0.01	8.30 ± 0.13
Field off measurement Simulation Reconstruction	Empty FC	1.42 ± 0.01	8.30 ± 0.10
	LiH Absorber in FC	10.54 ± 0.04	16.69 ± 0.09
	LiH Absorber only	9.12 ± 0.04	8.40 ± 0.13

Table 6.2: Results from the field off simulated Step IV experiment.

6.4.2 Comparison of the Measurement to Simulation

Table 6.4.2 contains a summary of the results from analysing simulated and MICE data in the Step IV field off configuration. The measured energy loss is compatible to the measurement predicted by the monte carlo simulation of 9.18 ± 0.01 MeV. There is a greater error on the measured result compared to the simulated result, which can be attributed to the lower statistics of the data. It is expected that this measurement is comparable to the measurement that can be made with field in the solenoids by the trackers, as discussed in the previous chapter.

Chapter 7

Conclusion

When completed, the Muon Ionisation Cooling Experiment (MICE) will be the first demonstration of ionisation cooling, and will show that a high quality beam of muons can be produced with low emittance to satisfy the requirements for a neutrino factory. The ionisation cooling demonstrated by MICE is essential in the production of muon beams, due to the low lifetime of a muon. Changes to the design of MICE as a result of various issue have led to the current prediction that MICE will demonstrate 6% transverse emittance cooling, with some re acceleration of the beam in the longitudinal direction.

Determining the energy loss of muons in the absorber is an important measurement to make in order to properly understand the cooling effect. By using the time-of-flight data to reconstruct the velocity of the muon before, and after the absorber, the energy loss of muons inside the absorber was measured at $\Delta E = 9.23 \pm 0.13$ MeV. The stopping power of Lithium Hydride for 200 MeV/c Muons was measured for the first time as $\frac{dE}{dx} = 1.42 \pm 0.02$ MeV g^{-1} cm^2. Simulations of the experiment were able to demonstrate the accuracy of the reconstruction algorithms used to produce the measurement, and to demonstrate the feasibility of making energy loss measurements in the descoped Step IV MICE lattice. This marks the first time that the energy loss by muons has been measured at 200 MeV/c momentum, and the first measurement of any muon energy loss in Lithium Hydride.

Step IV of MICE marks an exciting opportunity for further material physics measurements, and the first demonstration of cooling as a result of the energy loss of the absorber. It is hoped that in the coming year, measurements will be made with field inside the solenoids so that tracker data can be obtained. These measurements may have the potential to compliment the energy loss measurement presented in this thesis. Together, the

measurements will be used in the cooling formula to determine the emittance reduction.

Bibliography

[1] F. T. Avigone, S. R. Elliott, and J. Engel. Double beta decay, majorana neutrinos, and neutrino mass. *Rev. Mod. Phys*, 80:481–516, 2008.

[2] F. J. Paul Soler. Final results from the IDS-NF study. *PoS*, NUFACT2014:072, 2015.

[3] Adam James Dobbs. *Particle Rate and Host Accelerator Beam Loss on the MICE Experiment*. PhD thesis, Imperial Coll., London, 2011. URL: http://lss.fnal.gov/cgi-bin/find_paper.pl?thesis-2011-51.

[4] C.N. Booth and P. Hodgson. The design, construction and performance of the MICE target. Technical report, 2012. MICE-NOTE-392. URL: http://mice.iit.edu/micenotes/public/pdf/MICE0392/MICE0392.pdf.

[5] P. Hodgson, C. Booth, P.J. Smith, and J. Tarrant. Mice target hardware. Technical report, 2010. MICE-NOTE-312. URL: http://hep04.phys.iit.edu/cooldemo/micenotes/public/pdf/MICE0312/MICE0312.pdf.

[6] S. Ishimoto, S. Suzuki, M. Yoshida, and I. Tsukuba. LIQUID HYDROGEN ABSORBER FOR MICE. Technical report, 2010. MICE-NOTE-310. URL: http://mice.iit.edu/micenotes/public/pdf/MICE0301/MICE0301.pdf.

[7] G. T. Kafka, P. Snopok, J. H. Cobb, and C. T. Rogers. Solid Absorber Program Status for MICE Step IV. *Conf. Proc.*, C110904:859–861, 2011.

[8] Y. Torun, P. Hanlet, and M. Leonova. Assembly and testing of the first 201-mhz mice cavity at fermilab. *Proceedings of PAC03*, 2:1016 – 1018, 2003.

[9] P. Soler. Luminosity monitor documentation. Technical report, 2010. DOCUMENTATION. URL: http://micewww.pp.rl.ac.uk/documents/7.

[10] L. Coney, M. Popovic, and M. Rayner. MICE Step I: First Measurement of Emittance with Particle Physics Detectors. *Conf. Proc.*, C110904:853–855, 2011.

[11] R. Bertoni, M. Bonesini, M. Bogomilov, A. de Bari, and G. Cecchet. Analysis of PID detectors (TOF and KL) performances in the MICE 2010 run. Technical report, 2013. MICE-NOTE-337. URL: http://mice.iit.edu/mnp/MICE0337.pdf.

[12] A. Manfredini, D. Orestano, L. Tortora, and M. Bogomilov. Kloe Light Manual. Technical report, 2009. KL-Technical-Manual. URL: http://mice.iit.edu/mico/manuals/KL-manual-15Dec09.pdf.

[13] D. Adams et al. Electron-muon ranger: performance in the mice muon beam. *Journal of Instrumentation*, 10(12):P12012, 2015. URL: http://stacks.iop.org/1748-0221/10/i=12/a=P12012.

[14] K. A. Olive et al. Review of Particle Physics. *Chin. Phys.*, C38, 2014. doi:10.1088/1674-1137/38/9/090001.

[15] ICRU Report 37. Stopping powers for electrons and positrons. *International Commission on Radiation Units and Measurements*, 1984.

[16] Donald E.Groom, Nokolai V.Mokhov, and Sergei I.Striganov. Muon stopping power and range tables 10 mev100 tev. *Atomic Data and Nuclear Data Tables*, 78(2):183 – 356, 2001. URL: http://www.sciencedirect.com/science/article/pii/S0092640X01908617, doi:http://dx.doi.org/10.1006/adnd.2001.0861.

[17] Mark Alastair Rayner. *The development of a novel technique for characterizing the MICE muon beam and demonstrating its suitability for a muon cooling measurement*. PhD thesis, Worcester College, Oxford, 2011.

[18] D. Adams et al. Characterisation of the muon beams for the Muon Ionisation Cooling Experiment. *Eur. Phys. J.*, C73(10):2582, 2013. arXiv:1306.1509, doi:10.1140/epjc/s10052-013-2582-8.

[19] W. Pauli. Letter to tubingen conference participants. Dec 1930.

[20] Kan Chang Wang. A suggestion on the detection of the neutrino. *Phys. Rev.*, 61:97–97, Jan 1942. URL: http://link.aps.org/doi/10.1103/PhysRev.61.97, doi:10.1103/PhysRev.61.97.

[21] F. Reines and C. L. Cowan. Detection of the free neutrino. *Phys. Rev.*, 92:830–831, Nov 1953. URL: http://link.aps.org/doi/10.1103/PhysRev.92.830, doi:10.1103/PhysRev.92.830.

[22] G. Danby, J-M. Gaillard, K. Goulianos, L. M. Lederman, N. Mistry, M. Schwartz, and J. Steinberger. Observation of high-energy neutrino reactions and the existence of two kinds of neutrinos. *Phys. Rev. Lett.*, 9:36–44, Jul

1962. URL: http://link.aps.org/doi/10.1103/PhysRevLett.9.36, doi:10.1103/PhysRevLett.9.36.

[23] M. L. et al Perl. Evidence for anomalous lepton production in $e^+ - e^-$ annihilation. *Phys. Rev. Lett.*, 35:1489–1492, Dec 1975. URL: http://link.aps.org/doi/10.1103/PhysRevLett.35.1489, doi:10.1103/PhysRevLett.35.1489.

[24] K. Kodama et al. Observation of tau neutrino interactions. *Phys. Lett.*, B504:218–224, 2001. arXiv:hep-ex/0012035, doi:10.1016/S0370-2693(01)00307-0.

[25] Bruce T. Cleveland, Timothy Daily, Jr. Raymond Davis, James R. Distel, Kenneth Lande, C. K. Lee, Paul S. Wildenhain, and Jack Ullman. Measurement of the solar electron neutrino flux with the homestake chlorine detector. *The Astrophysical Journal*, 496(1):505, 1998. URL: http://stacks.iop.org/0004-637X/496/i=1/a=505.

[26] Y. Fukuda, T. Hayakawa, and E. Ichihara. Evidence for oscillation of atmospheric neutrinos. *Phys. Rev. Lett.*, 81:1562–1567, Aug 1998. URL: http://link.aps.org/doi/10.1103/PhysRevLett.81.1562, doi:10.1103/PhysRevLett.81.1562.

[27] Q. R. Ahmad, R. C. Allen, and T. C. Andersen. Direct evidence for neutrino flavor transformation from neutral-current interactions in the sudbury neutrino observatory. *Phys. Rev. Lett.*, 89:011301, Jun 2002. URL: http://link.aps.org/doi/10.1103/PhysRevLett.89.011301, doi:10.1103/PhysRevLett.89.011301.

[28] Z. Maki, M. Nakagawa, and S. Sakata. Remarks on the Unified Model of Elementary Particles. *Progress of Theoretical Physics*, 28:870–880, November 1962. doi:10.1143/PTP.28.870.

[29] Carlo Giunti. *Fundamentals of neutrino physics and astrophysics*. Number 34A5427. 2007.

[30] K. Zuber. *Neutrino Physics*. IOP Publishing, 2007.

[31] K. A. Olive et al. Review of Particle Physics. *Journal of Physics G*, 33:1+, 2006. URL: http://pdg.lbl.gov.

[32] K. Abe, N. Abgrall, and H. Aihara (T2K Collaboration). The t2k experiment. *Nuclear Instruments and Methods in Physics Research Section A: Accelerators, Spectrometers, Detectors and Associated Equipment*, 659(1):106 – 135, 2011. URL: http://www.sciencedirect.com/science/article/pii/S0168900211011910, doi:http://dx.doi.org/10.1016/j.nima.2011.06.067.

[33] K. Abe et al. Observation of Electron Neutrino Appearance in a Muon Neutrino Beam. *Phys. Rev. Lett.*, 112:061802, 2014. arXiv:1311.4750, doi:10.1103/PhysRevLett.112.061802.

[34] P. Adamson, C. Backhouse, and G. Barr. Measurements of atmospheric neutrinos and antineutrinos in the minos far detector. *Phys. Rev. D*, 86:052007, Sep 2012. URL: http://link.aps.org/doi/10.1103/PhysRevD.86.052007, doi:10.1103/PhysRevD.86.052007.

[35] F. P. An, A. B. Balantekin, and H. R. Band. Spectral measurement of electron antineutrino oscillation amplitude and frequency at daya bay. *Phys. Rev. Lett.*, 112:061801, Feb 2014. URL: http://link.aps.org/doi/10.1103/PhysRevLett.112.061801, doi:10.1103/PhysRevLett.112.061801.

[36] M. Goeppert-Mayar. Double beta-disintegration. *Phys. Rev.*, 48:512, 1935.

[37] W.H. Furry. On transition probabilities in double beta-disintegration. *Phys. Rev.*, 56:1184, 1939.

[38] H. V. Klapdor-Kleingrothaus, I. V. Krivosheina, A. Dietz, and O. Chkvorets. *Phys. Lett. B*, 586:198–212, 2004.

[39] H. V. Klapdor-Kleingrothaus et al. *J. Phys. J A*, 12:147, 2001.

[40] Feasibility study 2 of a muon based neutrino source. 2001. URL: http://www.osti.gov/energycitations/product.biblio.jsp?osti_id=914482.

[41] S. Geer. Muon colliders and neutrino factories. *Annual Review of Nuclear and Particle Science*, 59:347 – 365, 2009.

[42] MICE: An International Muon Ionisation Cooling Experiment, Technical Reference Document. 2005.

[43] A. N. Skrinsky and V. V. Parkhomchuk. Cooling Methods for Beams of Charged Particles. (In Russian). *Sov. J. Part. Nucl.*, 12:223–247, 1981. [Fiz. Elem. Chast. Atom. Yadra12,557(1981)].

[44] R. C. Fernow and J. C. Gallardo. Muon transverse ionization cooling: Stochastic approach. *Phys. Rev. E*, 52:1039 – 1042, 1995.

[45] M Bogomilov et al (MICE Collaboration). The mice muon beam on isis and the beam-line instrumentation of the muon ionization cooling experiment. *Journal of Instrumentation*, 7(05):P05009, 2012. URL: http://stacks.iop.org/1748-0221/7/i=05/a=P05009.

[46] T. Roberts. MICE Beamline Magnet Drawings. Technical report, 2003. MICE-NOTE-65. URL: http://hep04.phys.iit.edu/cooldemo/micenotes/public/pdf/MICE0065/MICE0065.pdf.

[47] Linda Coney. Status of the MICE Muon Ionization Cooling Experiment. In *Particle accelerator. Proceedings, 23rd Conference, PAC'09, Vancouver, Canada, May 4-8, 2009*, page TU6RFP057, 2010. URL: http://accelconf.web.cern.ch/AccelConf/PAC2009/papers/tu6rfp057.pdf.

[48] M Apollonio, J Cobb, M Dawson, T Handford, P Lau, W Lau, J Tacon, M Tacon, and S Yang. The MICE diffuser system. In *11th European Particle Accelerator Conference (EPAC 08), Genoa, Italy*, pages 23–27, 2008.

[49] A Dobbs and others. The MICE Muon Beam: Status and Progress. Technical report, 2010. MICE-NOTE-300. URL: http://mice.iit.edu/micenotes/public/pdf/MICE0300/MICE0300.pdf.

[50] D. Li et al. A 201 mhz rf cavity design with non-stressed pre-curved be windows for muon cooling channels. *Proceedings of PAC03*, 2:1243 – 1245, 2003.

[51] D. Stratakis, J. Gallardo, and R. Palmer. Effects of external magnetic fields on the operation of high-gradient accelerating structures. *Nucl. Instr. and Meth. A*, 620:147–154, 2010.

[52] R. Bertoni, A. Blondel, M. Bonesini, G. Cecchet, A. de Bari, J.S. Graulich, Y. Karadzhov, M. Rayner, I. Rusinov, R. Tsenov, S. Terzo, and V. Verguilov. The design and commissioning of the {MICE} upstream time-of-flight system. *Nuclear Instruments and Methods in Physics Research Section A: Accelerators, Spectrometers, Detectors and Associated Equipment*, 615(1):14 – 26, 2010. URL: http://www.sciencedirect.com/science/article/pii/S0168900209024024, doi:http://dx.doi.org/10.1016/j.nima.2009.12.065.

[53] E. Overton. Progress with the MICE scintillating fiber trackers. Technical report, 2012. MICE-NOTE-408. URL: http://mice.iit.edu/micenotes/public/pdf/MICE0408/MICE0408.pdf.

[54] A. Dobbs, C. Hunt, K. Long, E. Santos, and C. Heidt. The Reconstruction Software for the MICE Scintillating Fibre Trackers. Technical report, 2014. MICE-NOTE-451. URL: http://mice.iit.edu/micenotes/public/pdf/MICE0451/MICE0451.pdf.

[55] S.P. Virostek, M.A. Green, F. Trillaud, and M.S. Zisman. Fabrication, testing and modeling of the mice superconducting spectrometer solenoids. In *Proceedings of IPAC10*, 2010. URL: http://alturl.com/694wz.

[56] M. Antonelli, F. Anulli, G. Barbiellini, S. Bertolucci, C. Bini, and C. Bloise. The kloe electromagnetic calorimeter. *Nuclear Physics B - Proceedings Supplements*, 61(3):126 – 131, 1998. Proceedings of the Fifth International Conference on Advanced Technology and Particle Physics. URL: http://www.sciencedirect.com/science/article/pii/S0920563297005501, doi:http://dx.doi.org/10.1016/S0920-5632(97)00550-1.

[57] Paul H. Barrett, Lowell M. Bollinger, Giuseppe Cocconi, Yehuda Eisenberg, and Kenneth Greisen. Interpretation of cosmic-ray measurements far underground. *Rev. Mod. Phys.*, 24:133–178, Jul 1952. URL: http://link.aps.org/doi/10.1103/RevModPhys.24.133, doi:10.1103/RevModPhys.24.133.

[58] H. Bethe and J. Ashkin. Experimental Nuclear Physics. page 253, 1953.

[59] J. F. Zeigler. *Applied Physics Reviews*, 85:1249–1272, 1999.

[60] L.D. Landau. *J. Exp. Phys. (USSR)*, 201, 1944.

[61] Hans Bichsel. Straggling in thin silicon detectors. *Rev. Mod. Phys.*, 60:663–699, Jul 1988. URL: http://link.aps.org/doi/10.1103/RevModPhys.60.663, doi:10.1103/RevModPhys.60.663.

[62] S. Agostinelli et al. GEANT4: A Simulation toolkit. *Nucl. Instrum. Meth.*, A506:250–303, 2003. doi:10.1016/S0168-9002(03)01368-8.